Summer 8-2020

Structural Characterization of Organic Matter in Oil Shales Using Multiple Nuclear Magnetic Resonance Spectroscopic Techniques

Wenying Chu
Old Dominion University, wychu106@gmail.com

STRUCTURAL CHARACTERIZATION OF ORGANIC MATTER IN OIL SHALES USING MULTIPLE NUCLEAR MAGNETIC RESONANCE SPECTROSCOPIC TECHNIQUES

by

Wenying Chu
B.S. June 2008, Huazhong Agricultural University, China

A Dissertation Submitted to the Faculty of
Old Dominion University in Partial Fulfillment of the
Requirements for the Degree of

DOCTOR OF PHILOSOPHY

CHEMISTRY

OLD DOMINION UNIVERSITY
August 2020

Approved by:

Jingdong Mao (Director)

Guijun Wang (Member)

John R. Donat (Member)

Lesley H. Greene (Member)

Shizhi Qian (Member)

ABSTRACT

STRUCTURAL CHARACTERIZATION OF ORGANIC MATTER IN OIL SHALES USING MULTIPLE NUCLEAR MAGNETIC RESONANCE SPECTROSCOPIC TECHNIQUES

Wenying Chu
Old Dominion University, 2020
Director: Dr. Jingdong Mao

Oil shale is a promising source of hydrocarbon fuel that is distributed throughout the world. The petroleum generating potential of oil shale is related to the molecular structure of the organic matter in source rock. The major fraction of organic matter of oil shale is termed kerogen, and due to its insolubility in organic solvents, ^{13}C solid-state nuclear magnetic resonance (NMR) spectroscopy is one of the best ways to directly measure the insoluble organic matter without changing its chemical structures. This dissertation investigated oil shale samples using advanced solid-state ^{13}C NMR spectroscopy techniques and high resolution magic angle spinning (HRMAS) NMR spectroscopy, and studied bitumen samples extracted from oil shales using liquid-state NMR spectroscopy. Quantitative ^{13}C solid-state NMR spectra were generated for 22 shale samples and their percentages of different carbon moieties were integrated and aromaticities were calculated. Aromaticity was considered as a supplemental indicator of the thermal maturity and hydrocarbon generating potential of the oil shale. By investigating quantitative structural characteristics of three shales with extreme heteroatom contents, we found out that he high oxygen content in organic matter in the Kukersite shale sample indicated more non-protonated aromatic carbons, which were substituted with oxygen. An improved structural model of Kukersite kerogen was constructed based on one from literature and refined using our spectral data. The high organic sulfur content in the organic matter present in the Jordanian Ghareb shale sample was mostly contributed to the

high aromaticity of the organic matter in the sample. The Glen Davis shale sample contained organic matter with a relatively low total heteroatom content and produced comparatively simpler spectra due to the presence of few oxygen-containing functional groups. A comparative study showed that Kimmeridge and Phosphoria formation had similar solid-state ^{13}C NMR spectra from shale, kerogen, and extracted rock samples, and they exhibited almost the same signals in liquid-state 2D ^{1}H-^{13}C HSQC spectra from bitumen samples, indicating their similar structural characteristics, in spite of their differences in geologic age and depositional location. By examining shales samples with advanced solid-state ^{13}C NMR, quantitative data can be obtained and could be used for constructing more reliable kerogen structural models and for predicting petroleum generating potential.

This dissertation is dedicated to my parents,
Yuehua Chu and Shiqun Zhou, who always support my decisions.

To my husband Chad J. Hinton and my son Liam C. Hinton,
without whom this dissertation would have been completed and defended earlier.

ACKNOWLEDGMENTS

I would like to express my sincere gratitude to Dr. Jingdong Mao, who advised me through my Ph.D. journey on academic, career, and life choices, for his valuable guidance, support, inspiration, and understanding. I would also like to thank my dissertation committee members, Dr. Guijun Wang, Dr. John R. Donat, Dr. Lesley H. Greene, and Dr. Shizhi Qian for their comments, direction, and suggestions to help the completion of this dissertation.

I must thank Dr. Justin E. Birdwell at the United States Geological Survey for providing all the samples and background information studied in this dissertation, and for his guidance to get my research published.

I would also like to thank Dr. Klaus Schmidt-Rohr research group at Brandeis University for performing 2D solid-state NMR measurements and kerogen structural model construction. Thanks also go to College of Sciences Major Instrumentation Cluster (COSMIC) at Old Dominion University (ODU) and Professor John Cooper for providing access to solid-state NMR and HRMAS NMR instruments. Many thanks to Isaiah Ruhl and Ravi Garimella for the training and assistance in COSMIC.

Special thanks to Drs. Craig Bayse, James Lee, Jennifer Poutsma, Jingdong Mao, John Cooper, John Donat, Patrick Hatcher, and Steven Pascal for the courses they offered. Their courses have broadened my knowledge and perspective. I would also like to thank Drs. David Courson, Janet Moloney, Josh Wallach, and Pinky McCoy for their advices on how to succeed in teaching.

I am very thankful to my former group member Xiaoyan Cao who took the time to train and help me at the beginning of my research on data processing and NMR spectrum analysis. I am

grateful to all the faculty and staff in the Department of Chemistry and Biochemistry at ODU; each of them played a special role in my graduate life and has helped me in specific ways.

I am grateful to many friends I have met during my graduate years at ODU: Anji Chen, Dan Wang, Jennifer Mejia, Joedian Morris, Kristen Burns (Bashaw), Linmin Pei, Luni Sun, Rui Wang, Xi Chen, Yi Jian, Yuanyuan Yue, Yuhou Gao, and Zhiyi Yang for all the good times.

Finally, I wish to leave my gratitude to my family for all the love and support throughout the years.

TABLE OF CONTENTS

Page

Page

LIST OF TABLES

Table Page

LIST OF FIGURES

Figure Page

CHAPTER I

INTRODUCTION

ORIGINS AND TYPES OF OIL SHALES

Oil shales are diverse fine-grained sedimentary rocks containing refractory organic material that generates commercial quantities of synthetic crude oil and combustible gas upon pyrolysis at high temperatures (>350 °C), which can then be refined into liquid hydrocarbon fuels (Birdwell, 2017; Dyni, 2003; Yen and Chilingarian, 1976). The inorganic fraction of a shale is the mineral composition of the formation while the organic fraction contains mainly a solid material, termed kerogen, which is insoluble in organic solvents, and soluble bitumen (Dyni, 2003; Tissot and Vandenbroucke, 1983). Oil shales originate from the deposition of fine-grained mineral debris and organic degradation products derived from the breakdown of biota which went through early development of anaerobic conditions under sufficient overburden pressure and temperature (Yen and Chilingarian, 1976). Organic matter in oil shales is a mixture from remains of algae, spores, pollen, plant cuticle, corky fragments of herbaceous and woody plants, plant resins, plant waxes, and other cellular remains of lacustrine, marine, and land plants which are mainly composed of carbon, hydrogen, oxygen, nitrogen, and sulfur (Speight, 2012). Oil shale could be deposited in a wide variety of environments from fresh to saline water, including large lake basins, shallow seas on continental platform and shelves, and small lakes, bogs, and lagoons associated with coal-forming swamps (Speight, 2012; Yen and Chilingarian, 1976).

Oil shales are diverse in genesis, lithologic property, and organic composition so that there are more than one way to classify oil shales. Oil shales can be categorized based on the mineral content into carbonate-rich oil shales, siliceous oil shales, and cannel oil shales. More commonly,

oil shales are classified into terrestrial, marine, and lacustrine origin on the basis of the depositional environment of the deposit, the petrographic character of the organic matter, and the precursor organisms from which the organic matter was derived (Dyni, 2003; Hutton, 1987). Terrestrial oil shales are rich in oil-generating lipid-rich organic matter originated from terrestrial vascular plants commonly found in coal-forming swamps and bogs, such as the brown to black oil shale called cannel coal. Lacustrine oil shales contain lipid-rich organic matter derived from algae that lived in freshwater, brackish, or saline lakes, such as lamosite and torbanite. Marine oil shales include lipid-rich organic matter derived from marine algae, acritarchs, and marine dinoflagellates, such as kukersite, tasmanite, and marinite (Dyni, 2003; Speight, 2012).

SHALE DEPOSIT DISTRIBUTION

As a result of the fast depletion of easily obtained petroleum resources, many coutries have been focusing on searching for alternative energy sources. As one of the promising sources of hydrocarbon fuel, shale formations are widely distributed throughout the world (Figure 1) with know deposits including Australia, Brazil, Canada, China, Estonia, Israel, Jordan, Morocco, Russia, Scotland, Spain, Sweden, Syria, Thailand, Turkey, and United States, yet very limited deposits have been thoroughly studied and explored. The total amount of potential shale oil reserved in oil shales world-wide is abount 475 billion tons, which is about 4.4 times larger than the current recoverable reserves of crude oil (Pan et al., 2012),

The oil shale deposits in Australia are located in the eastern side of the country. There are torbanite deposits of New South Wales and Queensland, marine tasmanite deposits of Permian age in Tasmania, marine Toolebuc Formation of Early Cretaceous age in Queensland and adjacent States, and lamosite deposits in eastern Queensland which were mined for shale oil from late 1800s to early 1900s or still have the potential for development (Crisp et al., 1987; Dyni, 2003).

In Brazil, at least 9 shale deposits have been reported, and the most famous two are the lacustrine oil shale of Tertiary age in the Paraiba Valley and the oil shale of the Permian Irati Formation (Padula, 1969). Between those two, the Irati Formation has a great potential for economic development due to its accessibility, grade, and widespread distribution. A few oil-shale retort plants were established and have been producing shale oil, liquefied petroleum gas, methane, and sulfur (Dyni, 2003).

As many as 19 oil-shale deposits have been identified in Canada, including the Devonian Kettle Point Formation and the Ordovician Collingwood Shale of southern Ontario, and the oil shales of the New Brunswick of Mississippian age, which have the greatest potential for development. The lacustrine Albert Formation deposits in southern New Brunswick have substantial amount of shale oil yield and a lot of products are exported to other countries such as the U.S. and England (Dyni, 2003; Macauley et al., 1984).

Oil shale deposits are widespread in China, the deposit in Fushun, Liaoning Province of Eocene age is in northeastern China and the deposit in Maoming, Guangdong Province of Tertiary age is located in southeastern China (Dyni, 2003). The two oil shale deposits were mined and processed in refineries until the Daqing oil field was found to produce cheaper crude oil. Up to 2002, Fushun shale oil plant was still making profits due to relatively low mining cost and was planning on extending to larger retorts and production capacity. Some other coal mining companies were developing the oil shale business as well (Qian et al., 2003).

In Estonia, there are the most famous kukersite oil shale deposit of Ordovician age in northern Estonia covering more than 5% of Estonian mainland, and the marine Dictyonema argillite as uranium shale (Dyni, 2003). Almost 1 billion tons kukersite oil shale has been extracted since 1916 for fuel electric power plants, petrochemicals production, and cement manufacture

(Dyni, 2003; Reinsalu and Valgma, 2003). The Dictyoneme oil shale was mainly mined for the production of uranium between 1949 and 1952, and total 240500 tons of ore with an average uranium content of 0.036% was extracted (Reinsalu and Valgma, 2003).

Jordan has large oil shale deposits distributed all over the country covering more than 60% of Jordan's territory (Bsieso, 2003), and the eight important deposits are located in west-central Jordan close to the east of the Dead Sea (Dyni, 2003). Jordanian oil shale belongs to the upper Cretaceous and lower Tertiary ages and is estimated to be more than 50 billion tons which is capable of yielding 50 billion barrels of crude oil (Bsieso, 2003). Two oil shale deposits, El-Lajjun and Sultani have the potential for industrial utilization due to their good quality and quantity and the low mining and infrastructure costs, and the Government of Jordan has invited proposals to develop the source economically and cleanly (Bsieso, 2003).

In Russia, there is a long history of utilizing shales for direct burning, gas production, oil production, and agriculture (Russell, 1990). More than 100 deposits of oil shale have been identified, and the deposits of economic and commercial importance that have been exploited are in the Northwestern and Baltic states (Dyni, 2003; Russell, 1990). The distribution and origins of shale deposition are associated with ancient platform areas formed at various times including Cambrian age, late Devonian age, late Carboniferous-early Permian age, lower Triassic age, Cenozoic age, and the Quarternary age (Russell, 1990). The oil shale industry supplied shale as fuel for industrial boilers and railroad locomotives, and enhanced automation and mechanization increased the rate of oil shale processing, but this overall development of the oil shale industry increased steadily until the 1975-1980 when some problems arose such as loss of a large percentage of the shale in place during mining operations, continuing technological lag in the production of shale-based fuel and chemicals, and high pollution levels (Russell, 1990).

A famous oil shale deposit in Sweden is the Alum shale, a black organic-rich marinite of Cambrian and lower Ordovician age. It represents slow deposition in shallow, near-anoxic water with little disturbance. The Alum shale has a high content of metals such as uranium, vanadium, nickel, and molybdenum. More than 62 tons of uranium were produced between 1950 and 1961 and about 50 tons of uranium per year between 1965 and 1969. The oil yields of the Alum shale varies from 0 to 6 percent by Fischer assay due to different geothermal histories (Dyni, 2003).

The oil shale deposits in the United States occur from the late Tertiary to the Ordovician and Precambrian period located in various states including Alaska, Montana, Michigan, Wisconsin, Nevada, Kansas, etc (Yen and Chilingarian, 1976). The most important deposits in United States are the Eocene Green River Formation in the tri-state area of northwestern Colorado, southwestern Wyoming, and northeastern Utah, and the Devonian-Mississippian black shales in the central and eastern United State (Dyni, 2003). The Green River Formation is rich in organic material and was estimated to be able to produce 80 billion barrels of shale oil (Yen and Chilingarian, 1976), and the estimation went up to more than 1 trillion barrels with the better understanding of the shale formation (Dyni, 2003). The Green River shale deposit also contains large resources of sodium carbonate minerals which can be used in the manufacture of bottle and flat glass, baking soda, soap and detergents, waste treatment chemicals, and many other industrial chemicals (Dyni, 2003). The Devonian-Mississippian black shales have a higher aromatic to aliphatic ration than that of Green River Formation, and the oil yield is estimated to be only half as much as the Green River oil shale, but hydroretorting can increase the oil yield of the black shale compared to Fischer assay (Dyni, 2003). The black shales were exploited for shale gas to use in village heating, cooking, and illumination (Roen and Kepferle, 1993).

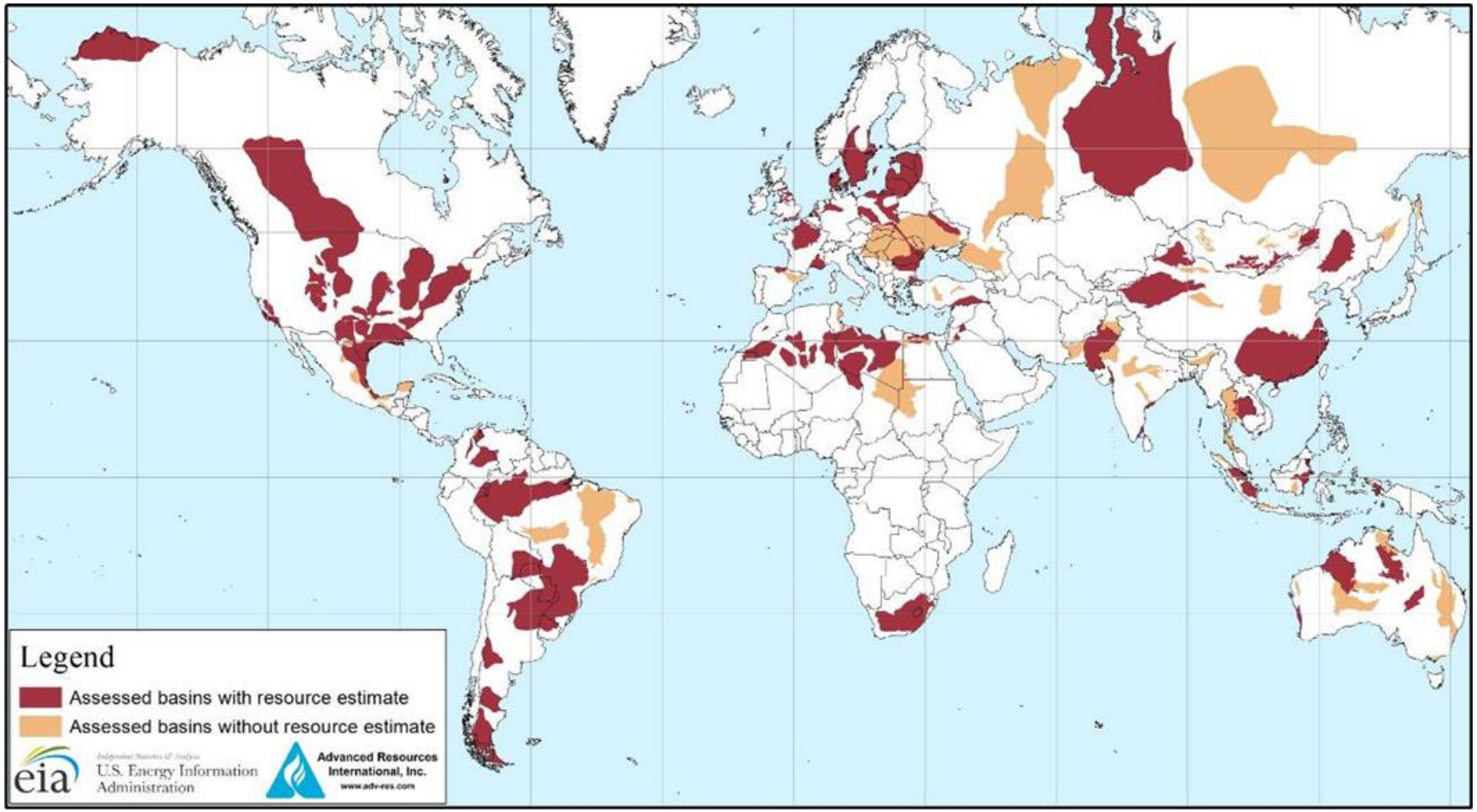

Figure 1. Map of basins with assessed shale oil and shale gas formations world-wide, as of May 2013, adapted from (Kuuskraa et al., 2013).

GRADE OF OIL SHALES

The grade of oil shales has been determined and expressed by different methods. Core drilling and analyses (such as Fischer assay) provide direct measurement of oil yields in oil shales. Geophysical well-logging methods use a probe that is lowered in the well at the end of an insulated cable, and physical measurements are performed and characteristic data are recorded in graphical form as functions of depth (Yen and Chilingarian, 1976). Geophysical well-logging methods provide a detailed estimation of the entire length of drilled hole on the exploration, evaluation, and production of oil and gas in a faster, more economical way, but core analysis data are always important at least in the first test hole to provide empirical correlation between the measured oil yield and the response of the geophysical well-logging (Yen and Chilingarian, 1976).

Traditionally, the grade of an oil shale can be determined by measuring the yield of oil of a shale sample in a laboratory retort. In industrial production, a shale deposit which yields 25 gallons of oil per ton of oil shale is considered as a high-yield deposit (Speight, 2012). In laboratory, a common method for determining the oil potential of an oil shale is the "modified Fischer assay" which was standardized as the American Society for Testing and Materials Method D-3904-80 (Miknis, 1992). In the method, a 100 g sample of -8 mesh (2.38 mm) sieved oil shale is heated to 500 ºC at a rate of 12 ºC per minute and held at this temperature for 40 minutes. The hydrocarbon vapors that distill from the shale are condensed to form shale oil and is recorded as weight percentage or gallons of oil per ton of shale (Dyni, 2003; Miknis, 1992). The Fischer method does not determine the total available energy in an oil shale or necessarily indicate the maximum amount of oil that can be produced by the given oil shale (Dyni, 2003). It does not provide any information about the quantity or quality of kerogen in the shale, and one cannot tell whether the amount or

the structure of kerogen causes the different shale oil yields between two shales determined by the Fischer assay (Miknis, 1992).

Rock-Eval pyrolysis is a temperature programmed pyrolysis to rapidly evaluate the petroleum-generative potential and thermal maturity of source rocks. The method heats a 70 mg rock sample in an inert atmosphere (helium or nitrogen) through several temperature stages in order to quantitatively and selectively determine the free hydrocarbons present in the sample (S_1 peak) and the hydrocarbon- and oxygen-containing compounds that are volatilized during the cracking of kerogen (S_2 peak). An illustration of Rock-Eval pyrolysis trace is shown in Figure 2. The CO_2 generated is recorded as the S_3 peak and residual carbon is recorded as S_4 peak (Behar et al., 2001; Speight, 2012). T_{max} is the temperature at which S_2 peak reaches the maximum, and it is an indication of the nature and maturity of the kerogen. The Rock-Eval parameters describe the quality of organic matter in the source rocks for exploration purpose (Behar et al., 2001).

The oil yields of shales upon pyrolysis depend on multiple factors including the natural evolution of the rock (the geological history, especially depth of burial), the abundance of kerogen in the shale, and the structural characteristics of kerogen (Maciel et al., 1978; Maciel et al., 1979; Tissot and Welte, 1984). The molecular structure of kerogen is highly related to the source organism and the depositional environment (Longbottom et al., 2016). It would be very useful to develop a reliable method to evaluate the grade of oil shales that could predict the total heat energy, the quantity and quality of the oil and gas that could be generated, and the amount of char in the residue. The price of crude oil is related to its organic acid content, distillation characteristics, sulfur content, viscosity, refraction, and density (Stratiev et al., 2010), which is usually reflected as American Petroleum Institute gravity (API gravity, a measure of how heavy or light a petroleum liquid is compared to water). Since the composition and quality of shale oil, to some extent, is a

direct result of the molecular structure of the sedimentary organic matter (Williams and Douglas, 1985), understanding structural characteristics of the organic matter in oil shale is critical in predicting the quality of the crude oil.

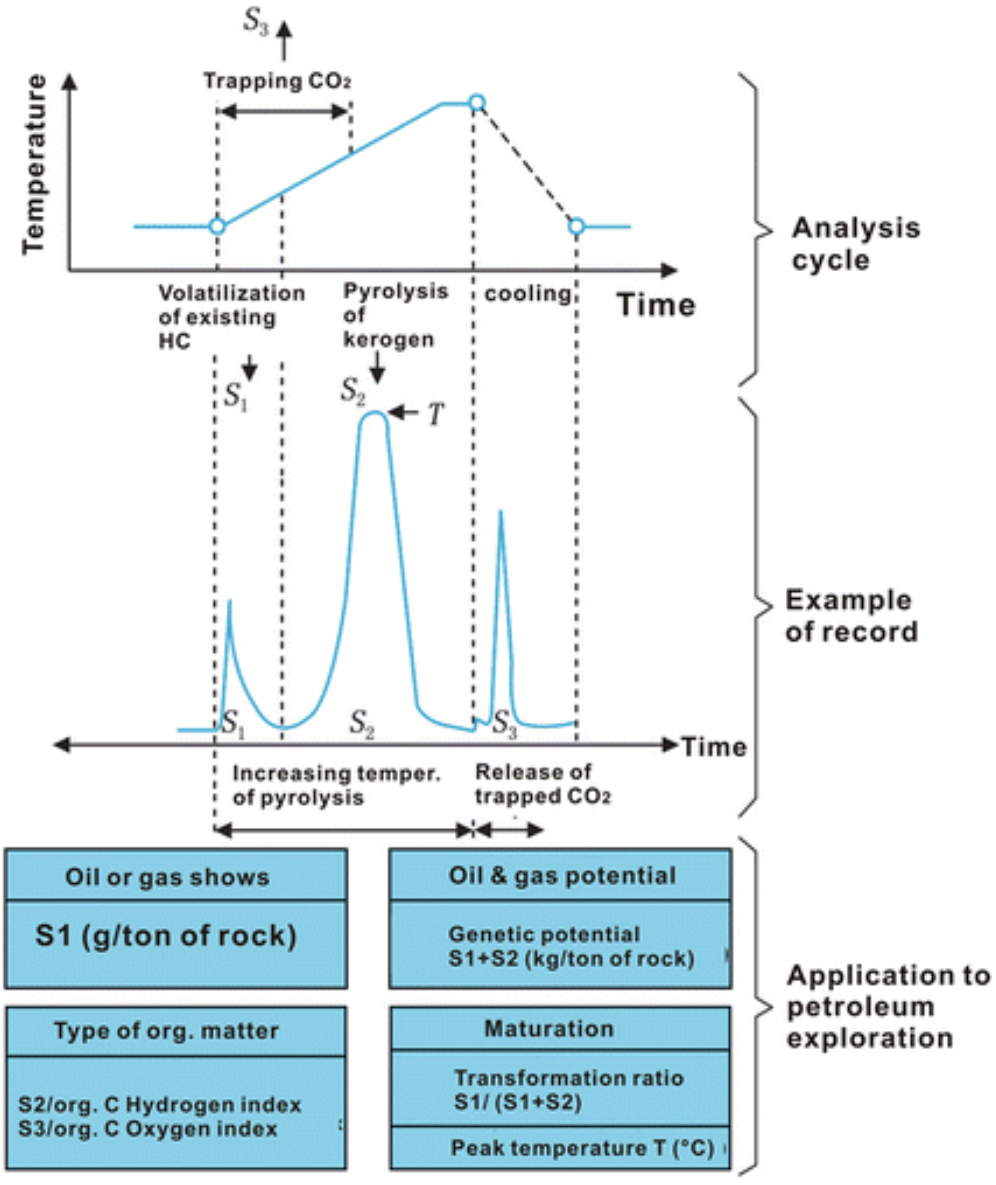

Figure 2. An illustration of Rock-Eval pyrolysis trace, adapted from (Guan et al., 2017).

SHALE OIL PRODUCTION

A major requirement for utilizing oil shale as a source of liquid and gaseous fuels is the thermal decomposition process termed retorting (Yen and Chilingarian, 1976). The heating process is necessary to convert the organic matter embedded in shales to liquid hydrocarbons and combustible gases, either through a low-temperature retorting (semi-coking) by heating the oil shale up to about 500 °C or a high-temperature retorting (coking) by heating up the oil shale up to 1000-1200 °C (Speight, 2012).

The retorting process can occur either aboveground or underground. The aboveground retorting is also called ex situ production. The general steps shown, in Figure 3, include: (1) surface mining the target deposit by blasting or excavators; (2) preparing ore by crushing and screening it into sizes suitable for transportation and retorting; (3) transporting mined shale to facilities for retorting; (4) pyrolysis of oil shale to get crude products; (5) upgrading and refining the raw products to marketable products; and (6) spent shale disposal and possible reclamation of mined area (Bartis et al., 2005; Speight, 2012; Väli et al., 2008). Some alternative mining methods are preferred depending on the depth of the target deposit. Among those methods, open-pit mining is suitable for the deposit where the overburden is less than 150 feet thick and the ratio of overburden thickness to deposit thickness ratio is less than 1:1; and room and pillar mining is viable when the overburden is too thick for surface mining. Both mining methods have been proven at commercial scale for oil shale production (Speight, 2012). Many aboveground retorting systems have been tested and a few succeeded in large scale production, including gas combustion retorting system, Union Oil Company retorting system, TOSCO II process system (Yen and Chilingarian, 1976), Fushun retorting system in China, Kiviter lump shale retorting system in Estonia, Petrosix lump shale retorting system in Brazil, Galoter particulate shale retorting system in Estonia, ATP

retorting system in Canada, and Enefit-280 retorting system upgraded from Galoter technology (Pan et al., 2012).

Aboveground retorting has advantages of high organic matter recovering efficiency, well-controlled operation, simple product recovery, and repeated usage of operational facilities. Aboveground retorting developed during 1970s-1980s, and significant problems arose during the development (Bartis et al., 2005). The disadvantages of aboveground retorting are obvious, such as high cost due to mining, ore preparation and transportation, limitation to rich-shale resources due to the high cost, spent shale disposal and its potential ground water pollution, high cost to reclaim and revegetate the mined area, and high capital investment for large-scale facilities (Speight, 2012).

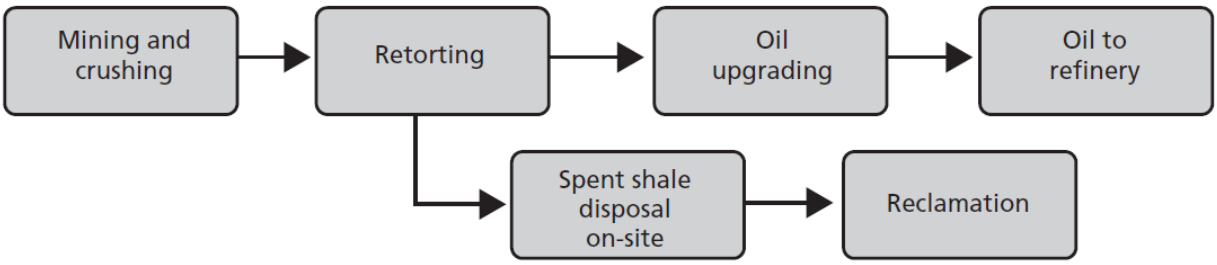

Figure 3. Major steps in aboveground retorting process, adapted from (Bartis et al., 2005).

In contrast to aboveground retorting, underground or in situ retorting involves heating the shale in situ (underground) by using underground combustion, introducing heated gases or liquids to the shale formation, or using electrical heating elements (Han et al., 2014). The liquids generated will then be collected and transported to an upgrading or refining facility (Bartis et al., 2005). In

situ retorting may be applicable to deposits that contain lower grade shale with yield down to 10 gallons of shale oil per ton of shale (Speight, 2012), as well as deposits with different thickness and amounts of overburden that are not suitable for surface mining economically (Yen and Chilingarian, 1976). Two approaches have been tested: (1) true in situ method which involves dewatering, fracturing, retorting by injection of hot fluid or ignition of a portion of the bed, and recovery of the oil and gas through wells (Congress, 1980); and (2) modified in situ method which consists of digging a tunnel to the bottom of the shale bed, mining enough shale to create a room, drilling a chimney-shaped underground retort filled with broken shale, injecting air and burning fuel to ignite the rubble pile, pyrolysis of lower layers with the heat generated, and pumping the products to the surface (Congress, 1980). An example of in situ retorting process in shown in Figure 4.

The advantages of underground retorting include avoiding large amount of shale mining and transporting, ability to generate products from deep deposits of shale formation, eliminating the necessity of disposing of spent shale waste, possibility to utilize low-grade shale formation, and lower cost due to minimized mining, transportation, and crushing (Speight, 2012). The disadvantages are also evident which include difficulty in controlling subsurface combustion, possibility of low permeability and porosity in the shale formation, low efficiency of recovery, high power consumption, and high risk of aquifer contamination (Fang et al., 2008).

Overall yields from underground retorting is lower than those form aboveground retorting. Aboveground retorting tends to yield gases with better quality, and underground retorting tends to yield liquid hydrocarbon fractions with better quality possibly due to relatively slower and more even heating during in situ retorting process (Speight, 2012).

Some advanced retorting and upgrading processes are being developed and tested in lab-scale. The objectives are to minimize the regressive thermal and chemical reactions that form coke and gases, and to maximize the yield of liquid products. The approaches being researched include lowering heating temperatures, increasing heating rates, shortening residence time durations, and introducing hydrogen transfer/donor agents or solvents (Johnson et al., 2004). Many aspects still need to be improved for commercial-scale production.

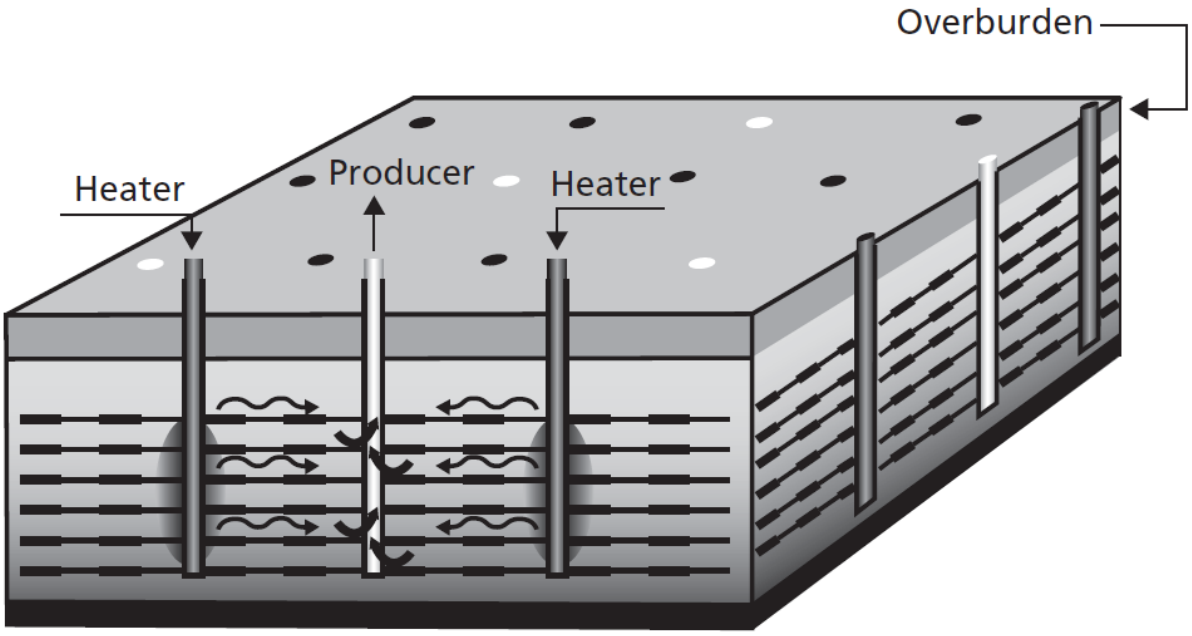

Figure 4. An example of underground (in situ) retorting process, adapted from (Bartis et al., 2005).

The shale oil produced from retorting varies in properties and composition and are usually very unstable. The unstable raw liquid product can cause pipelines clogging, machinery and engine malfunction, increased problem and cost, and overall loss in profits, thus needs to be upgraded to a stable synthetic crude oil before being transported with pipelines and used as conventional

refinery feedstock to produce marketable fuel products (Fathoni and Batts, 1992). The approaches to upgrade raw shale oil include: dewatering and desalting (Speight, 2012); hydrotreatment to decompose sulfur and nitrogen compounds to nonreactive hydrocarbons, H_2S, and NH_3, as well as reduce olefin and diolefin contents to eliminate possible gum formation; strong caustic scrubbing to remove sediment precursors; and modification of chemical and physical characteristics such as adding stabilizer, antioxidants, and metal deactivators (Fathoni and Batts, 1992).

The upgraded shale oil will be transported to a refinery to either obtain middle distillate products such as kerosene, diesel, and jet fuel, or to crack into lighter weight products such as gasoline (Congress, 1980; Lee, 1990).

ENVIRONMENTAL IMPACTS

Oil shale in the ground is generally harmless to environment or human health. Oil shale retorting, unfortunately, has negative environmental impacts if not controlled properly. Predominant waste produced during shale oil extraction makes up to 125% of the volume originally mined, and the disposal could impact a large area of land including potential land erosion and groundwater contamination. Waste water from retorting contains high concentration of complex organic compounds and waste spent shale contains potentially leachable salts and organic pyrolysis products (Routson et al., 1979). During shale gas production, the environmental risks also include aboveground waste water spilling, groundwater contamination due to faulty well construction, uncontrolled gas migration, and chemical leaking during drilling and hydraulic fracturing (Zoback et al., 2010).

Land disturbance is the most serious environmental impact from oil shale retorting. A large aera of land will need to be taken from current uses during production regardless of which retorting

method is used, and there could be permanent ecological effects. Aboveground retorting could change the topographic features from mining and disposal of spent shale. In situ retorting could also disturb the land from surface-based drilling (Bartis et al., 2005). Land disturbance also includes the possible landscape fragmentation, conflicts with agricultural lands and natural areas such as forests, and constructing necessary infrastructure of roads, pipelines, and service areas (Baranzelli et al., 2015). Reduction of soil fertility and decreases of wild habitat usually occurs even after reclamation.

Air pollution is another major environmental impact in oil shale operations. This include: (1) airborne dust particles produced underground blasting, which not only affect local area but also transport to affect father areas before they settle (Xiu et al., 2020); (2) oil shale fly-ash containing high concentrations of various heavy metals, carbonates, alkaline oxides, and harmful organic compounds (Raukas and Punning, 2009; Vallner et al., 2015); (3) greenhouse gas emissions such as H_2S, NH_3, CO, CH_4, and CO_2 during retorting and shale gas production, even though the gas life-cycle emissions are lower than conventional coal or natural gas production (Burnham et al., 2012); (4) acid gases (SO_x and NO_x) emission (Taylor et al., 1982); and (5) volatile organic compound emissions (Robinson, 2014).

Water consumption and water pollution is also a primary factor influencing the environment during oil shale production. Approximately three times of water is needed per unit volume of shale oil produced (Bartis et al., 2005). It includes water requirements for power generation, heating process, refining, dust control, on-site worker demands, and reclamation (Speight, 2012). With oil shale plants near rivers, there is great potential of inorganic salt loading to fresh water, from mine drainage containing sodium, potassium, calcium, magnesium, sulfate, bicarbonate, and chloride salts (Speight, 2012). Depending on the types of shale used in production,

waste water might also contain organic pollutants such as phenols, resorcins, ammonia, pyridines, etc., and are toxic if not removed appropriately (Wan, 2009). In situ retorting can increase the porosity and water absorption of the heated area and pyrolysis products can enter groundwater to deteriorate water quality (Hu et al., 2018). Groundwater quality is also directly impacted by the use of machinery, blasting, fuel, and oil residues during mining process (Raukas and Punning, 2009). Shale gas production generates "flowback water" from fracturing fluid containing salts and other chemicals as well as "produced water" from continuous flow of liquid through the well during production (Estrada and Bhamidimarri, 2016). Both types of wastewater are potential environmental hazards.

Spent shale causes a huge amount of solid waste pollution if not disposed or treated properly. The oxygen- and sulfur-containing compounds in spent shale would produce acidic species which leach to ground water along with dissolved heavy metals (Speight, 2012). The spent shale leachate also contains small amounts of the same soluble pollutants as those in air pollution, affecting local soil quality and water quality in rivers and streams (Bartis et al., 2005). Soil deterioration could occur due to solid waste from oil shale industry (Põllumaa et al., 2001).

Shale oil and gas development has both short-term and long-term effects on ecosystems. It clears the landscape for pad construction and related infrastructure, resulting in loss of native habitats. Land fragmentation, such as pipelines, new roads, transmission lines, and other types of corridors, further increases the habitat loss by altering moisture, temperature, and light which change the species interactions and movement patterns. Noise pollution during exploration and production can affect wildlife communication and transmission. Potential water quantity change and quality declining can affect terrestrial and aquatic species. Habitats and species most at risk

include core forest habitat, sagebrush habitat, vernal pond inhabitants, and stream biota (Brittingham et al., 2014).

The United States Congress introduced federal regulations in the 1960s to limit environmental impacts from oil shale industry development (Speight, 2012). Stricter and more rigidly enforced regulations are yet to be introduced by federal government and state governments to sufficiently protect the environment. Even though many techniques and managements have been developed to diminish the negative environmental impacts from oil shale industry (Bartholomew and Mauter, 2016; Brittingham et al., 2014; Coussens and Martinez, 2013; Eshleman and Elmore, 2013; Estrada and Bhamidimarri, 2016; Ethridge et al., 2015; Nasiri et al., 2017; Vallner et al., 2015; Wan, 2009; Zhang et al., 2019), series of project-based evaluating and monitoring systems still need to be designed and employed (Baranzelli et al., 2015).

ANALYTICAL TECHNIQUES TO CHARACTERIZE ORGANIC MATTER IN OIL SHALES

The structural characterization of oil shales is critical in advancing the method to evaluate the grade of oil shales, understanding the hydrocarbon generation process, and developing better petroleum exploitation strategies and proper disposal or reclamation methods of spent shales. Increasing attention has been paid to characterization of organic matter in oil shales and various analytical methods have been used to analyze oil shale and kerogen samples. The herarchy of experimental techniques for the characterization and structure elucidation of kerogen and related materials has been summarized (Rullkötter and Michaelis, 1990).

Elemental compositions of shales, kerogen, or extracted bitumens are usually determined by elemental analyzers (Bolin et al., 2016). Trace elements can be analyzed by X-ray fluorescence spectrometry (Glikson et al., 1985). Determining the elemental hydrogen, carbon, and oxygen

composition of a kerogen and plotting the atomic hydrogen to carbon (H/C) and oxygen to carbon (O/C) ratios on a van Krevelen diagram is the traditional way to classify the type of the kerogen in a shale (Whelan and Thompson-Rizer, 1993). Isotopic analysis, such as $^{13}C/^{12}C$ and $^{15}N/^{14}N$ ratios, can give information on the general organic matter origin and indicate the geochemical and biochemical cycles through which the elements have passed (Craig, 1953; Rigby and Batts, 1986). X-ray diffraction (XRD) is the principal method used to identify the mineral phases present in oil shales. By measuring the angles and intensities of the X-ray beams diffracted by the crystalline structure, it can provide the quantitative data on crystallized mineral phases of a sample (Suryanarayana and Norton, 1998; Wang et al., 2009). These overall analytical techniques provide general information on the average composition of bulk sample shales.

To characterize detailed structural properties of the organic matter in oil shales, degradative techniques such as chemical degradation and pyrolysis can be employed. Chemical degradation include oxidative, reductive, and cleavage reactions resulting in non-specific products, and selective chemical degradation at bonds such as ester, amide, ether, sulfur, olefinic, aromatic-C, aromatic-O-C bonds, leading to indicative cleavage products (Rullkötter and Michaelis, 1990). Pyrolysis of a shale or kerogen is usually carried out by heating up a small amount of sample in a reactor, and the pyrolysis products will be swept by a carrier gas out of the reactor and to the following instrument for further analyses (van de Meent et al., 1980). Gas chromatography (GC), mass spectrometry (MS), and Fourier-transform infrared spectroscopy (FTIR) are commonly employed to identify the volatile pyrolysis products (Fletcher et al., 2014; Hillier et al., 2013; van de Meent et al., 1980). The non-volatile pyrolysis products can be extracted with organic solvents and analyzed using high-performance liquid chromatography (HPLC) and solution-state nuclear magnetic resonance (NMR) spectroscopy (Fletcher et al., 2014; Zhao et al., 2017). The identified

components of pyrolysates include straight, branched, and cyclic hydrocarbons, alkylaromatic hydrocarbons, sulfur-bearing alkylated aromatic compounds, and alkylphenols. Even though they are minor portions of the whole organic matter, they to some extent proportionally represent the parent structural element concentrations in the kerogen (Engel and Macko, 2013b). Degradative techniques can provide detailed structural information on pyrolysis products and small building units of organic matter in oil shales, but the pyrolysates can undergo secondary reactions and have constitutional features not present in the parent material; therefore the structural information could be unrepresentative and difficult to relate them back to the precursor structure in oil shales.

Kerogen, which is insoluble in organic solvents, comprises the majority fraction of the organic matter in oil shales. The hierarchy of experimental methods to characterize the biological source, elemental composition, functional group/chemical environment, constitutional moieties, building blocks, and 3D-structures of kerogen and related materials was summarized (Rullkötter and Michaelis, 1990) and shown in Figure 5. Spectroscopic techniques are the best means to analyze the chemical environment in order to elucidate the structure of the organic matter in oil shales as a whole. Specifically, ^{13}C solid-state NMR can directly measure the insoluble organic matter without tedious chemical reactions and provide information on the distribution of carbon moieties and how they are connected, making it one of the best non-destructive methods for providing quantitative and comprehensive structural information on oil shales (Cao et al., 2013a; Cao et al., 2013b; Mao et al., 2017a; Miknis, 1992).

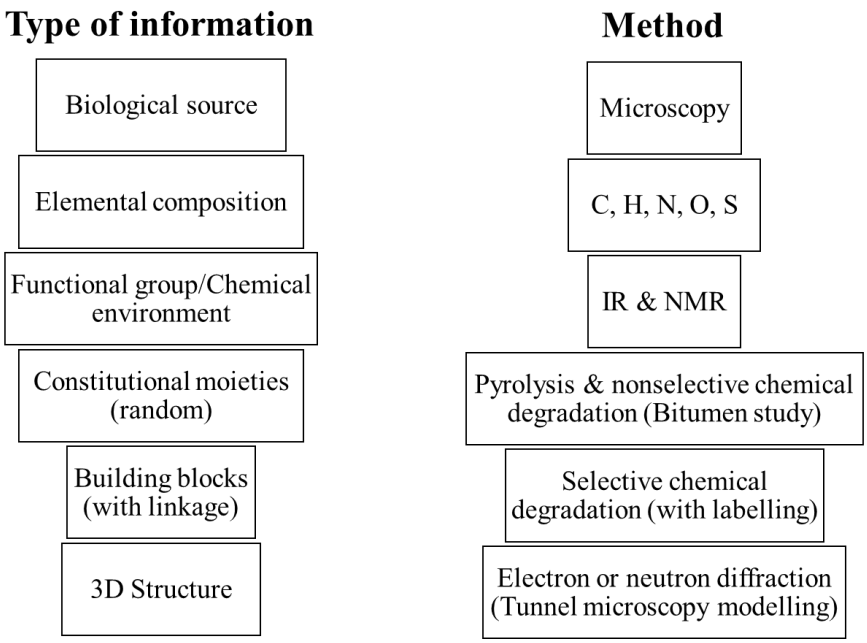

Figure 5. The hierarchy of experimental methods for the characterization and structure elucidation of kerogen and related materials, adapted from (Rullkötter and Michaelis, 1990).

STRUCTURAL PROPERTIES OF THE ORGANIC MATTER IN OIL SHALES

Kerogen is a solid, waxy organic material that is formed with pressure and heat from the Earth acting upon the remains of organisms, it is insoluble in non-polar organic solvents due to the high molecular weight and can yield oil upon heating (Speight, 2012). The chemical composition of kerogen is based on its biochemical source-related mechanical composition, diagenetic modification, and degree of thermal evolution (Engel and Macko, 2013b). Generally, kerogen is a mixture of various nonpolymeric macromolecules containing substantial amounts of carbon and hydrogen, as well as up to 400 heteroatoms (nitrogen, oxygen, and sulfur) for every 1000 carbon atoms (Speight, 2012; Vandenbroucke, 2003). The position of atomic H/C versus O/C of kerogen in the van Krevelen diagram categorizes them into diffent types (Figure 6), which can also

indicates the evolutionary path for kerogen from different precursors and depositional enrivonments (Vandenbroucke and Largeau, 2007).

Type I kerogen usually contains atomic H/C ratio 1.5 or higher, and atomic O/C ratio 0.03 to 0.1 (Vandenbroucke and Largeau, 2007). Type I kerogen is generally derived from lacustrine algae and has rich saturated aliphatic chains and few cyclic or aromatic structures (Speight, 2012). This type of kerogen is not widespread, but the Green River Shale in the Uinta Basin contains the reference Type I kerogen which consists of lacustrine deposit that has been reworked by microorganisms with the remaining constituent lipids and some cuticular vegetal waxes (Durand, 1980a). The high H/C ratio in Type I kerogen corresponds to the long chain n-alkanes (>40 carbons) in the pyrolysis products, oils, and extracts of this type of kerogen and has the highest oil potential among kerogen types (Vandenbroucke and Largeau, 2007).

Type II kerogen contains atomic H/C of 1.3 and O/C ration of 0.15, and a higher level of sulfur (Vandenbroucke and Largeau, 2007). It is usually derived from zooplankton, phytoplankton, or bacterial remains that are deposited in a reducing marine environment (Speight, 2012). There are more cyclic aliphatic and aromatic structures in type II kerogen than that of type I. The n-alkanes in the pyrolysis products and extracts are less than 25 carbons, so the oil-generating potential of type II kerogen is lower than that of type I kerogen at the same level of maturation (Speight, 2012; Vandenbroucke and Largeau, 2007).

Type III kerogen has even lower atomic H/C ratio (<0.8) and higher atomic O/C ratio (>0.2). The organic matter is usually derived from higher terrestial plants rich in lignin. The low hydrogen content and particularly high oxygen content correspond to carbon skeleton of cyclic or heterocyclic and extensive aromatic polycyclic structures (Durand, 1980a; Speight, 2012). High aromatic and heteroaromatic contents result in lower oil-generating potential but higher paraffinic

extracts and gas-generating potential compared to Type II kerogen (Vandenbroucke and Largeau, 2007).

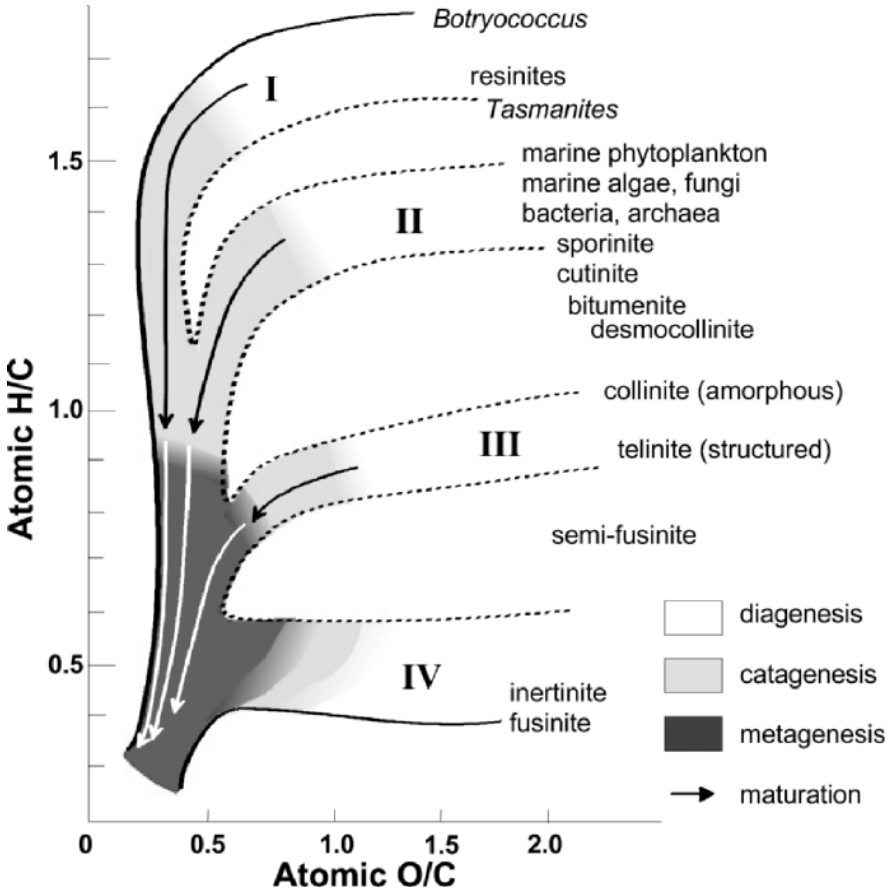

Figure 6. van Krevelen diagram showing the distribution of kerogen types, adapted from (Walters, 2007).

Quantitative characterization of the molecular structures of kerogen and related macromolecular fossil organic matter is helpful in understanding the generation, migration and accumulation of hydrocarbons as the processes on a geological time scale (Rullkötter and Michaelis, 1990). It also potentially aids in predicting oil and gas properties to improve production strategies and to alleviate environmental impacts. The combination of elemental analyses,

degradative analyses of pyrolysis products and bitumens, and non-destructive spectroscopic analyses of raw shale and kerogen, structural characterization has been, to some degree, achieved. Some constitutional models of kerogen have been proposed (Huang et al., 2018; Lille et al., 2003; Orendt et al., 2013; Tong et al., 2016; Ungerer et al., 2015; Wang et al., 2018).

NMR METHODS FOR CHARACTERIZATION OF ORGANIC MATTER IN OIL SHALES

In order to elucidate the molecular structure of the organic matter in oil shale, the research in this dissertation heavily relies on NMR spectroscopic techniques including advanced solid-state NMR, liquid-state NMR, and high resolution magic angle spinning (HRMAS) NMR techniques. This section will introduce all the NMR techniques that have been used in the research.

Advanced solid-state NMR

Advanced solid-state NMR techniques for the characterization of natural organic matter (NOM) and their applications to fossil fuels including oil shale and kerogen samples were summarized and a systematic approach for nondestructively investigating complex NOM was proposed and demmonstrated (Mao et al., 2017a; Mao et al., 2011). The general steps of the approach, shown in Figure 7, is to identify and quantify specific functional groups in the organic structure, determine the proximities or connectivities of specific functional groups, and detect the domains or heterogeneities in the chemical structure (Mao et al., 2011). The solid-state NMR techniques used in this dissertation are described below.

^{13}C multiple cross-polarization magic angle spinning (multiCP/MAS) NMR

The ^{13}C cross polarization/magic angle spinning (CP/MAS) method is the most widely used solid-state NMR technique in source rock organic matter studies. It has provided abundant qualitative or semi-quantitative structural information (Barron, 1982; Dennis et al., 1982; Kelemen

et al., 2007a; Lille et al., 2003; Miknis et al., 1984; Trewhella et al., 1986; Wang et al., 2017; Wei et al., 2005; Werner-Zwanziger et al., 2005; Witte et al., 1988; Žujović et al., 1995). Simple ^{13}C CP/MAS detects the magnetization transferred from more abundant ^{1}H nuclei to less abundant ^{13}C nuclei, but the magnetization transfer is more efficient for the protonated carbons than non-protonated carbons or mobile segments due to their weaker H-C dipolar couplings, so the less efficiently transferred magnetization will show underestimated signals in the spectra. Along with other shortcomings including spinning sidebands, baseline distortion, and ambiguous assignments, the CP/MAS NMR spectra are not quantitative (Mao et al., 2000).

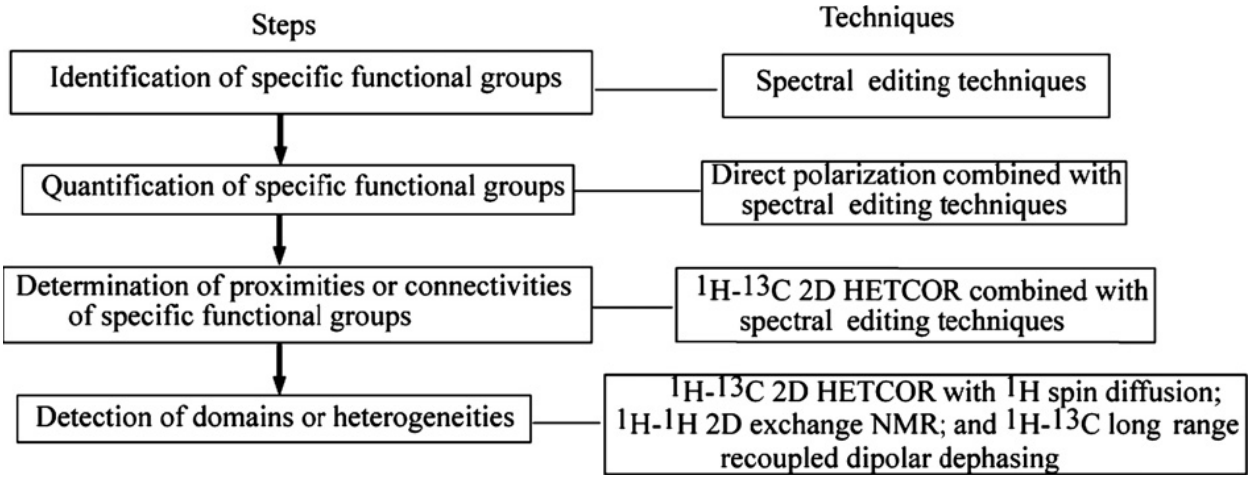

Figure 7. Systematic advanced solid-state NMR techniques for characterizing structures and heterogeneities in NOM, adapted from (Mao et al., 2011).

In order to obtain quantitative NMR spectra, the traditionally reliable way is to use direct polarization/magic angle spinning (DP/MAS) with long enough recycle delays between scans that allows complete longitudinal (T_1) relaxation of the magnetization to the z-axis. However, DP/MAS is very time-consuming when T_1 is long which is usually the case for complex organic materials (Mao et al., 2000). Johnson and Schmidt-Rohr developed a simple robust high spinning speed

multiple-ramped amplitude cross polarization/magic angle spinning (multiCP/MAS) method to get quantitative ^{13}C NMR spectra with better signal-to-noise ratios than DP/MAS while saving much experimental time (Figure 8). In the multiCP/MAS pulse sequence, repeated blocks of CP (~1 ms) separated by periods of duration t_z (~0.5 s) is used, the ^{1}H magnetization can recover to near-equilibrium value during t_z and reverses most of the ^{1}H magnetization loss during CP period. The local ^{1}H magnetization loss near ^{13}C due to the polarization transfer to ^{13}C is canceled by ^{1}H spin diffusion from the surrounding spins (Johnson and Schmidt-Rohr, 2014). MultiCP/MAS has performed very well on crystalline model compounds such as amino acid derivatives as well as complex organic matter including plant matter, chars, and humic acid in getting quantitative spectra comparable to DP/MAS (Johnson and Schmidt-Rohr, 2014).

^{13}C multiCP/MAS plus dipolar dephasing (multiCP/DD)

Dipolar dephasing is usually combined with multiCP/MAS to remove signals from any nucleus that is directly bonded to proton. This spectral editing technique selects signals from non-protonated carbons by the faster dephasing (decaying) of the magnetization originated from any species strongly dipolar coupled to proton while decoupling gate is off. Carefully choosing the wait time and placing the gated decoupling delay allows full removal of the signals from protonated carbons (Mao and Schmidt-Rohr, 2004a; Opella and Frey, 1979).

^{13}C chemical shift anisotropy (CSA) filter

^{13}C CSA filter was introduced to select signals of alkyl carbons and suppress those of aromatic carbons (Mao and Schmidt-Rohr, 2004b). This technique is based on the carbon bonding symmetry, as shown in the magnitude of the chemical shift anisotropy (CSA). Because of the tetrahedral bonding symmetry, the CSAs of sp^3-hybridized carbons are much smaller than the CSAs of planar sp^2-hybridized and linear sp-hybridized carbons. When the CSA is recoupled using

a few rotation-synchronized π-pulses, the magnetization of carbons with larger CSAs decays faster. Simple three- or five-pulse CSA-recoupling sequences with "γ-integral" are used to totally suppress the magnetization of all sp^2- and sp-hybridized carbons. This technique is particularly useful in separating the overlapping (usually between 90-120 ppm) signals of sp^2- and sp^3-hybridized carbons, e.g., anomerics (O-C-O) and aromatics, in complex NOM when they cannot be distinguished by their isotropic chemical shifts (Mao et al., 2017b; Mao and Schmidt-Rohr, 2004a, b).

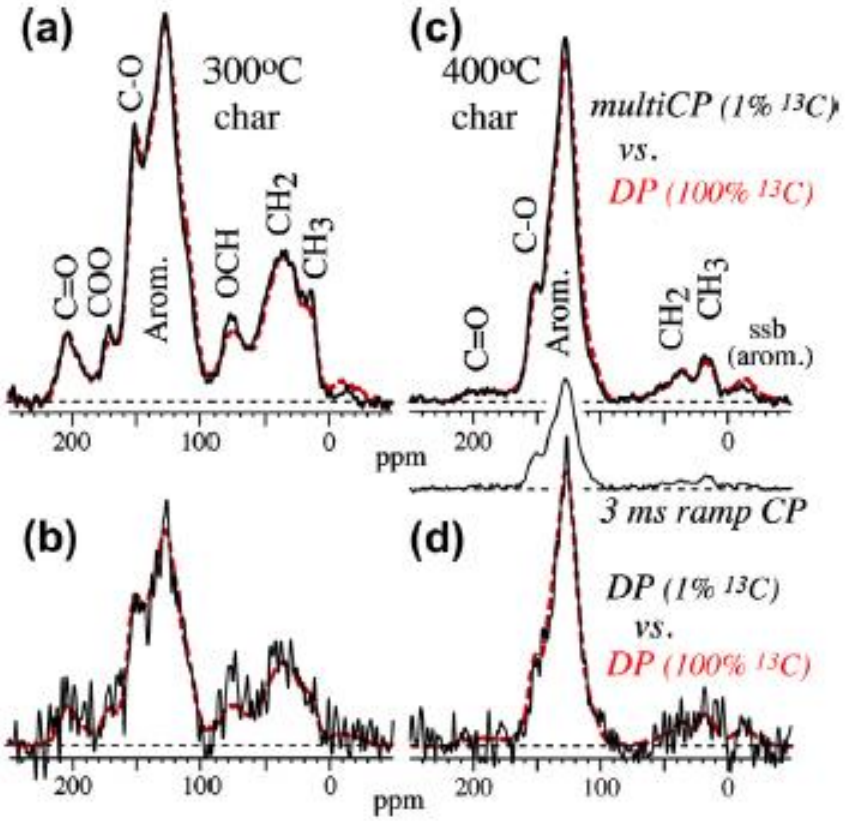

Figure 8. An illustration of multicp/MAS as a reliable quantitative ^{13}C NMR method for unlabeled solids, adapted from (Johnson and Schmidt-Rohr, 2014).

^{13}C CSA filter combined with dipolar dephasing (CP/TOSS/DD/CSA filtered)

^{13}C CSA filter technique can be combined with dipolar dephasing technique in order to select non-protonated mobile sp^3-hybridized carbon signals. A four-π-pulse total suppression of sidebands (TOSS) is inserted before detection to remove sidebands (Mao et al., 2017a).

CH_n selection

Signals of immobile CH_2 and CH groups (CH_n) can be selected in a simple spectral editing experiment similar to the scheme previously proposed (Wu et al., 1994). Two spectra are recorded, and a third spectrum is generated by their difference displaying the signals of immobile CH_n groups with a small CH_3 contribution. The first is a CP/TOSS spectrum with a short CP of 50 μs, showing the signals of protonated carbons in immobile segments with some residual signals from quaternary carbons. The second is a CP/TOSS spectrum with a short CP of 50 μs and 40 μs dipolar dephasing, showing only the residual signals from quaternary carbons or mobile segments including CH_3 groups with more than 50% efficiency (Mao et al., 2007). The third spectrum presents the result of the signals of the first spectrum minus the signals of the second spectrum.

Two-dimensional ^{1}H-^{13}C heteronuclear correlation (2D HETCOR) NMR

Correlation of ^{13}C chemical shifts with ^{1}H chemical shifts can reveal more structural information than 1D ^{13}C or ^{1}H spectrum (Mao et al., 2001). Since ^{1}H-^{13}C dipolar couplings can provide correlation between internuclear distance on about 0.6 nm, 2D HETCOR NMR is able to reveal close proximity of different functional groups (Bronnimann et al., 1992; Mao et al., 2017a). Combined with dipolar dephasing, 2D HETCOR NMR is especially useful in detecting the correlation between nearest protons and the non-protonated carbon functional groups such as COO/NC=O (Mao et al., 2012). 2D HETCOR NMR can also be used with ^{1}H spin diffusion in order to identify domains and heterogeneities in NOM structure (Mao and Cao, 2011), where

"domain" refers to similar types of chemical compounds spatially segregated from others (such as polysaccharide or lignin) with the diameter larger than 5 nm and "heterogeneity" refers to that of diameter less than 5 nm (Mao et al., 2017a).

Liquid-state NMR spectroscopy

Liquid-state NMR is one of the routine techniques for identifying the structure of either pure or complex organic compounds once they are dissolved in a chosen organic solvent. A series of liquid-state NMR techniques have been developed and improved over more than half a century (Lambert et al., 2019). The experimental methods used in this dissertation included 1D proton NMR, 2D ^{1}H-^{1}H correlation spectroscopy (COSY) to detect correlation between protons sharing a J-coupling through bond, total correlation spectroscopy (TOCSY) to detect correlation of protons within a chain or network of the bonding even when they do not share a J-coupling, and ^{1}H-^{13}C heteronuclear single quantum coherence (HSQC) to detect the correlation of carbons with directly bonded protons.

High resolution magic angle spinning (HRMAS) NMR spectroscopy

HRMAS is a technique suitable for investigating interfaces between a translationally mobile (liquid) and an immobile or less mobile (solid support, gel, microparticle), more particularly for detecting NMR resonances from a conformationally mobile chemical moiety, grafted to or interacting with the immobile phase. It allows the application of liquid-state NMR experiments to samples that are not fully soluble and contain solids. The signals are from species in contact with the solvent system, leading to spectra similar to liquid-state NMR spectra. It has been applied to study gels, ligand, soil, and kerogen (Alam and Jenkins, 2012; Iqbal et al., 2010; Polito et al., 2008; Salmon et al., 2011; Simpson et al., 2001).

All the pulse sequence programs available for liquid-state NMR experiments can be employed in HRMAS experiment, making it a very useful technique in studying those samples that give none or very poor at all signals under the regular solvent condition. It combines the techniques in liquid-state NMR with the magic angle spinning method in solid-state NMR.

CHAPTER II

SURVEY INVESTIGATION OF ORGANIC MATTER IN OIL SHALES

INTRODUCTION

The organic matter in oil shale, mainly in the form of kerogen, is closely related to the quantity and quality of petroleum and gas generated by the oil shale. Kerogen contains essential information about the geothermal history of the shale formations and can reflect the past environments, climates, and biota (Vandenbroucke and Largeau, 2007). Kerogen is usually isolated for analytical investigation, especially NMR study, due to its low concentration in sedimentary rocks. The typical isolation procedures involve the treatment with non-oxidant acids to break down the mineral components and remove the paramagnetic materials (Vandenbroucke and Largeau, 2007). In previous studies, the NMR spectra of raw shale and the corresponding kerogen samples showed similar chemical shift distributions with generally more resolved peaks in the spectra of kerogen samples due to the more concentrated organic matter after the removal of paramagnetic materials and some soluble fraction (Cao et al., 2013b). However, difference has been observed such as the depletion of oxygen-substituted carbons, indicating the destruction of carbohydrates in acid treatment during the kerogen isolation (Maciel and Dennis, 1981). It is reasonable to avoid the kerogen isolation process and study raw shale if the shale contains a decent concentration of kerogen and negligible amount of paramagnetic materials to yield well-resolved NMR spectra.

The world-wide shale formations introduced in the last chapter represent their own depositional and thermal histories. To gain an overall picture of the structural characteristics of

the organic matter from typical shales formations and provide more information on the development of oil exploration, shale samples collected from some famous sites were investigated.

MATERIALS AND METHODS

Shale samples

The 22 shale samples investigated in this chapter were collected and provided by the United States Geological Survey (USGS). The shale samples were collected from heavily studied, often visited sites or from mines that are currently or were previously in operation. The samples were taken from a particularly organic-rich interval of the formation in an outcrop or at a roadcut. This ensured the high organic matter concentration for directly measuring the raw shale samples without the tedious process of kerogen isolation. The samples were crushed to small pieces, pulverized, and sieved (-60 mesh) to obtain homogenized powders for NMR analysis. They were from various geological times including Eocene, Late Cretaceous, Jurassic, Permian, Carboniferous, Devonian-Mississippian, Ordovician, and Cambrian. These samples contained different mineral components and types of kerogen and were collected at different locations including Sweden, USA, Israel, Jordan, Australia, Brazil, UK, and Estonia. Sample information was listed in Table 1.

Solid-state NMR spectroscopy

All ^{13}C NMR analyses were performed on a Bruker Avance 400 spectrometer at 100 MHz for ^{13}C. Samples were packed in 4-mm-diameter zirconia rotors with Kel-F caps, and experiments were run in a double-resonance probe head and the rotor was spun at magic angle of 54.7° to the direction of the magnetic field. The ^{13}C chemical shifts were referenced to tetramethylsilane (TMS), with $^{13}COO^-$ labeled glycine at 176.49 ppm as a secondary reference.

Table 1. Information of 22 shale samples.

Sample name	Location	Age	Mineralogy	TOC (wt. %)	Hydrogen index (mg-HC/g-TOC)
Alum Shale	Vastmanlands, Sweden	Cambrian	Quartz, illite	12.4	465
Boquillas shale	Val Verde County, Texas, USA	Late Cretaceous	Calcite, quartz, kaolinite	5	619
Brecciated oil shale	NW Colorado, USA	Eocene	Carbonate, quartz, feldspar	16	935
Cow Ridge B-marker	NW Colorado, USA	Eocene	Mixed-layer clays, quartz	8	732
Dawsonitic oil shale	NW Colorado, USA	Eocene	Quartz, feldspar, dawsonite	9.9	805
Garden Gulch Member	NW Colorado, USA	Eocene	Illite, carbonate	10	821
Ghareb (Israel)	Hadarom, Israel	Late Cretaceous	Carbonate	15.8	705
Ghareb (Jordan)	Al Karak, Jordan	Late Cretaceous	Carbonate, clay	20.9	759
Glen Davis	New South Wales, Australia	Permian	Quartz	56.2	939
Green River (GR-42)	NW Colorado, USA	Eocene	Carbonate, quartz, feldspar	25.4	854
Irati Formation	Parana, Brazil	Permian	Quartz, illite	11	730
Kimmeridge Clay (Blackstone)	England, UK	Jurassic	Claystone	53.8	604
Mancos shale	Delta County, Colorado, USA	Late Cretaceous	Illite, quartz, albite	3.2	187
Narva-E mine Kukersite	Estonia	Ordovician	Carbonate, clay	44.7	982
New Albany Shale (Clegg Ck)	Indiana, USA	Devonian-Mississippian	Quartz, illite	14.9	549
Phosphoria Fm (Retort Shale)	Montana, USA	Permian	Quartz, ML clays	28	469
Pumpherston	Scotland, UK	Carboniferous	Quartz, kaolinite	27.7	512
Pyrolysis standard	NW Colorado, USA	Eocene	Carbonate, quartz, feldspar	13.3	899
Timahdit Morocco Oil Shale	South-central Morocco	Late Cretaceous	ML clays, carbonate	9.5	560
Uinta Basin (Mahogany zone)	Utah, USA	Eocene	Carbonate, quartz, feldspar	29.7	1003
Uteland Butte shale	NW Colorado, USA	Eocene	Clay, quartz, carbonate	6	893
Woodford shale	Carter County, Oklahoma, USA	Devonian-Mississippian	Quartz, dolomite, illite	8	550

^{13}C multiple cross-polarization magic angle spinning (multiCP/MAS) NMR

The ^{13}C multiCP/MAS technique was employed to obtain quantitative solid-state ^{13}C MAS NMR spectra with good signal-to-noise ratios while measuring time was significantly reduced in contrast to direct-polarization (DP/MAS) NMR (Johnson and Schmidt-Rohr, 2014). The spectra were collected at a spinning speed of 14 kHz, with very small (<3%) spinning sidebands that have minimal overlap with centerbands. The 90° ^{13}C pulse length was 4.2 μs. Scan numbers varied based on the carbon contents in the samples to achieve reasonable S/N ratio.

^{13}C multiCP/MAS plus dipolar dephasing (multiCP/DD)

To obtain quantitative structural information on non-protonated carbons and mobile segments, ^{13}C multiCP/MAS combined with dipolar dephasing was applied. Most experimental conditions were the same as for the ^{13}C multiCP/MAS method except that a recoupled dipolar dephasing time of 68 μs was applied (Mao and Schmidt-Rohr, 2004a). The same scan numbers were collected as in the multiCP/MAS technique of each sample.

RESULTS

The ^{13}C multiCP/MAS and multiCP/DD spectra of 22 shale samples are presented in Figure 9. The multiCP/MAS spectra showed the signals of all carbon moieties while multiCP/DD spectra showed the signals of non-protonated carbons and mobile segments in the organic matter of the shale samples.

In multiCP/MAS spectra of all the samples, there were two major bands centered around 30 ppm and 135 ppm which were assigned to aliphatic (alkyl) carbons and aromatic carbons, respectively. The intensive aliphatic band indicated a significant contribution of methylene groups. Specific functional groups were assigned to corresponding chemical shift regions, 0-48 ppm was assigned to nonpolar alkyls, 48-65 ppm to OCH_3 and NCH, 65-93 ppm to O-alkyls, 148-165 ppm

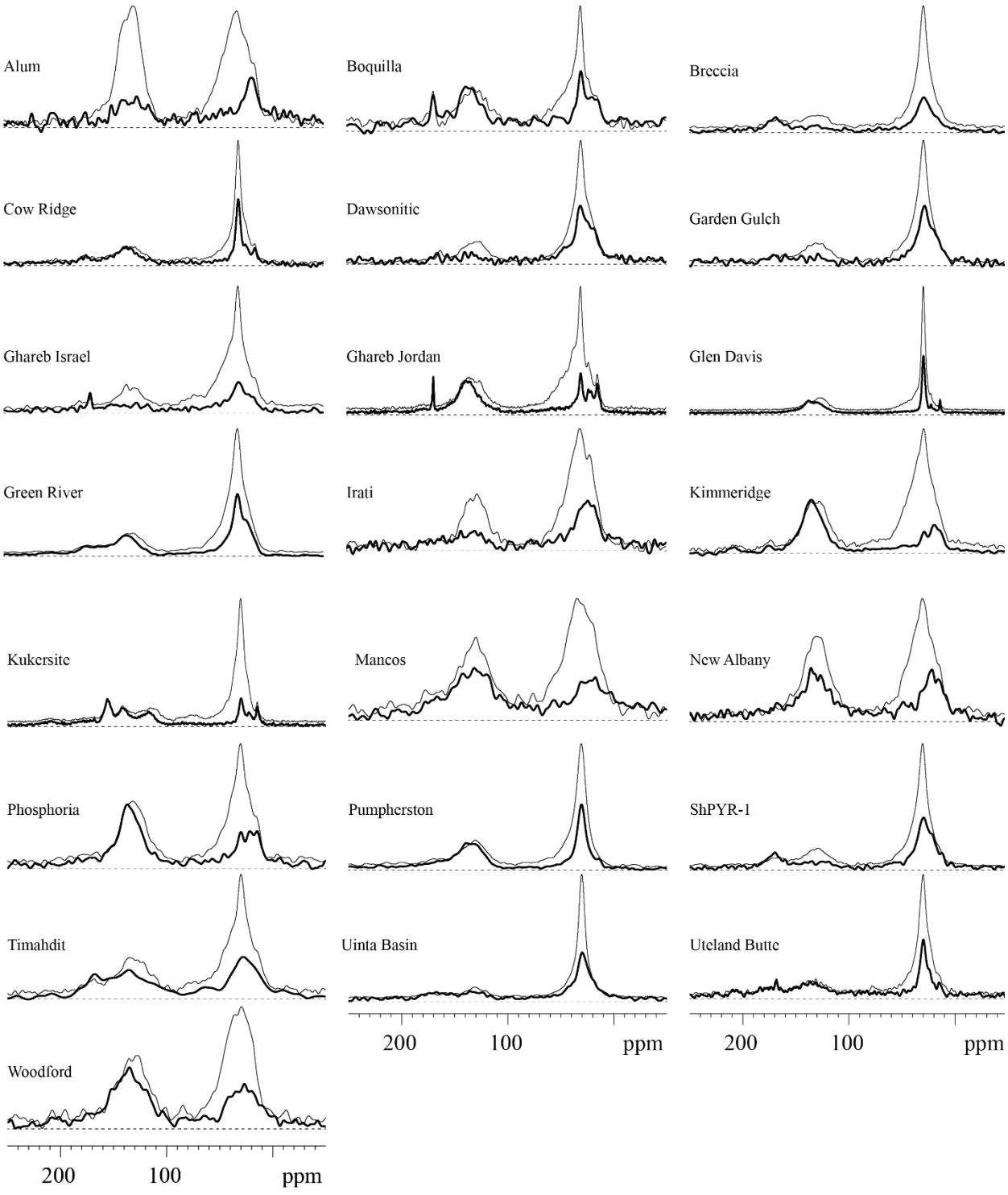

Figure 9. MultiCP/MAS (black lines) and multiCP/DD spectra (bold lines) of 22 shale samples.

to aromatic C-O, 165-190 ppm to COO and NC=O, and 190-220 ppm to ketones and aldehydes.

The multiCP/DD spectra (bold lines) in Figure 9 selectively presented the signals from the non-protonated carbon moieties and mobile segments. The broad aliphatic bands centered at 30 ppm confirmed the presence of methylene groups, which was consistent with the bands in multiCP/MAS spectra. All these band heights were lower in multiCP/DD spectra than those in multiCP/MAS spectra due to the suppression of signals at this region other than the signals from mobile segments. The shoulders at around 20 ppm in the multiCP/DD spectra of the samples were more resolved than those in multiCP/MAS spectra, corresponding to the contribution of methyl groups to the aliphatic bands. The methyl group signals were better separated and shown in the spectra of some samples such as Boquilla sample, Cow Ridge sample, Dawsonitic sample, Jordanian Ghareb sample, Glen Davis sample, Green River sample, Irati sample, Kukersite sample, Phosphoria sample, and Utland Butte sample, indicating more distinctive methyl moieties in their molecular structures.

In the aromatic region, the bands in multiCP/DD spectra were generally lower than those in multiCP/MAS spectra due to the presence of signals from only the non-protonated aromatic carbons. The signals at downfield to the aromatic region confirmed the existence of ester structures in some of the shale samples. The relative proportion of protonated and non-protonated aromatic carbons, as well as other carbon moieties can be calculated using the chemical shift assignment and integration of multiCP/MAS spectra and multiCP/DD spectra.

To demonstrate the composition of carbon moieties, the percentages of different carbon moieties were calculated following the systematic calculating approach (Mao et al., 2011), Briefly, the percentages of ketones and aldehydes, COO/N-C=O, and aromatic C-O groups were directly integrated from multiCP/MAS spectrum at chemical shift regions 220-190 ppm, 190-165 ppm,

and 165-148 ppm, respectively. The percentage of Aromatic C-C plus aromatic C-H was integrated from multiCP/MAS spectrum at chemical shift region 148-93 ppm, and then integral between 148-93 ppm from the multiCP/DD spectrum was obtained and divided by 0.93 (dipolar dephasing efficiency), in order to separate non-protonated aromatic C-C and protonated aromatic C-H. The total percentage of OCH, OCH_2, and quaternary OC (OC_q) was integrated from multiCP/MAS spectrum at chemical shift region 93-65 ppm, and the percentage of OC_q was obtained from integral between 93-65 ppm in multiCP/DD spectrum. The percentage of OCH_3 plus aromatic NCH was integrated from multiCP/MAS spectrum at chemical shift region 65-48 ppm, and then percentage of OCH_3 was separated by integrating from multiCP/DD spectrum at 65-48 ppm and divided by its dipolar dephasing efficiency 0.65. The percentage of alkyls was integrated from multiCP/MAS spectrum at chemical shift region 48-0 ppm, and CCH_3 was calculated by integral between 24-0 ppm from the multiCP/DD spectrum divided by its dipolar dephasing efficiency 0.65. The different between alkyls and CCH_3 was referred as other alkyls in Table 2, which was mainly CCH_2C in our samples.

The relative proportions (%) of carbon moieties in 22 oil shale samples were shown in Table 2 and the functional group distribution in the organic matter of the same shale samples were illustrated in Figure 10. The relative proportions of different functional groups presented quantitative structural information that was consistent with what was shown in spectra, such as the predominant functional groups being alkyls and aromatics. However, Table 2 also provided more information regarding what types of alkyl groups and their percentages. Based on chemical shifts in both multiCP/MAS and multiCP/DD spectra, the alkyl groups were separated into OC_q (quaternary carbon connected to oxygen), OCH and OCH_2 (tertiary or secondary carbon connected

Table 2. Relative proportions (%) of carbon moieties in 22 oil shales calculated using ^{13}C multiCP/MAS and multiCP/DD spectra.

Chemical shift (ppm)	220-190	190-165	165-148	148-93		93-65		65-48		48-0	
	Ketone and aldehyde	COO and NC=O	Arom. C-O	Arom. C-C	Arom. C-H	OC_q	OCH and OCH_2	OCH_3	NCH	CCH_3	Other alkyls
Alum	0.8	1.6	4.4	4.0	37.1	0.5	2.9	0.7	5.6	5.4	37.0
Boquillas	0.6	5.1	1.9	20.0	8.4	1.1	1.4	2.0	5.9	11.4	42.2
Breccia	0.0	3.5	3.7	3.0	9.6	0.8	1.5	1.3	3.2	5.8	67.6
Cow Ridge	2.1	3.9	4.0	15.9	3.9	2.0	2.4	2.2	2.1	10.8	50.7
Dawsonitic	0.5	1.5	3.7	1.1	17.7	0.3	1.8	0.9	4.1	6.3	62.1
Garden Gulch	1.5	3.0	3.4	1.8	16.3	0.2	2.4	1.0	5.4	5.8	59.2
Ghareb Israel	0.0	3.0	2.0	2.4	14.1	0.7	6.0	1.3	7.3	3.2	60.0
Ghareb Jordan	0.4	3.3	3.0	18.5	7.0	1.0	2.0	2.0	6.5	10.2	46.1
Glen Davis	0.2	0.7	1.9	15.6	6.3	0.1	0.6	1.1	3.0	5.2	65.3
Green River	0.9	3.5	3.5	9.4	6.4	1.2	1.7	2.0	4.6	8.9	57.9
Irati	1.3	1.5	2.3	2.9	24.2	0.5	1.6	1.2	5.8	6.1	52.6
Kimmeridge	0.5	1.6	2.4	17.4	10.4	1.4	2.8	2.0	5.1	6.8	49.6
Kukersite	2.0	2.7	7.3	12.3	6.9	1.1	3.7	0.7	2.9	5.7	54.7
Mancos	2.4	4.8	5.5	20.4	8.9	2.7	2.3	3.1	4.3	11.8	33.8
New Albany	1.2	1.9	4.5	8.0	28.6	0.7	2.8	0.8	4.7	5.6	41.2
Phosphoria	1.3	3.6	4.2	23.3	10.0	1.3	1.4	1.5	3.8	12.8	36.8
Pumpherston	2.2	3.5	4.2	14.2	7.4	0.7	2.6	1.5	4.0	5.2	54.5
ShPYR-1	1.3	4.3	3.7	2.1	13.9	0.4	2.1	1.1	4.6	5.3	61.2
Timahdit	0.6	4.1	4.2	5.1	18.9	1.0	4.0	1.1	5.5	4.1	51.4
Uinta Basin	0.6	3.5	3.5	2.7	9.4	0.5	1.7	1.1	3.1	5.2	68.7
Uteland Butte	1.9	6.2	3.5	11.4	3.4	2.2	2.7	1.5	2.7	7.2	57.3
Woodford	1.6	2.2	5.2	20.1	10.0	1.7	2.3	1.4	5.6	8.8	41.1

to oxygen), OCH_3 (methoxy group) and NCH, CCH_3 (methyl group), and other alkyl groups that were not included, and aromatic groups were separated into aromatic C-O, aromatic C-C, and aromatic C-H.

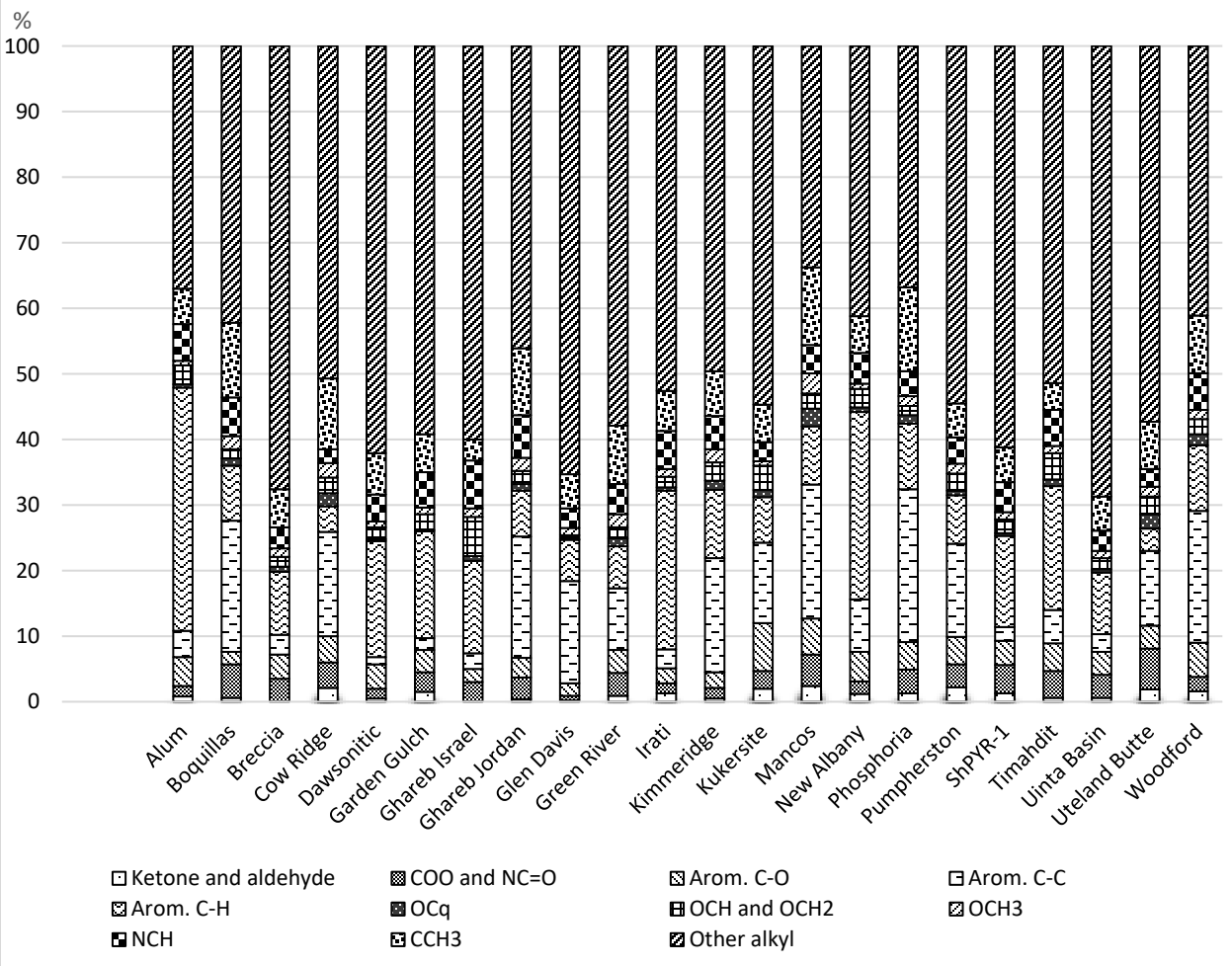

Figure 10. Functional group distribution in the organic matter of 22 shale samples.

All types of alkyl carbons accounted for 52%-80% of organic carbons in all the shale samples, with Alum sample being the lowest and Uinta Basin sample being the highest. This confirmed what was shown in Figure 9. that all the shale samples had significant signal bands at the aliphatic region in the multiCP/MAS spectra. On the other hand, aromatic carbons constituted 16%-46% of organic carbons in the samples measured, with Uinta Basin sample being the lowest and Alum sample being the highest, which is the opposite to alkyl carbon percentages. Among all types of aromatic carbons, Uteland Butte sample had the smallest proportion of aromatic C-H (3.4%) and Alum sample had the largest (37%); Dawsonitic sample had the smallest proportion of aromatic C-C (1.1%) and Phosphoria had the largest (23%); and Glen Davis sample had the smallest proportion of aromatic C-O (1.9%) and Kukersite sample had the largest (7.3%). All the shale samples had small proportion of COO and/or NC=O functional groups (0.7%-6.2%) and negligible proportion of ketone and/or aldehyde functional groups (0%-2.4%).

DISCUSSION

The shale samples measured were from various geological times which would naturally result in different thermal maturities of the shales. Thermal maturity is the extent of temperature–time driven reactions, which are responsible for the conversion of sedimentary organic matter to petroleum or cracking of oil to gas. It reflects the temperature history of the source rock in the subsurface and estimates its petroleum generating potential (Mani et al., 2017). The temperature at which the rate of hydrocarbon generation reaches its maximum (S_2 peak) in Rock-Eval pyrolysis is termed T_{max}. It has been used as a thermal maturity parameter. However, mineral matrix effect, heavy bitumen carryover, weathering, and uranium irradiation can cause inaccuracy of its thermal maturity estimation (Yang and Horsfield, 2020). Vitrinite reflectance (R_o), which measures the percentage of incident light reflected from the surface of vitrinite particles, is the conventional

method to characterize the maturity and thermal history of a sedimentary rock (Fang and Jianyu, 1992; Tissot and Welte, 1984). A linear correlation between vitrinite reflectance (R_o 0.29%-1.4%) and aromaticity derived from ^{13}C CP/MAS NMR spectra was reported for Type II kerogen samples (Werner-Zwanziger et al., 2005). The result indicated that more aromatic carbon percentage from the spectra corresponded to being more thermally mature. This is consistent with our result that the sample with the highest percentage of aromatic carbons (Alum) is from the oldest geological time, the Cambrian Period, while the sample with the lowest percentage of aromatic carbons (Dawsonitic) is from the relatively youngest geological time, the Eocene Epoch of the Paleogene Period. It proved the potential ability of quantitative ^{13}C solid-state NMR spectral data of oil shale as a complementary thermal maturity indicator besides T_{max} and vitrinite reflectance.

Petroleum (oil and gas) generating potential of oil shale and other organic-rich sediments is one of the most important concerns of geochemical studies. Besides the external factors such as grain size of shales, pyrolysis temperature, heating rate, and pyrolysis atmosphere (Ahmad and Williams, 1998; Jaber et al., 1999; Nazzal, 2002, 2008; Williams and Ahmad, 1999), the shale oil yield inherently depends on the amount of kerogen contained in the corresponding source rock, i.e., the organic carbon content, as well as the structure of the kerogen (Miknis and Conn, 1986). High petroleum generating potential is generally supported by the factors such as high total carbon content (TOC), high hydrogen index, early to mid-thermal maturity, high extractable organic matter content (bitumen content) and hydrocarbon yield, as well as high pyrolysis (Rock-Eval) S_1 value plus S_2 value (Gao et al., 2016; Hakimi et al., 2010; Wan Hasiah, 1999).

By comparing ^{13}C CP/MAS NMR data and modified Fischer assay results, the petroleum generating potential of oil shale was found to be linearly related to the aliphatic carbon content, i.e., a larger proportion of aliphatic carbon in a shale sample would lead to a higher pyrolytic oil

yield, independent of the geological age, depositional environment and location of the shale (Miknis et al., 1982a). More specifically, methylene and methine carbons were found to be directly related to oil yield while other aliphatic carbons, together with carbonyl and carboxyl carbons, were related to gas production (Kuangzong et al., 1991). After analysis and calculation, solid-state ^{13}C NMR spectra can also reflect the hydrogen index, thermal maturity, hydrocarbon yield of the organic matter from oil shale which are all related to the petroleum generating potential, making it a fast, non-destructive, and reliable method to predict the petroleum generating potential of oil shales and other organic-rich sediments (Longbottom et al., 2016; Miknis et al., 1982b).

There are multiple characteristics to determine the quality and the price of crude oil, but the most important ones are density and sulfur content. The light (lower density, or higher degrees of API gravity) and sweet (lower sulfur content, $S \leq 0.5\%$ mass) crude oils are high quality and priced the highest, and the heavy and sour ($S \geq 3\%$ mass) crude oils are priced the lowest (Stratiev et al., 2010). While sulfur content can be measured with elemental analysis, the density or API gravity can be predicted from spectroscopic data (Abbas et al., 2012; Aske et al., 2001; Morgan et al., 2014; Stasiuk and Snowdon, 1997).

Since the quality of shale oil is closely related to the types of the hydrocarbons (saturated hydrocarbons, aromatic hydrocarbons, asphaltenes, and resins) (Abbas et al., 2012; Aske et al., 2001), the hydrocarbon composition highly relies upon the organic matter of the source rock, which makes advanced solid-state ^{13}C NMR method a great candidate for predicting the quality of crude oil generate by oil shale, based on the organic structural characteristics of the source rock.

In this chapter, solid-state ^{13}C NMR multicp/MAS and multicp/DD techniques have proven their ability to quantify different carbon moieties of the organic matter in oil shales (Table 2). In the following chapters, more advanced solid-state ^{13}C NMR experiments with spectral editing

techniques, as well as two-dimensional techniques, liquid-state NMR techniques, and HRMAS NMR techniques will be applied to some chosen shale samples to address specific issues.

CHAPTER III

EFFECT OF HETEROATOM CONTENT ON KEROGEN STRUCTURE

INTRODUCTION

The majority organic carbon in oil shale is in the form of kerogen which is insoluble in common inorganic and organic solvents and represents the largest repository of organic matter on earth (Durand, 1980b; Vandenbroucke and Largeau, 2007). The hydrogen, carbon, and oxygen contents of kerogen are used to determine kerogen types by plotting the atomic H/C and O/C ratios in a van Krevelen diagram (Engel and Macko, 2013a). The different elemental ratios provide information on the relative amount of liquid oil or natural gas that the kerogen will generate during thermal decomposition (Speight, 2012). Oil shales of different origins generally have different heteroatom contents and elemental ratios, which lead to various linkages between functional groups and thus different structural properties (De Leeuw and Largeau, 1993; Engel and Macko, 2013a). Abundant oxygen content could indicate the presence of O-containing functional groups such as phenols, esters, ethers, and carboxylic acids. Organic sulfur can be present in the form of sulfoxide, sulfone, aliphatic sulfur, and aromatic sulfur (Wang et al., 2017). While the elemental analysis may suggest overall chemical composition, spectroscopic methods can provide much more detailed and comprehensive structural information. Specifically, solid-state NMR can provide quantitative structural information and is one of the best methods for non-destructive characterization of oil shale and kerogen given their insolubility in organic solvents.

The ^{13}C cross polarization/magic angle spinning (CP/MAS) method is the most widely used solid-state NMR technique in source rock organic matter studies. For instance, it has been

applied to investigate structures of Green River oil shale kerogen (Trewhella et al., 1986), kerogen from Tertiary deposits in Queensland, Australia (Miknis et al., 1984), Aleksinac oil shale kerogen (Žujović et al., 1995), Estonian kukersite kerogen (Lille et al., 2003), and Australian Glen Davis shale (Barron, 1982). This technique was also applied in studying thermal alteration of Cretaceous black shale kerogen (Dennis et al., 1982), thermal evolution of a group of kerogen samples from China (Wei et al., 2005), and thermal maturity of the New Albany shale (Werner-Zwanziger et al., 2005), usually along with Rock-Eval pyrolysis and vitrinite reflectance (Witte et al., 1988). It also has been combined with X-ray photoelectron spectroscopy (XPS) to characterize organic nitrogen and sulfur structures in oil shale kerogens (Kelemen et al., 2007a; Wang et al., 2017). Solid-state NMR has significantly advanced knowledge on oil shales, and ^{13}C CP/MAS has provided abundant qualitative or semi-quantitative structural information. However, shortcomings of simple ^{13}C CP/MAS include spinning sidebands, baseline distortion, and ambiguous assignments, and quantitative information cannot be obtained due to those or other limitations. Systematic advanced solid-state NMR techniques (Cao et al., 2013b; Mao et al., 2017a; Mao et al., 2011) have been developed and applied to study natural organic matter including shales in order to make quantitative measurements (Cao et al., 2013a), better functional group assignments (Mao et al., 2010), and aromatic cluster size estimation (Mao and Cao, 2011).

While several studies have been conducted on the extractable organic fraction of Estonian kukersite, Glen Davis torbanite, and Ghareb marinite deposits using gas chromatography-mass spectrometry (GC-MS), Fourier-transform infrared spectroscopy (FTIR), and X-ray absorption near-edge structure (XANES) spectroscopy (Audino et al., 2001; Blokker et al., 2001; Derenne et al., 1988; Grice et al., 2001; Koopmans et al., 1998b; Lille, 2003), but few investigations have been carried out on isolated samples of the insoluble fraction or the whole shales (Barron, 1982;

Lille et al., 2003; Wilson et al., 1983). In this chapter, we analyzed structures of Ordovician Estonian Kukersite shale sample, Permian Australian Glen Davis shale sample, and Cretaceous Jordanian Ghareb shale sample by advanced ^{13}C solid-state NMR techniques including ^{13}C multiple cross-polarization magic angle spinning (multiCP/MAS), ^{13}C multiCP/MAS plus dipolar dephasing (multiCP/DD), two-dimensional ^{1}H-^{13}C heteronuclear correlation (2D HETCOR), and 2D HETCOR with ^{1}H spin diffusion. Our objectives were to obtain quantitative structural information on these three shales and to compare the structures present in their kerogens, which have very different heteroatom compositions, in order to understand how they contribute to organic matter structural properties.

MATERIALS AND METHODS

Shale samples

Ordovician kukersite deposits of Estonia cover an area of more than 50,000 km^2, and they have been extensively exploited and processed to fuel electric power plants and produce synthetic crude oil, petro-chemicals and other products (Dyni, 2003). The Kukersite shale sample is a type I/II kerogen-bearing oil shale from the Narva-E mine, Estonia. Permian Glen Davis torbanite/shale deposits at New South Wales Australia are organic-rich sedimentary rocks primarily originating from Botryococcus *braunii* algae (Derenne et al., 1988; Hutton et al., 1980) and some methanogenic bacteria (Glikson, 1983). The Cretaceous Jordanian Ghareb marinite contains Type IIS kerogen and is rich in a complex distribution of organic sulfur compounds, among which the alkylthiophenes can be used as biomarkers to indicate paleoenvironmental changes (Kohnen et al., 1990; Koopmans et al., 1998a). All the shale samples were provided by the USGS (collected by M. Lewan). The shale samples were crushed, pulverized, and sieved (-60 mesh) to obtain homogenized powders for NMR analysis.

The mineralogy of shale samples was determined by X-ray diffraction (XRD; see Table 3). Corundum was added as an internal standard (20 wt. %) to each sample prior to micronization and a PANalytical X'Pert Pro MPD X-ray diffractometer (Westborough, Massachusetts) was used to collect diffractograms. Semi-quantitative mineralogy was obtained by interpreting diffractograms using the Jade Software package (Materials Data Inc., Livermore, California). Elemental compositions of isolated kerogen samples were determined following demineralization following the method described previously (Bolin et al., 2016). Total organic carbon (TOC) content and programmed pyrolysis parameters were determined using a LECO C744 Series analyzer and Wildcat Technologies Hydrocarbon Analyzer With Kinetics (HAWK), respectively, following manufacturers' instructions. The results from kerogen elemental analysis and XRD, TOC, and programmed pyrolysis analyses on shale samples are shown in Table 1.

NMR spectroscopy

All ^{13}C NMR analyses were performed on a Bruker Avance 400 spectrometer at 100 MHz for ^{13}C. Samples were packed in 4-mm-diameter zirconia rotors with Kel-F caps, and experiments were run in a double-resonance probe head. The ^{13}C chemical shifts were referenced to tetramethylsilane (TMS), with $^{13}COO^-$ labeled glycine at 176.49 ppm as a secondary reference.

^{13}C multiple cross-polarization magic angle spinning (multiCP/MAS) NMR

The ^{13}C multiCP/MAS technique was employed to obtain quantitative solid-state ^{13}C MAS NMR spectra with good signal-to-noise ratios while measuring time was significantly reduced in contrast to direct-polarization (DP/MAS) NMR (Johnson and Schmidt-Rohr, 2014). The spectra were collected at a spinning speed of 14 kHz, with very small (<3%) spinning sidebands that have minimal overlap with centerbands. The 90° ^{13}C pulse length was 4.2 μs. Scan numbers ranged from 1024 to 4096 based on the carbon contents in the samples to achieve reasonable S/N ratio.

Table 3. Summary of results from total organic carbon (TOC), programmed pyrolysis and X-ray Diffraction (XRD) analyses of shales and elemental analysis of corresponding kerogen isolates.

Shale	TOC (mg/g)	S1 (mg/g)	S2 (mg/g)	S3 (mg/g)	Tmax (°C)
Kukersite	447	0.4	439.2	5.6	428
Glen Davis	562	3.7	521.5	3.0	457
Ghareb	209	5.1	158.4	2.9	407

Shale	Quartz (wt. %)	Calcite (wt. %)	Total Clay (wt. %)	Feldspar (wt. %)	Amorphous (wt. %)
Kukersite	8.1	37.9	4.5	N/A	30.6
Glen Davis	48.4	1.0	1.7	N/A	49.8
Ghareb	8.9	67.2	11.0	12.2	6.1

Kerogen	Carbon (wt.%)	Hydrogen (wt.%)	Nitrogen (wt.%)	Oxygen (wt.%)	Total Sulfur (wt.%)
Kukersite	74.43	8.72	0.22	13.41	1.51
Glen Davis	84.87	9.07	1.22	3.71	0.80
Ghareb	68.75	7.71	1.57	5.66	14.13

Note: Mineralogy is reported on an organic-free basis. Other minor mineral phases detected include pyrite (Kukersite, 0.8 and Ghareb 0.7 wt. %), dolomite (Kukersite, 5.9 wt. %), and fluorapatite (Ghareb, 5.9 wt %).

^{13}C multiCP/MAS plus dipolar dephasing (multiCP/DD)

To obtain quantitative structural information on non-protonated carbons and mobile segments, ^{13}C multiCP/MAS combined with dipolar dephasing was applied. Most experimental conditions were the same as for the ^{13}C multiCP/MAS method except that a recoupled dipolar

dephasing time of 68 μs was applied (Mao and Schmidt-Rohr, 2004a). The same scan numbers were collected as in the multiCP/MAS technique.

Two-dimensional ^{1}H-^{13}C heteronuclear correlation (2D HETCOR) NMR

The 2D HETCOR and its combination with dipolar dephasing can identify specific functional groups and their connectivities and proximity (Mao et al., 2017a; Mao et al., 2001). 2D HETCOR experiments were performed at a spinning speed of 7.5 kHz. Standard Hartmann-Hahn CP (HH-CP) with 0.5 ms CP time allows for correlations between carbons and protons within ~0.5 nm radius. A 40-μs dipolar dephasing delay was inserted into the HH-CP HETCOR pulse sequence to reveal multi-bond proximities between protons and non-protonated carbons or mobile groups like -CH_3. 2D HETCOR NMR with ^{1}H spin diffusion (Mao and Cao, 2011) was also performed with a 1 ms mixing time.

Structural model construction and spectrum simulation

A structural model of Kukersite kerogen was constructed based on the model proposed by Lille et al. (Lille et al., 2003). The model was adapted by calculating 1D ^{13}C NMR spectra, for all C, C not bonded to H, and CH, using chemical shifts from the empirical chemical-shift prediction program from ACD/Labs (Anderson et al., 2014; Lille et al., 2003). These data were input to an in-house Matlab program that converted them into spectra with a Gaussian line broadening of ca. 5 ppm (full width at half maximum). The structures were optimized iteratively by small modifications until the necessary fit of simulated spectra with the experimental spectra was obtained.

RESULTS

^{13}C multiCP/MAS and ^{13}C multiCP/DD spectra

Quantitative multiCP/MAS ^{13}C NMR spectra of all carbons and those of non-protonated carbons and mobile segments in the three shale samples are presented in Figure 11. All the three multiCP/MAS ^{13}C NMR spectra contained sharp peaks centered at 30 ppm, which were assigned to polymethylene chains, and all three had relatively weaker signals in aromatic regions (93-165 ppm). The region of 0-48 ppm was assigned to nonpolar alkyls, 48-65 ppm to OCH_3 and NCH, 65-93 ppm to O-alkyls, 93-148 ppm to aromatics, 148-165 ppm to aromatic C-O, 165-190 ppm to COO and NC=O, and 190-220 ppm to ketones and aldehydes. With the assistance of spectral editing techniques including dipolar dephasing, more specific assignments can be achieved (Mao et al., 2017a). In the multiCP/MAS ^{13}C NMR spectra (Figure 11 a, c, and e), all three contained aliphatic bands centered at 30 ppm and aromatic bands around 93-165 ppm. After dipolar dephasing (Figure 11 b, d, and f), the intensities of the aromatic bands were only slightly changed, indicating that most aromatic carbons are not bonded to hydrogens. The residual signals within sp^3-hybridized carbon region are from rotating $-CH_3$ groups around 0-24 ppm and mobile $-(CH_2)_n-$ segments around 30 ppm.

In the ^{13}C multiCP/MAS spectrum of Kukersite sample (Figure 11 a), there were signals in the aromatic region around 156 ppm, 142 ppm, and 117 ppm, and much stronger signals in the aliphatic region around 30 ppm and 15 ppm, indicating most carbons were in aliphatic forms. The aromatic signals of Kukersite sample were more distinctive than those of Glen Davis sample and Ghareb sample, indicating extensive oxygen substitution of the aromatic rings. In the dipolar dephased spectrum of Kukersite sample (Figure 11 b), the aromatic signals were slightly reduced meaning most of the aromatic carbons were non-protonated, while the signals at 30 ppm was significantly reduced. The peak centered around 156 ppm was assigned to aromatic carbons bonded to oxygen, and the band at 115 ppm to their neighboring carbons, while the band centered

around 142 ppm was assigned to substituted aromatic carbons not near oxygen, or orthodiphenols (Figure 11 a and b). The broad band around 75 ppm was due to OCH or OCH_2 groups. The prominent band at 30 ppm was attributed to $-(CH_2)_n-$, and the small peak around 15 ppm to $-CH_3$.

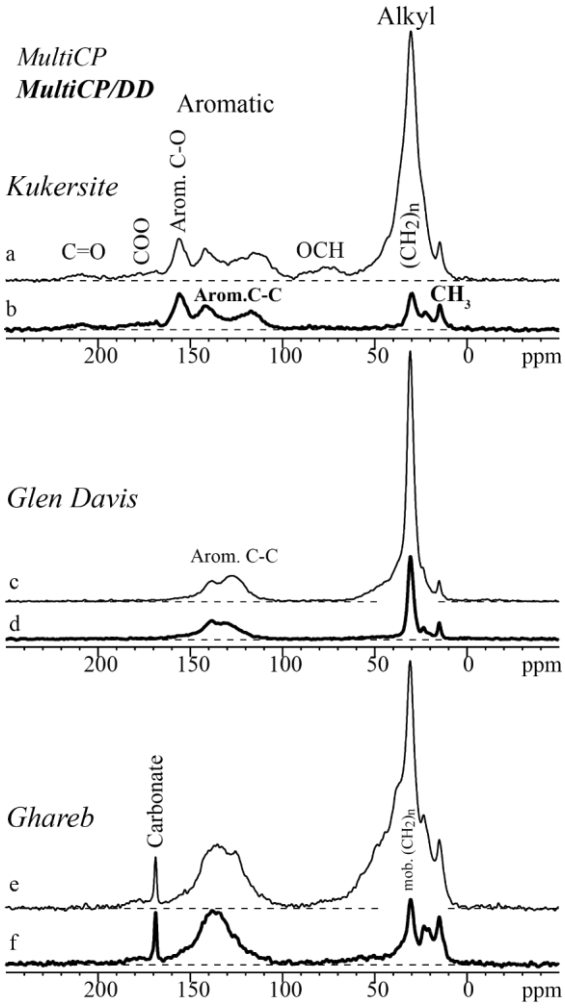

Figure 11. Quantitative multiCP ^{13}C NMR spectra of all carbons (a, c, and e) and multiCP with dipolar dephasing of non-protonated carbons and mobile carbons (b, d, and f) from Kukersite, Glen Davis, and Ghareb shale samples.

The ^{13}C multiCP/MAS spectrum of Glen Davis sample (Figure 11 c) was relatively simpler compared with that of Kukersite sample, containing two major bands: aromatic band around 130 ppm and a sharp aliphatic peak around 30 ppm. The aliphatic band was the sharpest and strongest among the spectra of the three shales, indicating it had the most abundant aliphatic structure. The aromatic peak of Glen Davis sample was the smallest among the three samples. The aromatic signals around 138 ppm were assigned to branched non-protonated aromatic carbons because they were retained in the ^{13}C multiCP/DD spectrum. The signals around 127 ppm were partially retained in the ^{13}C multiCP/DD spectrum indicating that a part of the signals was due to protonated aromatic carbons (Figure 11 c and d). Almost no signals of aromatic or alkyl C-O functional groups were present. The sharp band at 30 ppm was assigned to -$(CH_2)_n$-, and the small peak at 15 ppm assigned to –CH_3.

In the ^{13}C multiCP/MAS and multiCP/DD spectra of Jordanian Ghareb shale (Figure 11 e and f), there was a sharp peak at 169 ppm, assigned to carbonates, in addition to the two bands assigned to aliphatics and aromatics, which was different from the spectra of the other two samples. The carbonate peak corresponded to the large amount of calcite (67.2 wt.%) in the mineral fraction; however, this peak was not observed in the Kukersite spectrum, which also contained a substantial calcite fraction (37.9 wt. %). The aromatic band was centered at 135 ppm and mostly arose from non-protonated aromatic carbons, and the shoulder at ~125 ppm was primarily assigned to protonated aromatic carbons. Again, there were almost no C-O signals. The band at 30 ppm was assigned to mobile -$(CH_2)_n$-, and the small peak at 15 ppm to –CH_3. The alkyl band was broader compared to those of the other two shales, indicating more diverse aliphatic carbons, presumably in branched and cyclic alkane structures.

Quantitative structural information and aromaticity

The quantitative structural information of the three samples is listed in Table 4, where the percentages of different functional groups of the organic matter in the shales were calculated based on ^{13}C multiCP/MAS and ^{13}C multiCP/DD spectra (Johnson and Schmidt-Rohr, 2014; Mao et al., 2017a). Alkyl C accounted for more than half of the organic carbons in all three shales, among which Glen Davis sample had the largest proportion (70.5%), consistent with the intense alkyl peaks in Figure 11 c. Previous studies on oil shales showed no anomeric carbons present (Cao et al., 2013a), indicating carbohydrates were absent, so the ^{13}C chemical shift anisotropy filter technique was not applied in the present study. The aromatic C fraction, including aromatic C-O, ranged from 23.8% for the Glen Davis sample to 28.5% in the Ghareb sample. The organic matter of Kukersite sample had the largest percentage of aromatic C-O (about 7.3%) while organic matter of Ghareb sample had the largest proportion of aromatic C (about 25.5%). About 71-75% of the aromatic C in the three samples was non-protonated (arom. C-O and arom. C-C), indicating there was much more substituted or bridgehead aromatic C than aromatic C-H. The ketone/aldehyde fraction was small (2%) in the Kukersite sample, and negligible in the other two samples. The COO and NC=O groups accounted for a little more, being the most abundant in Ghareb sample at 3.3%, with the carbonate peak at 169 ppm in Figure 11 e. All three samples had some amounts of OCH_3 and NCH moieties, with the highest in Ghareb sample (up to 8.5% of the organic carbon), more than twice the fraction present in Kukersite and Glen Davis samples, to some extent accounting for the broad base of the aliphatic band in Figure 11 e. The O-alkyl fraction ranged from 0.7% in Glen Davis organic matter to 4.8% in Kukersite.

Figure 12 illustrated the functional group distribution in the organic matter of the three shale samples more clearly. The alkyl groups dominated in all three samples and followed by

aromatic groups. The aromatic-O group in from Kukersite shale is obviously greater than the other two, which is consistence with spectral features in Figure 11.

The aromaticity of the three sample and the percentages of aromatic C-O, C-C, and C-H were calculated after sideband correction (Mao and Schmidt-Rohr, 2004a) and show in Table 5. The aromaticity of three samples ranged around 26%-31%, with Ghareb sample showed the highest aromaticity and Glen Davis sample the lowest. All three samples had about 25%-29% of aromaticity as protonated aromatic carbons. Among the non-protonated carbons, Kukersite sample had the most aromatic carbons in the form of aromatic C-O, much higher than the other two samples, and the least in the form of aromatic C-C.

Table 4. Relative proportions (%) of functional groups in the three oil shales determined by ^{13}C multiCP/MAS and ^{13}C multiCP/DD spectra.

Chemical Shift	Ketone and aldehyde	COO and NC=O	Arom.O	Arom.C	OCH and OCH_2	OCH_3	N**C**H	Other alkyls	C**C**H_3
(ppm)	220-190	190-165	165-148	148-93	93-63	63-48		48-0	
Kukersite	2.0	2.6	7.8	20.4	4.7	0.7	2.8	53.4	5.6
Glen Davis	0.2	0.7	2.0	23.5	0.7	1.1	2.9	63.8	5.1
Ghareb	0.4	3.2	3.2	27.2	2.9	1.9	6.3	44.9	9.9

2D ^{1}H-^{13}C HETCOR NMR spectra

Kukersite sample

Spectra from 2D ^{1}H-^{13}C HETCOR and 2D HETCOR with dipolar dephasing experiments on the Kukersite sample are shown in Figure 13. A 2D HETCOR NMR spectrum with 0.5 ms cross polarization time can reveal ^{1}H-^{13}C proximities within one or two bonds (Mao et al., 2001), i.e., ^{1}H signals within approximately 0.5 nm radius from the C are detected. ^{1}H slices were extracted from the 2D spectra to identify the proximities between functional groups. The ^{1}H slices extracted from the ^{13}C chemical shifts of 15 ppm and 30 ppm (Figure 13 c) had cross peaks in the aliphatic region indicating the alkyl carbons mainly associated with their directly bonded alkyl protons around 1.5 ppm. The ^{1}H slices at the ^{13}C chemical shift of 75 ppm had a proton peak at 1 ppm and a shoulder around the ^{1}H chemical shift of 6.5 ppm, suggesting that the O-alkyl carbons were primarily correlated with the alkyl chain and also with aromatic rings. The ^{1}H slices from the aromatic carbon region at 112 ppm, 141 ppm, and 155 ppm showed signals of directly bonded protons around 6.5 ppm as well as alkyl proton signals at around 1.5 ppm, demonstrating that aromatic carbons were bonded to alkyl groups.

Table 5. Aromaticity and the percentages of aromatic C-O, C-C, and C-H in three samples calculated from ^{13}C multiCP/MAS and ^{13}C multiCP/DD spectra.

	Aromaticity (%)	Arom. C-O (%)	Arom. C-C (%)	Arom. C-H (%)
Kukersite	28.2	28.4	42.4	29.2
Glen Davis	25.5	13.9	59.7	26.4
Ghareb	30.4	15.8	59.2	25.0

The 2D HETCOR spectrum with dipolar dephasing in Figure 13 b shows the correlations of non-protonated carbons with protons that are at least two bonds away, and ^{1}H slices were extracted and shown in Figure 13 d. ^{1}H slices extracted at the ^{13}C chemical shifts of 15 ppm, 23 ppm, and 30 ppm showed alkyl proton signals. The ^{1}H slices at ^{13}C chemical shifts of 116 ppm, 141 ppm, and 155 ppm (Figure 13 d) had shoulders around 6.5 ppm and major bands around 1.5 ppm, demonstrating the non-protonated aromatic carbons were close to aromatic protons and nonpolar alkyl protons, which confirmed the linkage between aromatic and alkyl functional groups.

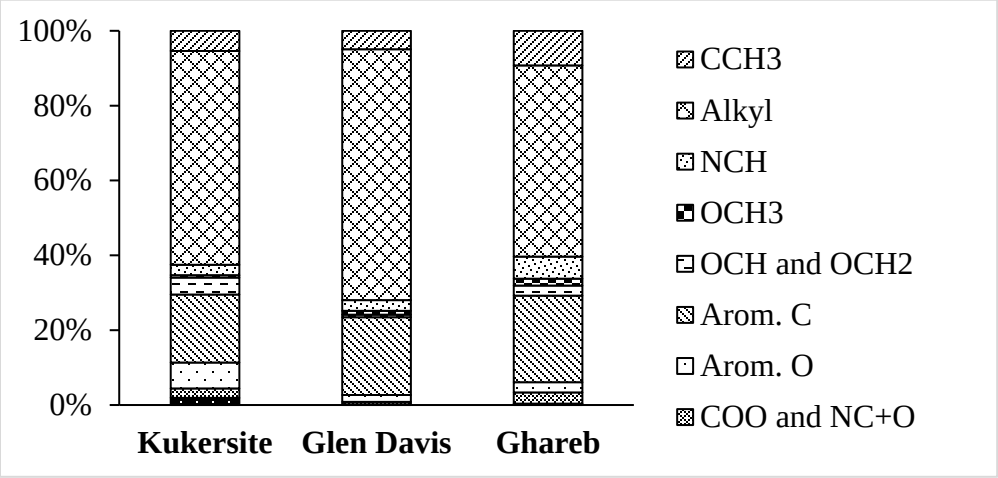

Figure 12. Functional group distribution in the organic matter of Kukersite, Glen Davis, and Jordanian Ghareb shale samples.

Glen Davis sample

Figure 14 shows the 2D HETCOR spectra of Glen Davis sample. Similar to Kukersite sample, the ^{1}H slices (Figure 14 c) extracted at the ^{13}C chemical shifts of 15 ppm and 30 ppm showed predominantly cross peaks to the directly bonded protons around 1.5 ppm. The ^{1}H slices from 126 ppm and 138 ppm showed that aromatic carbons were near both their bonded protons

(signals around 7.5 ppm), and alkyl groups (signals around 1.5 ppm). The 2D HETCOR spectrum with dipolar dephasing of Glen Davis sample is presented in Figure 14 b. The extracted ^{1}H slices (Figure 14 d) at the ^{13}C chemical shifts of 15 ppm, 23 ppm, and 30 ppm confirmed the association between alkyl carbons and their bonded protons, while the ^{1}H slices taken at 131 ppm and 138 ppm demonstrated again that the non-protonated aromatic carbons were substituted with alkyl groups.

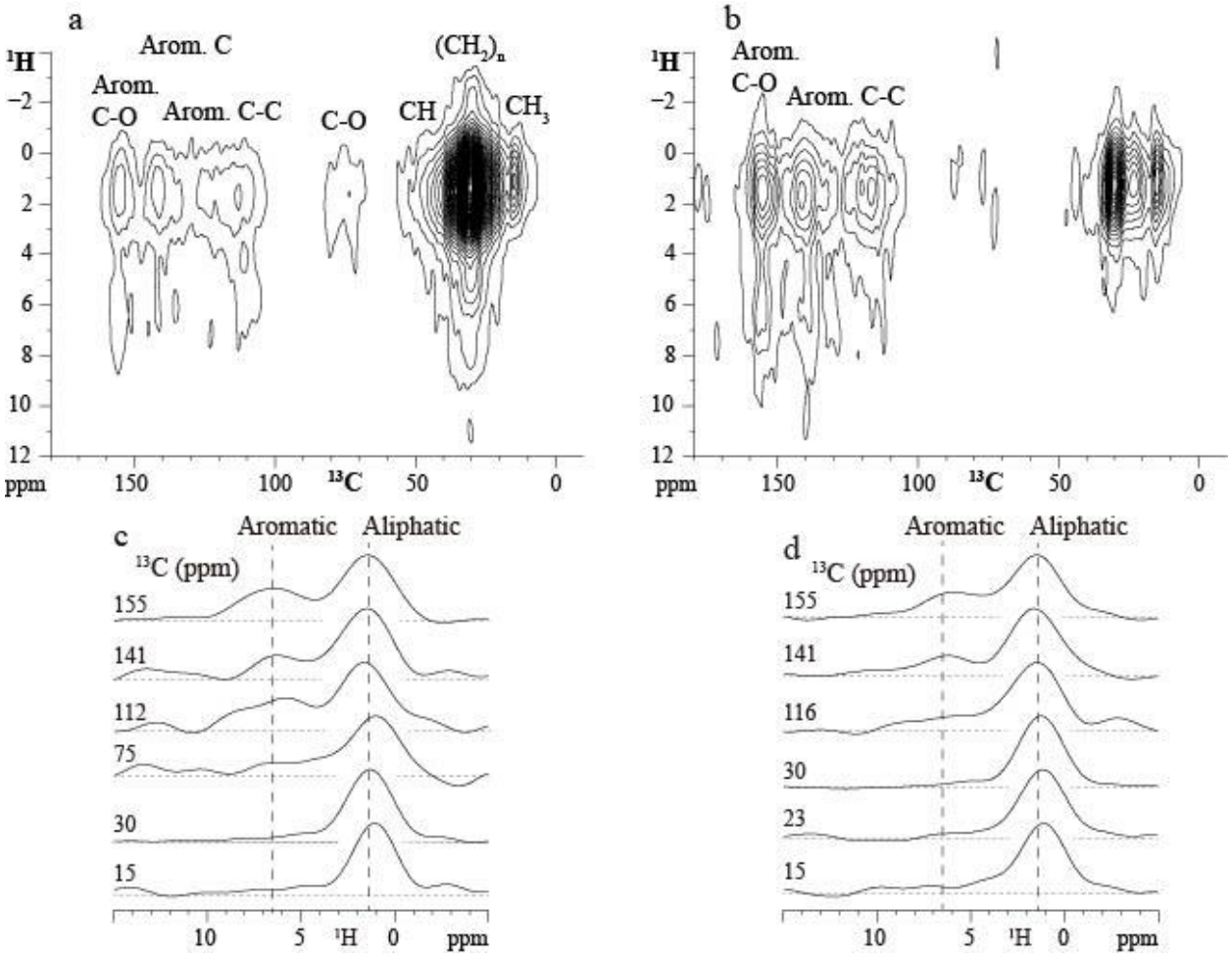

Figure 13. (a) 2D ^{1}H-^{13}C HETCOR NMR spectrum and (b) 2D ^{1}H-^{13}C HETCOR spectrum after dipolar dephasing of Kukersite sample. (c, d) ^{1}H slices extracted from the 2D spectra; (c) refers to ^{1}H slices from spectrum (a), and (d) from spectrum (b).

A 2D HETCOR spectrum with 1 ms ^{1}H spin diffusion spectrum of Glen Davis sample is shown in Figure 15 a. Fast equilibration within 1 ms corresponds to heterogeneities of less than 1 nm (Mao and Cao, 2011; Mao et al., 2010). The ^{1}H slices (Figure 15 b) extracted at ^{13}C chemical shifts of 15 ppm, 30 ppm, 126 ppm, and 138 ppm were all similar, indicating that magnetization was equilibrated within 1 ms. The fast equilibration indicated that aromatic carbons in this shale do not form domains and are in close proximity to the alkyl chains.

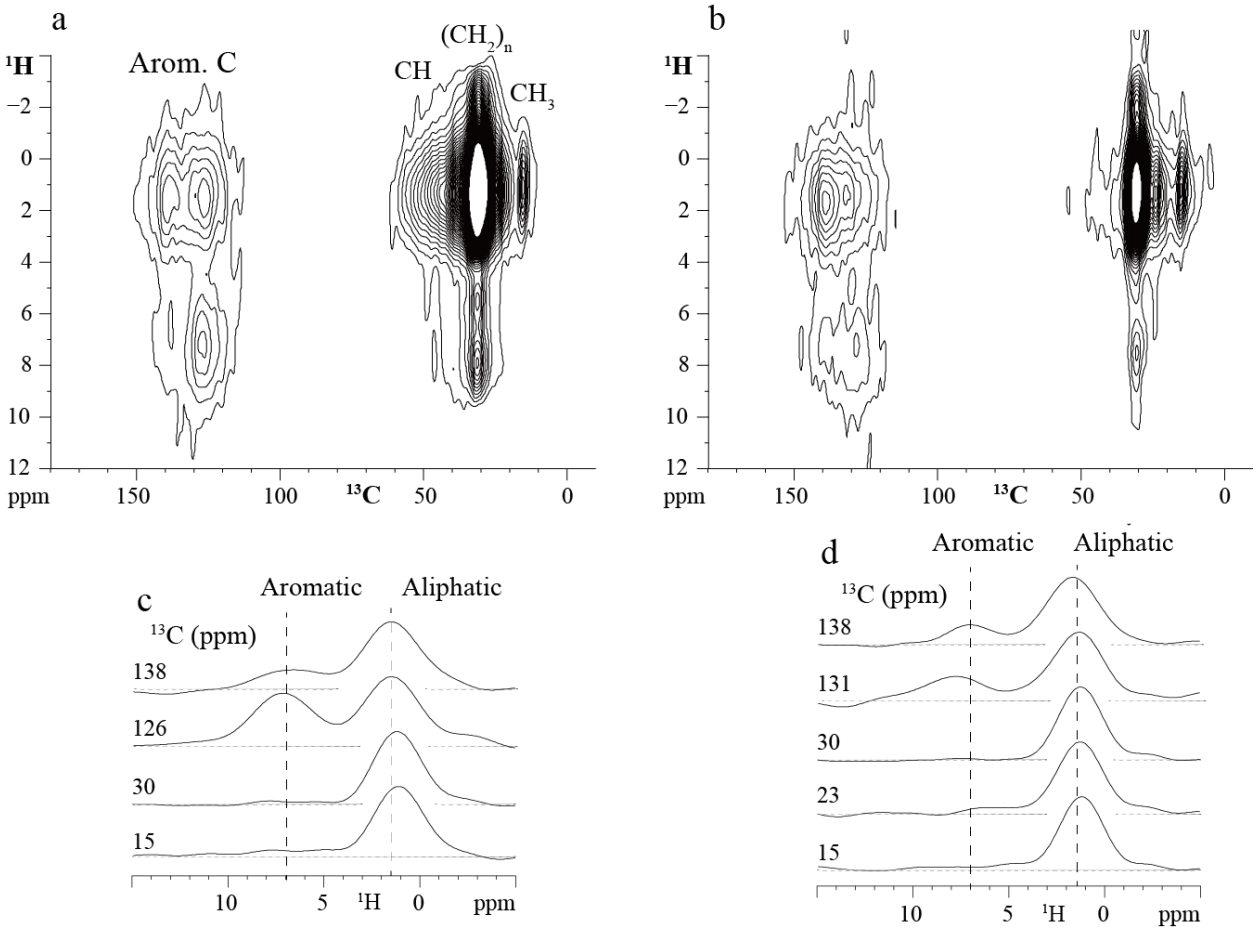

Figure 14. (a) 2D ^{1}H-^{13}C HETCOR NMR spectrum and (b) 2D ^{1}H-^{13}C HETCOR spectrum after dipolar dephasing of Glen Davis sample. (c, d) ^{1}H slices extracted from the 2D spectra; (c) refers to ^{1}H slices from spectrum (a), and (d) from spectrum (b).

DISCUSSION

The Estonian Kukersite shale sample is derived from the accumulation of the remains of an extinct microorganism, Gloeocapsomorpha *Prisca* (Derenne et al., 1990; Dyni, 2003; Lille, 2003). The bitumens generated by the pyrolysis of Kukersite kerogen and most Ordovician oils show distinctive features of saturated hydrocarbon distribution (Derenne et al., 1990). Some key features of Kukersite kerogen include a dominance of C_9-C_{19} odd n-alkane chains and a prominent occurrence of phenolic structures (Lille, 2003), which is consistent with the n-alkyl-phenol and n-alkyl-resorcinol structures of the pyrolysates of its origin, the outer cell walls of G. *Prisca* (Blokker et al., 2001; Derenne et al., 1990).

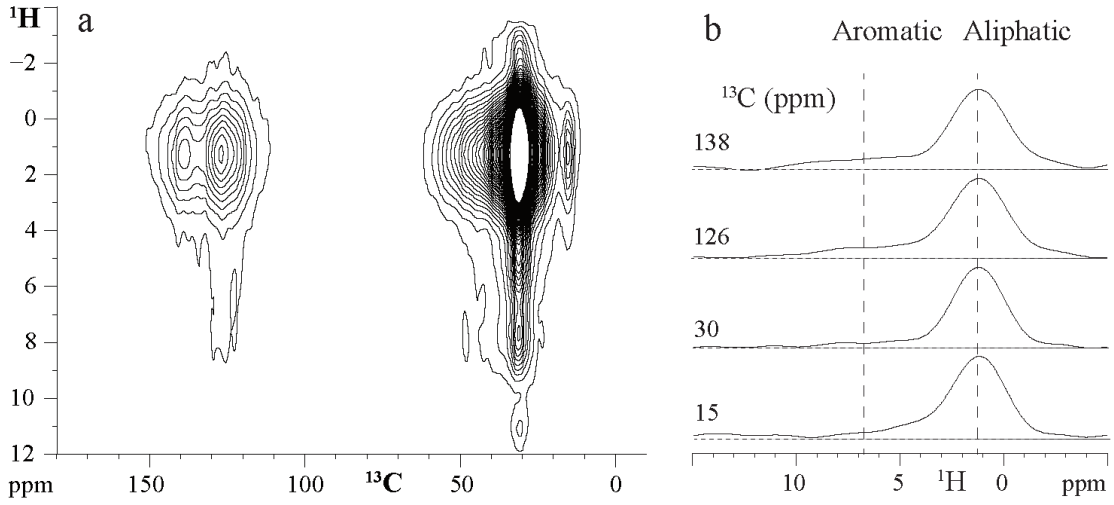

Figure 15. (a) 2D ^{1}H-^{13}C HETCOR NMR spectrum with 1 ms ^{1}H spin diffusion and (b) ^{1}H slices extracted from the 2D spectrum of Glen Davis sample.

The Kukersite shale sample in our study (Table 3) has a similar kerogen elemental composition to the kerogen molecular model proposed by Lille et al.(Lille et al., 2003). The long aliphatic carbon chains in the model correspond to the large alkyl band around 5 to 50 ppm in the experimental and simulated ^{13}C MAS NMR spectra of the Kukersite kerogen (Lille et al., 2003), consistent with our ^{13}C multiCP/MAS NMR spectrum of the Kukersite sample (Figure 11 a). The oxygen content of the Kukersite sample is comparatively higher than that of the other two shales (Table 3). Oxygen was proposed to be in the form of phenolic structures and ether linkages in the kerogen model (Lille et al., 2003). The heteroatom-containing groups in the model were tentatively quantified using ^{13}C CP/MAS (Lille, 2003), but with the ^{13}C multiCP/MAS and multiCP/DD NMR spectra (Figure 11 a and b), we were able to more accurately quantify the oxygen-containing functional groups (Table 4). Functional groups containing aromatic C-O bonds account for more than 1 in 4 of the aromatic carbons present, indicating the presence of many doubly O-substituted aromatic rings. The observed 155 ppm chemical shift is incompatible with ortho dioxysubstitution (~145 ppm) or para substitution (~150 ppm). The ratio of aliphatic to aromatic carbons based on the kerogen model was about 4-5 (Lille, 2003), higher than that in the present study (~2.3 calculated from Table 4). This is most likely due to the underestimation of aromatics by standard ^{13}C CP/MAS measurements. The difference between the Kukersite kerogen in the Lille et al. study and that present in our raw Kukersite oil shale is minimal based on the similar kerogen H:C ratios for the two samples. There were significantly more non-protonated (C-O and C-C, total 70.8%) than protonated aromatic carbons (29.2%; Table 5), indicating that at least 4 carbons on an aromatic ring must be substituted by oxygen or a carbon chain, on average. Kukersite kerogen contains abundant diphenolic moieties linked to the macromolecular structure via terminal and mid-chain carbon of the linear side chains (Derenne et al., 1990), which is confirmed by 2D

HETCOR data (Figure 13 a and b), and more non-protonated carbons were connected with alkyl chains (42.4%) than with phenolic groups (28.4%; Table 5) in our sample. With the lower aliphatic to aromatic carbon ratio, the structure of the Kukersite kerogen must contain shorter alkyl chains than those in the molecular model (Lille et al., 2003) to properly explain this discrepancy. We simulated an updated structural model of Kukersite kerogen based on the literature (Lille, 2003; Lille et al., 2003) by adjusting the structure, specifically shortening some alkyl chains, adding some chains on the aromatic rings, increasing the amount of methyl groups, etc., to obtain a good fit of simulated spectra with the experimental spectra. As shown in Figure 16, the simulated spectra (dashed lines) of multiCP/MAS, multiCP/DD, and CH-only corresponded well to the experimental spectra (solid lines). Specifically, the peaks within aromatic region of the simulated multiCP/MAS spectrum matched with the experimental spectrum reasonably well after the modifications, as well as the CH, CH_2, and CH_3 groups in aliphatic region and O-containing groups such as C=O, COO, and OCH.

The kerogen present in the Australian Glen Davis shale sample had a low heteroatom content (N, S, and O; Table 3), leading to a comparatively simple ^{13}C multiCP/MAS NMR spectrum (Figure 11 c) consisting mostly from signals of alkyl and aromatic carbon moieties. The absence of oxygen would be consistent with the cleavage of C-O bonds due to the maturation of the shale (Derenne et al., 1988), but by all measures the Glen Davis sample is thermally immature. Due to the small amount of aromatic C-O structures, the non-protonated carbons must be substituted with alkyl chains, consistent with the chemical shifts of aromatic carbons (Figure 11 c) and 2D HETCOR data (Figure 4 a and b). Fewer aromatic C-O structures leads to a simpler aromatic structure compared to Kukersite sample, as reflected in their different aromatic bands (Figure 11). The aliphatic band of organic matter of Glen Davis sample was sharper than those of

Kukersite or Ghareb sample (Figure 11 a and c), indicating its alkyl chains have fewer branches, cyclic structures, and cross linkages. The soluble organic matter extracted from eastern Australia Glen Davis torbanite contains large amounts of drimanes, abundant monomethylalkanes, and an unusual presence of macrocyclic alkanes containing 14 to 34 carbons (Audino et al., 2001; Audino et al., 2004; Grice et al., 2001), all consistent with a large proportion of alkyl carbons. The low aromaticity (Table 5) and the sharp aliphatic band (Figure 11 c) of our Glen Davis sample were consistent with previous results showing that the pyrolysis products of Glen Davis shale contained more saturated hydrocarbons compared to aromatic hydrocarbons (Boreham et al., 1994). The 2D HETCOR spectrum with 1 ms ^{1}H spin diffusion (Figure 15) showed no indication of previously described fused aromatic systems, such as 1,2,5-trimethylnaphthalene and 5,6-dimethyl-1-ethylnaphthalene (Grice et al., 2001). The sharp aliphatic band assigned to $–(CH_2)_n–$ and the band assigned to $–CH_3–$ can correspond to series of monomethylalkanes (Audino et al., 2001).

The Jordanian Ghareb shale sample contained much more organic sulfur in its kerogen compared to the other two samples (Table 3). Alkylthiophenes and alkylbenzothiophenes are stable forms of organic sulfur compounds (Koopmans et al., 1998b; Van Kaam-Peters et al., 1995). Both of these structures could contribute to the aromatic band centered at 135 ppm in the ^{13}C multiCP/MAS spectrum (Figure 11 e). Sulfur has a similar electronegativity as carbon, and therefore does not produce distinctive chemical shifts when bonded to carbon. This is supported by the results of sulfur XANES spectroscopy on immature kerogen from a Jordanian Ghareb sample collected at the same location as the sample examined here (Birdwell et al., 2018), revealing that the majority of sulfur moieties are categorized as thiophene, sulfoxide, sulfide, and elemental-organic sulfur. More labile sulfur moieties are converted into aromatic forms during maturation, oxygen-containing groups are eliminated, and therefore the remaining oxygens are

most likely in the form of aromatic C-O groups and O-alkyl (Kelemen et al., 2010) as shown in Table 4. The Ghareb shale had the highest aromaticity among the three shales (Table 5), consistent with more typical marine kerogens (Kelemen et al., 2007a; Miknis, 1992).

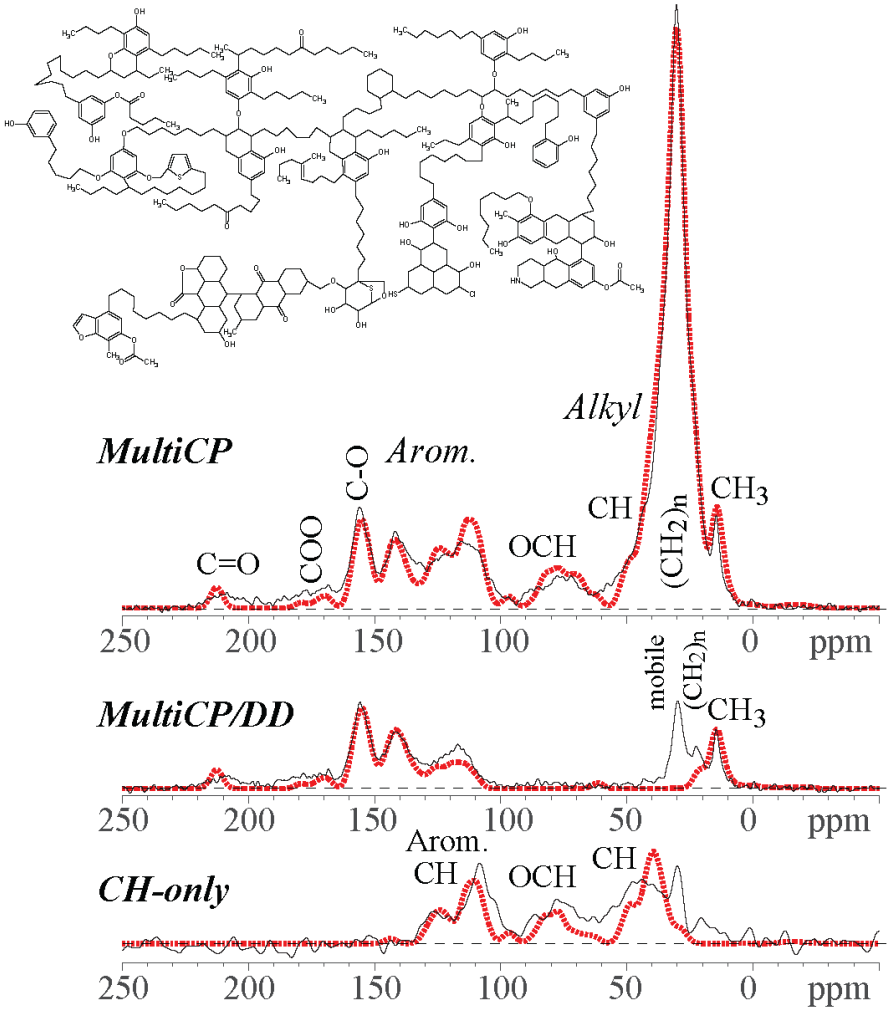

Figure 16. Structural model of Kukersite sample and its simulated (red dashed lines) and measured (black solid lines) ^{13}C NMR spectra.

CHAPTER IV

COMPARISON OF PHOSPHORIA AND KIMMERIDGE FORMATIONS

INTRODUCTION

Oil shale has been considered as one of the viable energy sources with the increasing attention to unconventional fuels, and the quality of oil produced from oil shales depends on the properties of deposits and retort technologies (Hartstein et al., 2010). Understanding the molecular composition of oil shales will assist the development of oil shale processing and the evaluation of shale oil quality. The major organic components in oil shales are kerogen, the fraction insoluble in organic solvents which represents about 80% (w/w) of the organic matter, and bitumen (native bitumen, different from bitumen generated during kerogen decomposition (Bolin et al., 2016)), the fraction soluble which accounts for about 20% (w/w) of the organic matter (Birdwell, 2017; Yen and Chilingarian, 1976).

The molecular structure of kerogen is difficult to characterize due to its insolubility, but the advances in solid-state nuclear magnetic resonance (NMR) spectroscopy techniques (Cao et al., 2013b) have improved the characterization of kerogen structural properties. Advanced solid-state NMR techniques (Cao et al., 2013b; Mao et al., 2017a) and high resolution magic angle spinning (HRMAS) NMR (Salmon et al., 2011; Simpson, 2001) have been successfully applied to study the insoluble and partially soluble fractions of natural organic matter. Bitumen represents unites of the precursors that do not bind to the insoluble macromolecular network of kerogen and that have been cleaved without much structural alteration (Speight, 2012), and it is often extracted by organic solvents and measured using analytical techniques such as gas chromatography (GC),

Fourier transform infrared (FT-IR) spectrometry (Adebiyi and Akhigbe, 2015), MS (Burdelnaya et al., 2013; Park et al., 2013), NMR spectroscopy (Borrego et al., 1996), X-ray absorption near-edge structure (XANES) spectroscopy (Birdwell et al., 2018), etc.

In this chapter, Phosphoria sample and Kimmeridge sample were selected for structural characterization using advanced solid-state NMR, HRMAS NMR, and liquid-state NMR. The Phosphoria Formation of Permian age is a world-class phosphate-ore deposit covering 350,000 km^2 area in Idaho, Wyoming, Montana, Utah, and Nevada, and has been mined for a century (Hein, 2003). The Jurassic Kimmeridge clay formation is an organic-rich claystone deposit in Britain and across north-west Europe (Scotchman, 1991). US Geological Survey (USGS) has studied the Phosphoria Formation during field mapping and sampling programs (Dyni, 2003). Pyrolysis products and bitumen extracted from the Phosphoria Formation in western United States has been investigated using GC (Claypool et al., 1978; Price and Wenger, 1992), GC-MS (Clayton and King, 1987; Lewan et al., 1986), and high performance liquid chromatography (HPLC) (Knauss et al., 1997). Phosphoria rock sample has been analyzed by two-step laser mass spectrometry (L2MS) to study the polycyclic aromatic hydrocarbons (Zhan et al., 1997). Kerogen pyrolysis products, extracts, and pulverized rock of Kimmeridge Clay Formation have been analyzed by GC-MS (Eglinton et al., 1988a; Eglinton et al., 1988b; Scotchman, 1991; van Dongen et al., 2006; van Kaam-Peters et al., 1997), gas chromatography-isotope ratio mass spectrometry (GC-IRMS), HPLC (Garrigues et al., 1990), IR spectrometry (Scotchman, 1991), cross-polarization magic angle spinning (CP/MAS) ^{13}C NMR (Boucher et al., 1990; Mann et al., 1991; Palmer et al., 1987), X-ray fluorescence (XRF) (van Dongen et al., 2006), and time-resolved synchrotron X-ray tomography (Figueroa Pilz et al., 2017). As far as we know, this is the first study on organic structural characterization of Phosphoria and Kimmeridge shales using advanced solid-state NMR,

HRMAS NMR, and liquid-state NMR. The object is to comprehensively characterize the soluble and insoluble fractions of oil shales.

MATERIALS AND METHODS

Sample preparation

Phosphoria shale is a type IIS kerogen-bearing oil shale from marine Phosphoria Formation of Permian Period in Montana, USA, and Kimmeridge clay (blackstone) is a type II kerogen-bearing oil shale from Jurassic Period in UK, both provided by USGS. The shale samples were crushed, pulverized, and sieved (-60 mesh) to obtain homogenized powder for solid-state NMR analysis.

Kerogen from Phosphoria and Kimmeridge shales were isolated by sequential of acid treatments with 18% (w/w) hydrochloric acid, 52% (w/w) hydrofluoric acid, and 37% (w/w) hydrochloric acid to remove the mineral components. This was followed by a heavy-liquid separation in $ZnBr_2$ solution, additional hot HCl to remove ralstonite, and a Soxhlet extraction using a 60:40 (wt%) benzene and methanol mixture. The residue after drying in a vacuum oven was considered kerogen (Birdwell and Washburn, 2015; Lewan et al., 1986).

Bitumen from both shales were extracted from dry, pulverized aliquots of shale using chloroform in a Soxhlet apparatus. The bitumen was then concentrated in a rotary evaporator (Birdwell and Washburn, 2015). The shales after chloroform extraction were described as extracted rocks in this study, and they were analyzed with ^{13}C solid-state NMR as well.

NMR spectroscopy

Solid-state ^{13}C NMR spectroscopy

All solid-state ^{13}C NMR analyses were performed using a Bruker Avance II 400 spectrometer at 100 MHz for ^{13}C. The shale and kerogen samples were packed in 4-mm-diameter zirconia rotors with Kel-F caps, and experiments were run in a double-resonance probe along the magic angle. The ^{13}C chemical shifts were referenced to tetramethylsilane (TMS), with $^{13}COO^-$ labeled glycine at 176.46 ppm as a secondary reference.

^{13}C multiple cross-polarization magic angle spinning (multiCP/MAS) NMR

The ^{13}C multiCP/MAS technique was developed to obtain quantitative solid-state ^{13}C MAS NMR spectra of organic materials with good signal-to-noise ratios while reducing the measuring time in contrast to direct-polarization (DP/MAS) NMR (Johnson and Schmidt-Rohr, 2014). The spectra were collected at a spinning speed of 14 kHz, with a very small (<3%) spinning sidebands and minimal overlap with center bands. The 90^0 ^{13}C pulse length was 4.2 μs.

^{13}C multiCP/MAS plus dipolar dephasing (multiCP/DD)

To identify non-protonated carbons and mobile segments, ^{13}C multiCP/MAS combined with dipolar dephasing was applied. Most conditions were the same as for the ^{13}C multiCP/MAS method but with a dipolar dephasing time of 68 μs (Mao and Schmidt-Rohr, 2004a).

^{13}C chemical shift anisotropy (CSA) filter

^{13}C CSA filter was introduced to separate signals of sp^3-hybridized carbons from those of sp^2- and sp-hybridized carbons. This technique was based on the carbon bonding symmetry, hence the fact that CSAs of sp^3-hybridized carbons are much smaller than that of sp^2- and sp-hybridized carbons, so their magnetization remains after a certain recoupling time (Mao et al., 2017b; Mao and Schmidt-Rohr, 2004b). Total suppression of sidebands (TOSS) was applied before detection, the spectra were referred as CP/TOSS/CSA filtered spectra.

^{13}C CSA filter combined with dipolar dephasing (CP/TOSS/DD/CSA filtered)

^{13}C CSA filter technique was combined with dipolar dephasing technique in order to show non-protonated mobile sp^3-hybridized carbon signals.

CH_n selection

Signals of immobile CH_2 and CH groups (CH_n) can be selected in a simple spectral editing experiment similar to the scheme previously proposed (Wu et al., 1994). Two spectra were acquired, and a third spectrum generated by their difference showed the signals of CH_n groups. The first was a CP/TOSS spectrum with a short CP of 50 µs, and the second was a CP/TOSS spectrum with a short CP of 50 µs and 40 µs dipolar dephasing (Mao et al., 2007).

Liquid-state NMR spectroscopy

Liquid-state NMR analyses were performed using a Bruker Avance III 400 spectrometer at 400 MHz for ^1H. The bitumen sample was dissolved in deuterated chloroform, and then transferred into a 5-mm NMR tube. A 1D proton spectrum was acquired with 64 scans and 1s delay. 2D spectra including ^1H-^1H correlation spectroscopy (COSY), and ^1H-^{13}C heteronuclear single quantum coherence (HSQC) were acquired to provide molecular connectivity.

High resolution magic angle spinning (HRMAS) NMR spectroscopy

HRMAS NMR experiments were performed on a Bruker Avance III 400 spectrometer at 400 MHz for ^1H. The shale sample was packed in a 4-mm-diameter 50 µl zirconia HRMAS rotor, swelled with 25 µl of deuterated dimethyl sulfoxide (DMSO-d_6), and sealed with a Kel-F insert screw and a cap. All spectra were collected in a double-resonance probe along the magic angle at

a spinning speed of 5 kHz. The HRMAS techniques including TOCSY and HSQC were adapted from liquid-state NMR.

RESULTS

^{13}C Solid-state NMR spectra

Solid state NMR is one of the most powerful techniques to investigate shale and its related solid phase samples due to their insolubility. Quantitative ^{13}C multiCP/MAS NMR spectra of all carbons and multiCP/DD spectra of non-protonated carbons and mobile carbons from Phosphoria raw shale, kerogen, and extracted rock are presented in Figure 17, and Kimmeridge raw shale, kerogen, and extracted rock in Figure 18. The region of 0-48 ppm was assigned to nonpolar alkyls, 48-63 ppm to OCH_3 and NCH, 63-93 ppm to O-alkyls, 93-147 ppm to aromatics, 147-164 ppm to aromatic C-O, 164-190 ppm to COO and NC=O, and 190-220 ppm to ketones and aldehydes.

The three multiCP/MAS spectra of Phosphoria samples (Figure 17 a, b, and c) were quite similar, dominated by a major band around 30 ppm, representing aliphatic carbons, indicating the significant contribution of methylene groups. There was also a shoulder around 15 ppm at aliphatic region, which was attributed to $–CH_3$ groups. There was a less intense signal around 132 ppm, representing aromatic carbons. There were very weak signals at OCH_3/NCH, O-alkyl, and COO/NC=O regions and almost no signals of ketone/aldehyde were present. Similarly, the multiCP/MAS spectra of Kimmeridge samples (Figure 18 a, b, and c) showed the most intense peak around 30 ppm at aliphatic region and the second most intense peak around 132 ppm at aromatic region, but the aromatic peaks were shorter than those of Phosphoria spectra.

After dipolar dephasing, the aromatic bands of Phosphoria shale and kerogen (Figure 17 d and e) and Kimmeridge shale and kerogen (Figure 18 d and e) were only slightly reduced,

indicating that the majority of the aromatic carbons were non-protonated. The residue signals at the aliphatic bands of the shales were from $–(CH_2)_n-$ groups around 30 ppm and rotating $-CH_3$ groups around 20 ppm. The signals in dipolar dephased spectra of both extracted rocks (Figure 17 f and Figure 18 f) were less intense than those of the corresponding shale and kerogen, which might be due to the low C% content in the extracted rocks resulting in poor S/N ratio.

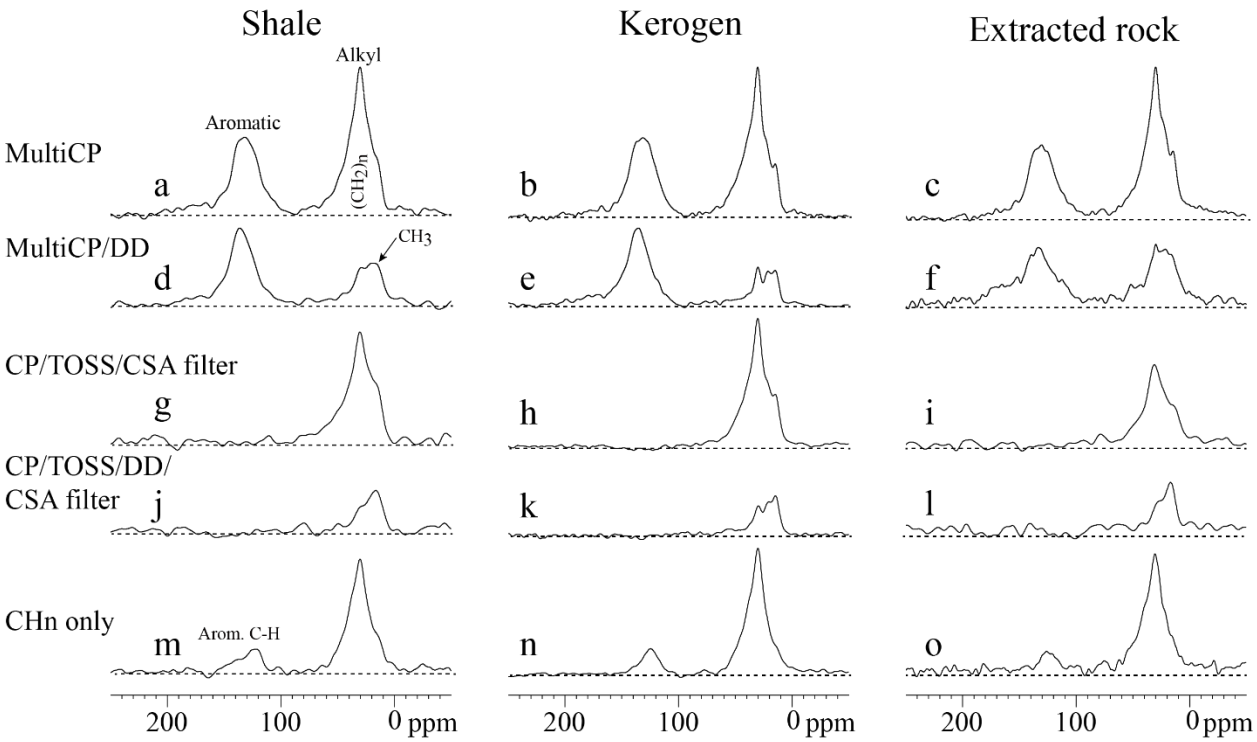

Figure 17. Quantitative multiCP ^{13}C NMR spectra (a, b, and c), multiCP with dipolar dephasing spectra (d, e, and g), CP/TOSS with ^{13}C CSA filter spectra (g, h, and i), ^{13}C CSA filter with dipolar dephasing spectra (j, k, and l), and CH_n selected spectra (m, n, and o) of Phosphoria shale, kerogen, and extracted rock samples.

Qualitative ^{13}C cross polarization with total sideband suppression (CP/TOSS) combined with spectral editing techniques were able to assign the overlapping resonances and better describe the structural characteristics of the samples. CP/TOSS/CSA filtered spectra of the three samples are presented in Figure 17, showing signals from saturated carbons. CP/TOSS/CSA filtered spectra of Phosphoria shale (Figure 17 g), kerogen (Figure 17 h), and extracted rock (Figure 17 i) samples all had aliphatic bands almost the same as those in their multiCP/MAS spectra, indicating the contribution from the alkyl carbons. No signals between 90-120 ppm were present in the CP/TOSS/CSA filtered spectra, meaning all signals in this region were attributed to aromatic carbons and no anomeric carbons, which was consistent with previous study (Cao et al., 2013a). The aliphatic bands in CP/TOSS/DD/CSA filtered spectra (Figure 17 j, k, and l) of all three samples generally matched those in multiCP/DD spectra, but there were no signals in aromatic regions since sp^2-hybridized aromatic carbon signals were suppressed. Similar results can be found in CP/TOSS/CSA filtered spectra of Kimmeridge samples (Figure 18 g, h, and i).

Signals of immobile -CH_2 and -CH groups of the Phosphoria samples are shown in Figure 17 m, n, and o. The strong signals at aliphatic region were attributed to alkyl –CH, -CH_2 groups. The much less intense signals at aromatic region were from the protonated aromatic carbons, indicating the very small amount of protonated aromatic carbons, which was consistent with the result from multiCP/DD spectra. The same trend was shown in the CH_n selected spectra of Kimmeridge samples (Figure 18 m, n, and o).

Quantitative structural information

The quantitative structural information of the six samples was listed in Table 6, where the percentages of different functional groups were calculated based on ^{13}C multiCP/MAS, ^{13}C

multiCP/DD spectra, and spectral editing results (Mao et al., 2011; Mao and Schmidt-Rohr, 2004a). Alkyl carbons accounted for a little less than half of all carbons in the Phosphoria samples and more than half in Kimmeridge samples, which was consistent with the intense aliphatic peak in the multiCP/MAS spectra (Figure 17 and 8 a, b, and c). Among the alkyl carbon, the methyl groups accounted for about 12% in Phosphoria shale and kerogen and about 9% in Kimmeridge shale and kerogen. The second major carbon moiety was aromatic carbons, accounting for 40% of total carbons in Phosphoria shale and 32% in Kimmeridge shale.

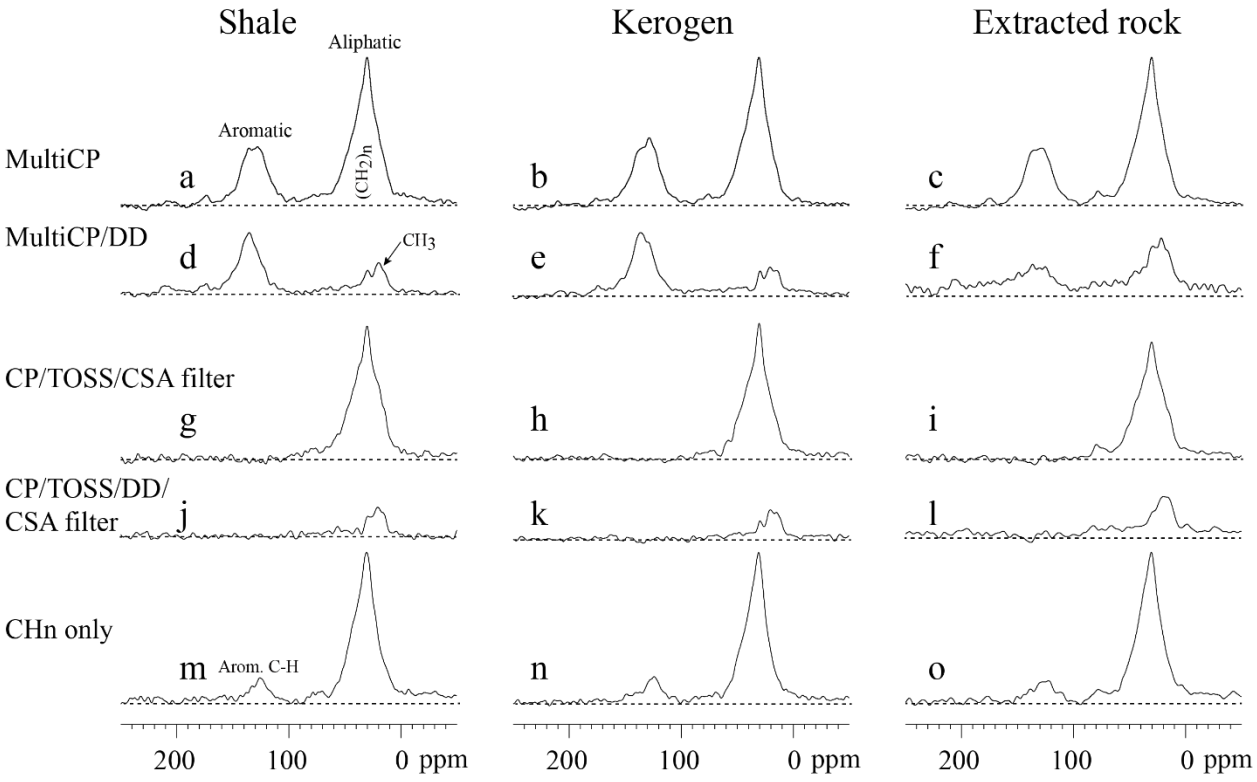

Figure 18. Quantitative multiCP ^{13}C NMR spectra (a, b, and c), multiCP with dipolar dephasing spectra (d, e, and g), CP/TOSS with ^{13}C CSA filter spectra (g, h, and i), ^{13}C CSA filter with

dipolar dephasing spectra (j, k, and l), and CH_n selected spectra (m, n, and o) of Kimmeridge shale, kerogen, and extracted rock samples.

Table 6. Relative proportions (%) of functional groups in Phosphoria and Kimmeridge shale, kerogen, and extracted rock determined by ^{13}C multiCP, ^{13}C multiCP/DD spectra, and spectral editing results.

Chemical Shift		Ketone and aldehyde	COO and NC=O	Arom.O	Arom.C	OCH and OCH_2	non-protonated OC	OCH_3	N**C**H	Other alkyls	C**C**H_3
(ppm)		220-190	190-164	164-147	147-93	93-63		63-48		48-0	
Phosphoria	Shale	1.4	3.5	3.2	36.4	1.2	1.0	1.6	3.8	35.4	12.6
	Kerogen	1.2	3.2	3.6	37.9	1.1	1.4	1.7	4.0	33.6	12.3
	Extracted rock	0.8	3.1	3.6	35.7	1.6	0.6	1.1	4.7	43.1	5.7
Kimmeridge	Shale	0.8	2.1	2.3	29.9	2.2	1.6	2.0	5.5	45.0	8.5
	Kerogen	1.0	1.9	2.9	32.0	1.5	1.7	1.8	5.2	43.1	8.9
	Extracted rock	1.1	1.4	2.2	30.0	2.4	1.7	2.3	5.1	39.8	14.0

Figure 19 was generated to visually compare the spectral features and the functional group distribution of organic matter in Phosphoria and Kimmeridge shale, kerogen, and extracted shale samples. Very close pattern appeared in the samples, especially for the predominant alkyl and aromatic groups. The illustration was consistent with the results concluded from spectral and integrating data.

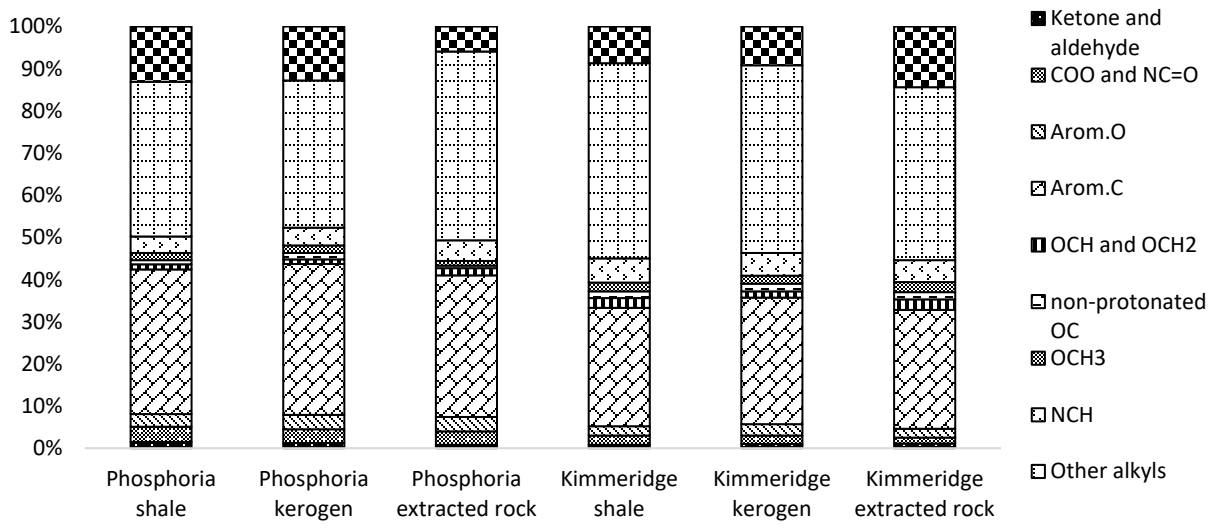

Figure 19. Functional group distribution of the organic matter in Phosphoria and Kimmeridge shale, kerogen, and extracted shale samples.

The aromaticity and the composition of aromatic C-O, C-C, and C-H were also calculated (Mao and Schmidt-Rohr, 2004a) and listed in Table 7. The aromaticity of Kimmeridge samples (32~35%) were less than that of Phosphoria samples (39~42%), which was also described by the reduced aromatic peak in their multiCP/MAS spectra (Figure 17 a and 8 a). Kimmeridge shale also had less substituted aromatic C (C-O and C-C) and more aromatic C-H than Phosphoria shale, indicating that Kimmeridge shale had fewer aromatic carbons connected to alkyl carbons and oxygens than Phosphoria shale. The chemical shift region attributed to COO and NC=O groups and NCH group accounted for 3.5% and 3.8%, respectively, in Phosphoria shale, and 2.1% and 5.5%, respectively, in Kimmeridge shale. There were small number of O-alkyl groups and little to no ketone and aldehyde groups in the samples.

Table 7. Aromaticity and the percentages of aromatic C-O, C-C, and C-H in three samples calculated from ^{13}C multiCP, ^{13}C multiCP/DD spectra, and spectral editing results.

	Sample	Aromaticity (%)	Arom. C-O (%)	Arom. C-C (%)	Arom. C-H (%)
Phosphoria	Shale	39.6	16.0	56.8	27.2
	Kerogen	41.5	22.5	70.0	7.5
	Extracted rock	39.4	5.9	17.3	76.8
Kimmeridge	Shale	32.2	18.7	52.6	28.7
	Kerogen	34.8	14.1	56.7	29.2
	Extracted rock	32.3	2.6	6.7	90.7

Note: aromaticity (%) is the proportion of aromatic C over all C, aromatic C-O (%) is the proportion of aromatic C-O over all aromatic C, aromatic C-C (%) is the proportion of aromatic C connecting to alkyl C over all aromatic C, and aromatic C-H (%) is the proportion of aromatic C-H over all aromatic C.

Liquid-state NMR spectra

Liquid-state NMR techniques were employed in order to analyze bitumen, the soluble part of shale, for better resolution during less experimental time. Figure 20 shows the ^{1}H NMR for the bitumen samples extracted form Phosphoria and Kimmeridge shales. There were generally two regions for aliphatic and aromatic protons similar to the solid-state NMR spectra. The sharp peaks at aliphatic region were assigned to methyl groups at 0.9 ppm and methylene groups at 1.3 ppm in both samples. The peak at 3.7 ppm in Phosphoria bitumen (Figure 20 b) was attributed to $–CH_2O$ groups. The big humps at the aliphatic region under the sharp peaks (Figure 20 b and e) indicated

there were other alkyl components with lower molecular mobility present. The humps between 6.2-8.3 ppm (Figure 20 c and f) were ascribed to aromatic protons, and the sharp peak at 7.28 ppm was due to the impurity of the solvent, deuterated chloroform. To better assign the proton peaks, COSY and HSQC experiments were applied to the same bitumen samples.

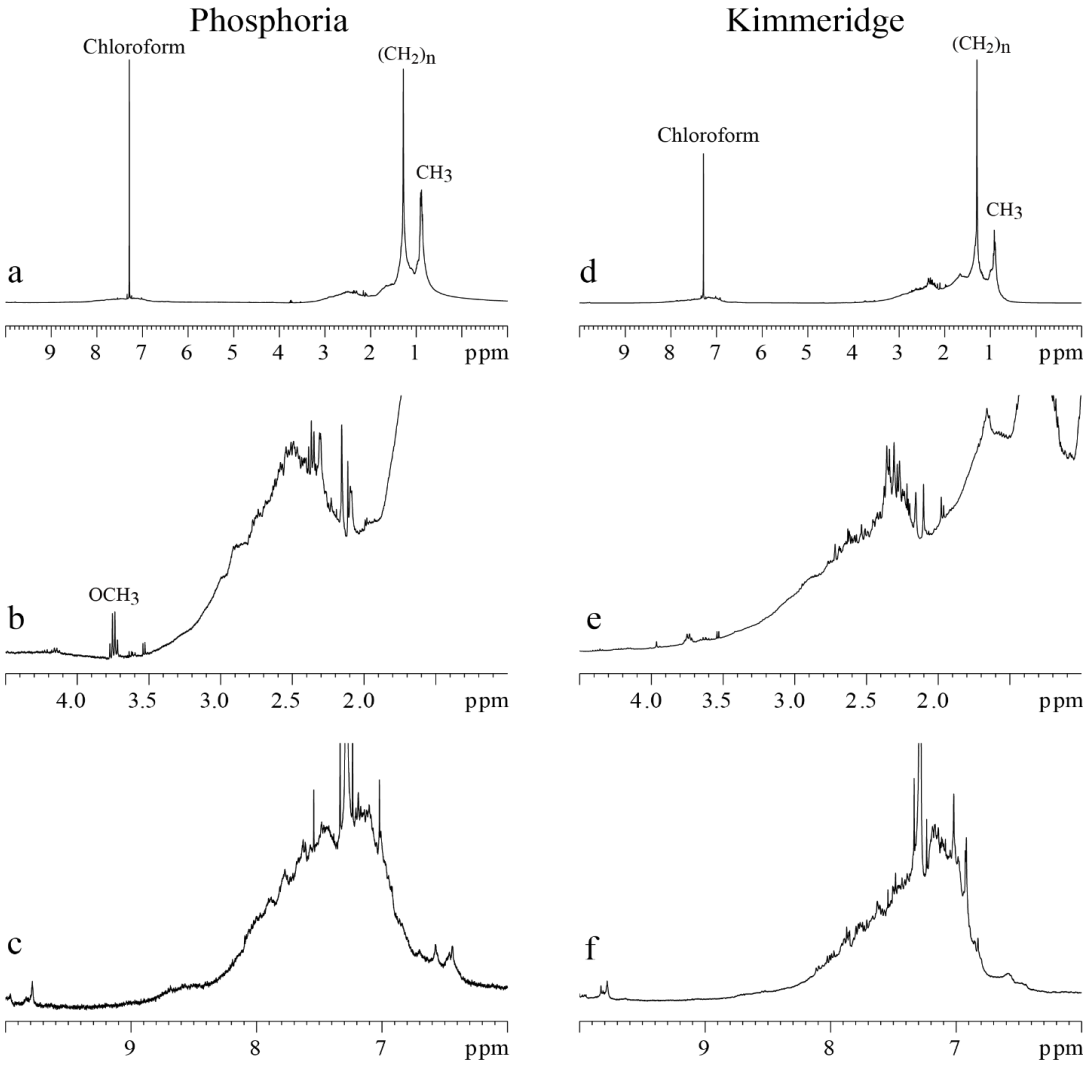

Figure 20. 1D ^{1}H NMR spectrum of Phosphoria and Kimmeridge bitumen from liquid-state NMR (a and d), 0-4.5 ppm region zoomed-in (b and e), and 6-10 ppm region zoomed-in (c and f).

The COSY spectrum of Phosphoria bitumen is shown in Figure 21. The off-diagonal contours showed the correlations between coupled protons. The correlations at aliphatic region corresponded to the intense peaks in 1D spectrum in Figure 20 a, indicating the presence of dominant aliphatic structures. Contour 1 showed the methyl groups were associated with the methylene and methine groups, confirming the presence of alkyl chains. Contour 2 was assigned to alkyl groups correlated with olefinic H, and contour 3 was assigned to methylene groups α to O-alkyls. There was no significant off-diagonal correlation at aromatic region likely due to the weak signals from the much less aromatic fraction and the fact that aromatic carbons were partially substituted. Figure 22 presents the COSY spectrum of Kimmeridge bitumen. There were more signals shown in aliphatic region than those in Phosphoria bitumen spectrum, and some signals were observed in aromatic region. Similar to Figure 21, contour 1 was assigned to methyl groups connecting to methylene groups, contour 4 to alkyl groups correlated with olefinic H, and contour 5 to methylene groups α to O-alkyls. The other signals were not in Figure 21, including contour 2 assigned to methylene groups connecting to methine groups, contour 3 assigned to methylene groups β to olefinic groups, and contour 6 was the correlation between two O-alkyls.

The 2D HSQC spectrum and two expanded regions of Phosphoria bitumen are displayed in Figure 23 to show the correlations between carbons and protons. There were two major regions of contours corresponding to aliphatic and aromatic signals. The chemical shifts of the contours in Figure 23 b and c, and the chemical structures assigned to them were listed in Table 8. For the methyl groups around 0.90 ppm at ^{1}H dimension, contour 1 and 2 were assigned to terminal methyl groups (-(CH_2)n-**CH_3**) at the end of aliphatic chains, contour 3 was assigned to branched methyl groups on aliphatic chain connected to methines (-CH(**CH_3**)-CH_2-), contour 4 was assigned to branched terminal methyl groups (-(CH_2)n-CH**$(CH_3)_2$**), and contour 5 and 6 were assigned to

methyl groups connected to cyclohexane rings. The contours along 1.2-1.3 ppm at ^{1}H dimension were assigned to different methylene groups. Contour 7 was assigned to the methylene groups α to the terminal methyl groups (-(CH_2)n-**CH_2**-CH_3), contour 9 to the methylene groups β to the terminal methyl groups (-(CH_2)n-**CH_2**-CH_2-CH_3), and 8 to the other methylene groups in a long aliphatic chain ((-**(CH_2)n**-CH_2-CH_2-CH_3). Contour 10, 11, and 12 were assigned to the methylene groups α to one or two methines of branched chains (-**CH_2**-CH-). The signals from methine groups were weaker compared to methyl and methylene groups. Contour 13 was from the methine groups connected to the terminal methyl groups (-**CH**-$(CH_3)_2$), and 14 from methine groups at branch positions of aliphatic chains (-CH_2-**CH**(CH_3)-CH_2-).

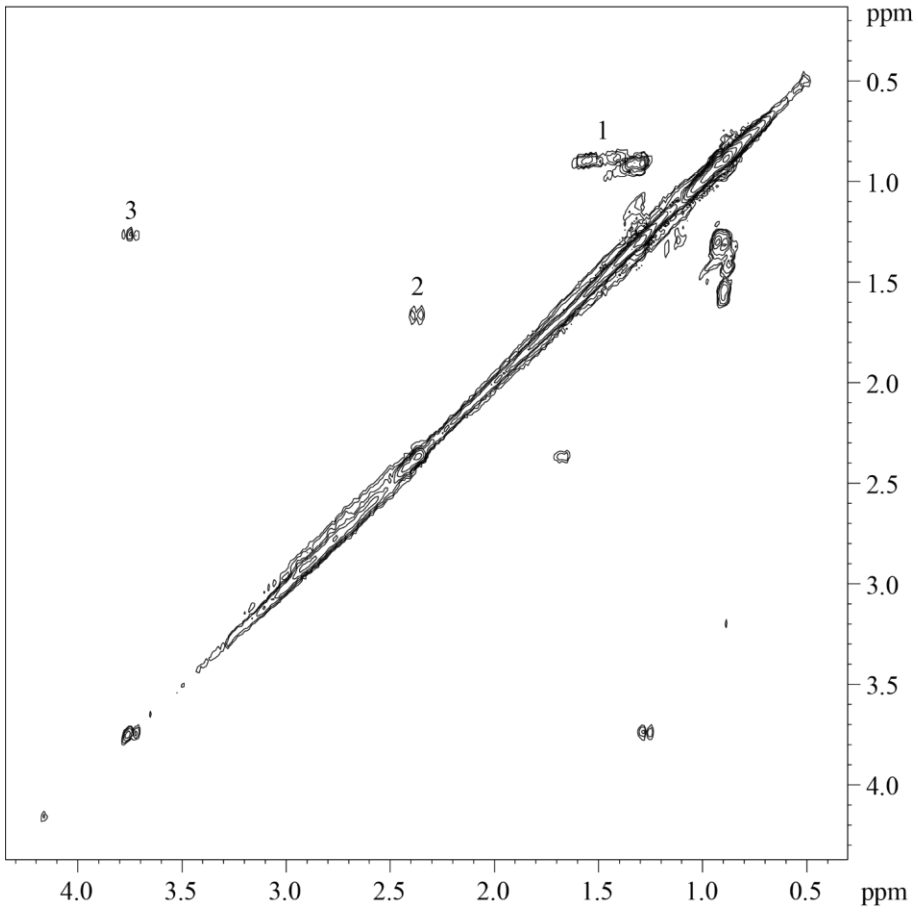

Figure 21. 2D ^{1}H-^{1}H COSY spectrum of Phosphoria bitumen from liquid-state NMR.

Other signals were attributed to alkyl groups that were close to unsaturated structures or heteroatoms. Contour #15 was assigned to methylene groups β to –COO (-**CH$_2$**-CH$_2$-COOR). Contour #16-25 were assigned methyl groups α to C=C olefinic carbons (**CH$_3$**-CH=CH-) or aromatic carbons (**CH$_3$**-Ar). Contour # 26, 27, and 28 were from the methylene group between 2 double bonds (-CH=CH**CH$_2$**CH=CH-). Contour #29 and 30 were from the methine group and methylene group connected to aromatic rings, respectively. Contour # 31 was assigned to methylene group α to COO. Contour #32 was from methylene group connected to aromatic C-O (-**CH$_2$**-O-Ar). The rest of the contours #34-43 were from aromatic groups.

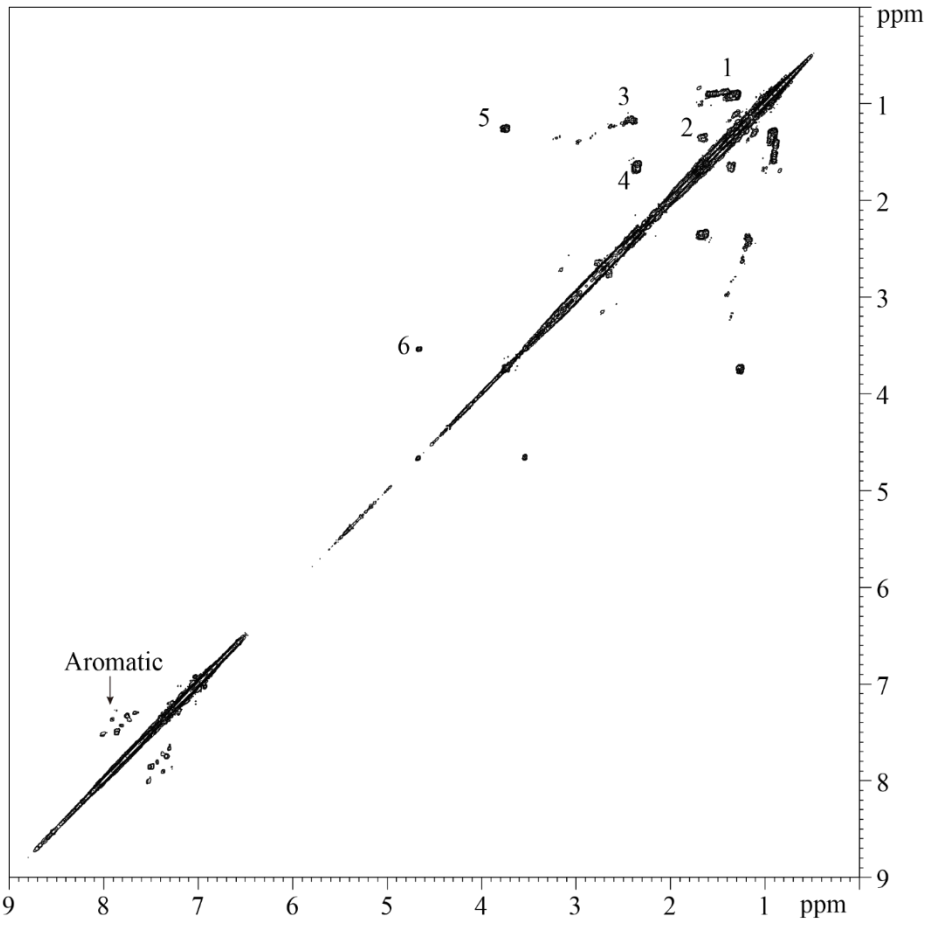

Figure 22. 2D ^{1}H-^{1}H COSY spectrum of Kimmeridge bitumen from liquid-state NMR.

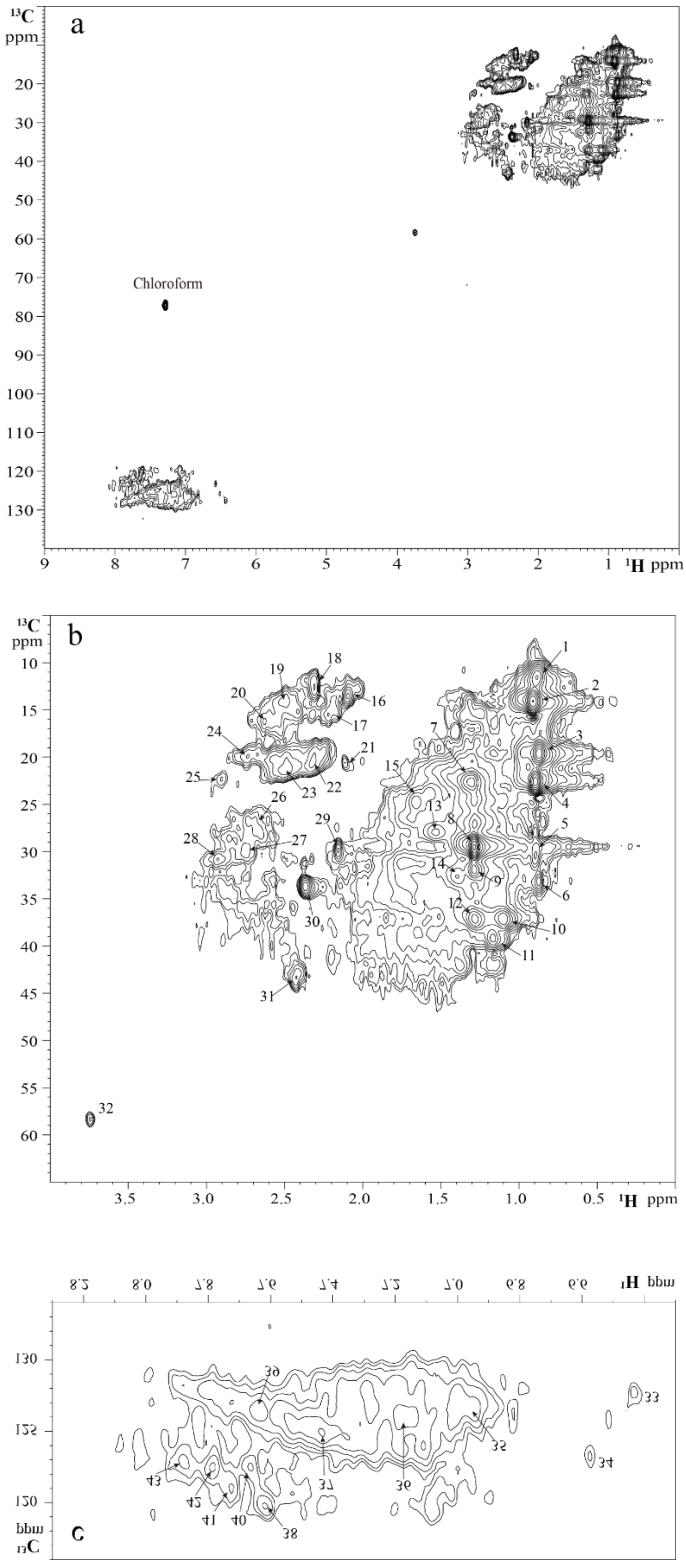

Figure 23. 2D ^{1}H-^{13}C HSQC spectrum of Phosphoria bitumen from liquid-state NMR (a), aliphatic region (b), and aromatic region (c).

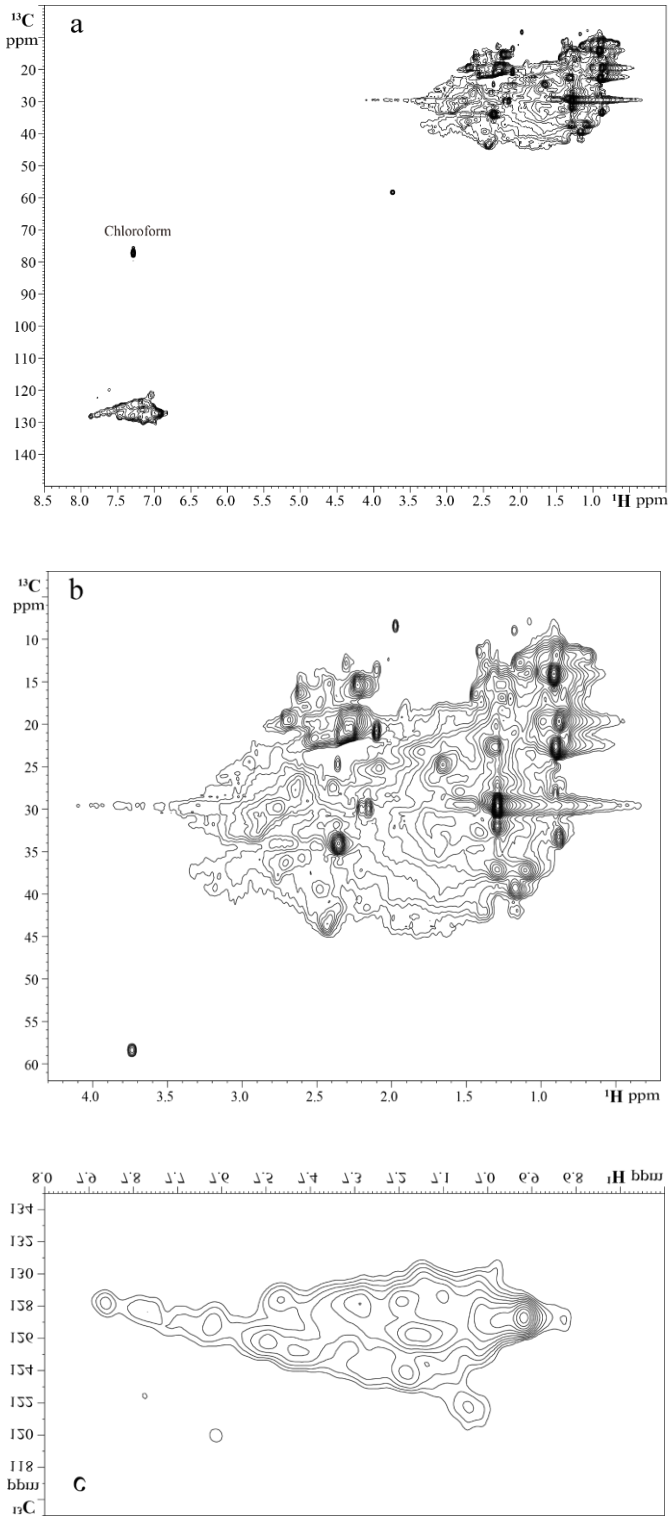

Figure 24. 2D ^{1}H-^{13}C HSQC spectrum of Kimmeridge bitumen from liquid-state NMR (a), aliphatic region (b), and aromatic region (c).

Table 8. Contours selected from 2D ^{1}H-^{13}C HSQC spectrum of Phosphoria bitumen sample from liquid-state NMR and the possible chemical structure assignments.

Contour #	^{1}H shift (ppm)	^{13}C shift (ppm)	Chemical structure	Contour #	^{1}H shift (ppm)	^{13}C shift (ppm)	Chemical structure
1	0.9	12	-$(CH_2)_n$-**CH_3**	23	2.5	21	**CH_3**-Ar or **CH_3**-CH=CH-
2	0.9	14	-$(CH_2)_n$-**CH_3**	24	2.7	20	**CH_3**-Ar or **CH_3**-CH=CH-
3	0.9	20	-CH(**CH_3**)-CH_2-	25	2.9	23	**CH_3**-Ar or **CH_3**-CH=CH-
4	0.9	23	-$(CH_2)_n$-CH**$(CH_3)_2$**	26	2.7	27	-CH=CH**CH_2**CH=CH-
5	0.9	30	**$(CH_3)_2$**-cyclic alkane	27	2.8	30	-CH=CH**CH_2**CH=CH-
6	0.9	33	**$(CH_3)_2$**-cyclic alkane	28	2.9	31	-CH=CH**CH_2**CH=CH-
7	1.3	23	-$(CH_2)_n$-**CH_2**-CH_3	29	2.2	30	**-CH-**Ar
8	1.3	30	**-$(CH_2)_n$-**CH_2-CH_3	30	2.4	34	**-CH_2-**Ar
9	1.3	32	**-$(CH_2)_n$-**CH_2-CH_3	31	2.4	43	**-CH_2-**COO
10	1.1	37	**-CH_2-**CH-	32	3.7	58	**-CH_2-**O-Ar
11	1.2	39	**-CH_2-**CH-	33	6.4	128	Aromatic ring –CH=
12	1.3	37	**-CH_2-**CH-	34	6.6	123	Aromatic ring –CH=
13	1.5	29	**-CH-**$(CH_3)_2$	35	7	127	Aromatic ring –CH=
14	1.4	33	-CH_2-**CH**(CH_3)-CH_2-	36	7.2	126	Aromatic ring –CH=
15	1.6	25	**-CH_2-**CH_2-COOR	37	7.4	125	Aromatic ring –CH=
16	2.1	14	**CH_3**-Ar or **CH_3**-CH=CH-	38	7.6	120	Aromatic ring –CH=
17	2.2	15	**CH_3**-Ar or **CH_3**-CH=CH-	39	7.6	126	Aromatic ring –CH=
18	2.3	13	**CH_3**-Ar or **CH_3**-CH=CH-	40	7.7	123	Aromatic ring –CH=
19	2.5	14	**CH_3**-Ar or **CH_3**-CH=CH-	41	7.7	121	Aromatic ring –CH=
20	2.6	16	**CH_3**-Ar or **CH_3**-CH=CH-	42	7.8	122	Aromatic ring –CH=
21	2.1	21	**CH_3**-Ar or **CH_3**-CH=CH-	43	7.9	123	Aromatic ring –CH=
22	2.3	20	**CH_3**-Ar or **CH_3**-CH=CH-				

2D HSQC spectrum of Kimmeridge bitumen is displayed in Figure 24, and the expanded aliphatic and aromatic regions shared almost all the contour spots as labeled in Figure 23. This indicated that the two bitumen samples extracted from Phosphoria and Kimmeridge shales had very similar molecular structures.

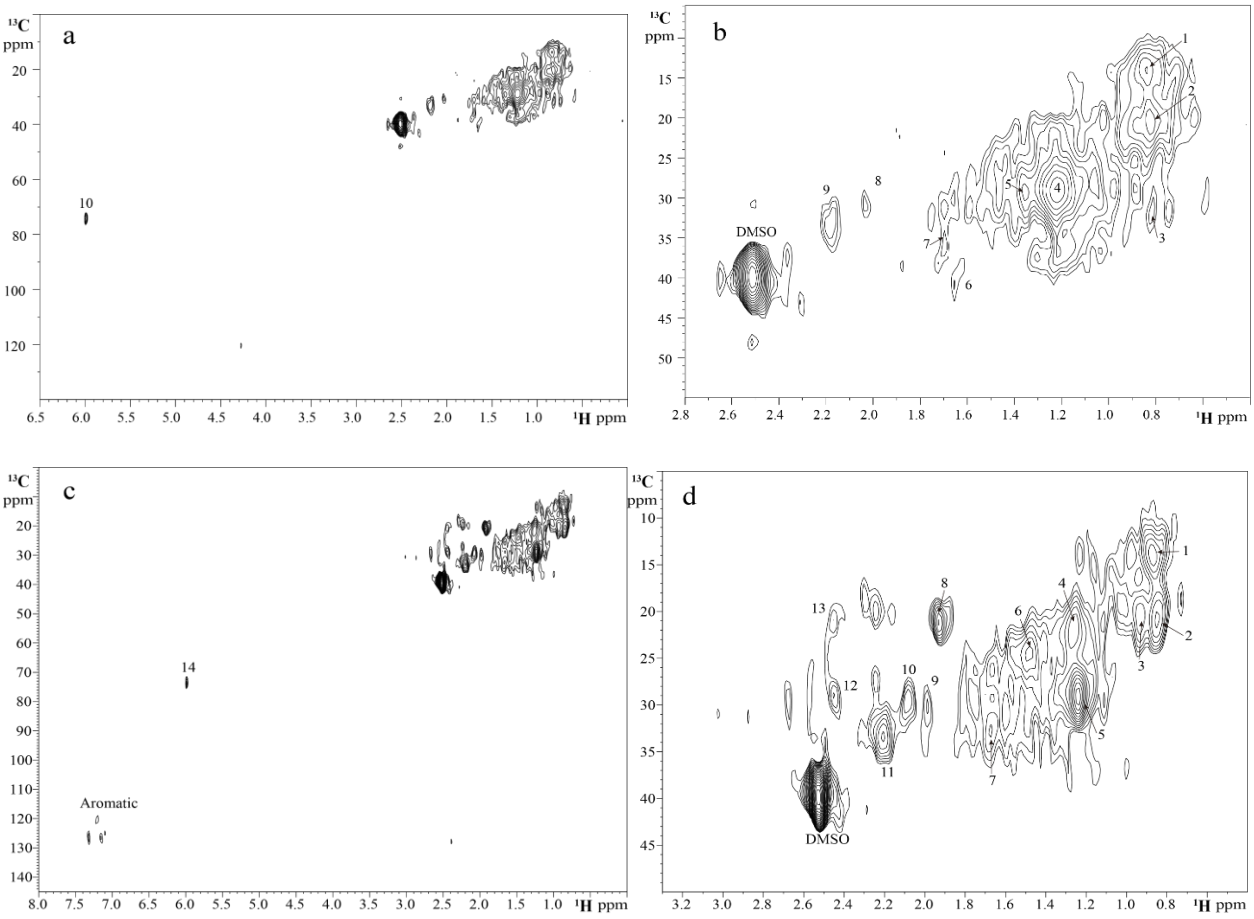

Figure 25. 2D ^{1}H-^{13}C HSQC spectrum from HRMAS NMR of Phosphoria shale (a) and its aliphatic region (b), and Kimmeridge shale (c) and its aliphatic region (d).

HRMAS NMR spectra

HRMAS NMR spectroscopy allows for the applications of liquid-state NMR techniques to samples that are not fully soluble, such as oil shale. Only the shale segments in contact with the solvent system showed NMR signals, and thus valuable information could be obtained on the interface moieties that were connected to the insoluble shale and mobile in the liquid phase. The HSQC spectra of Phosphoria and Kimmeridge shales from HRMAS NMR were presented in Figure 25. Their possible structure assignments were listed in Table 9. There were many similar signals as those in bitumen HSQC spectrum (Figure 23 b and Table 8), indicating that those structural fragments were most likely cleaved when swollen by organic solvents and that the structure of bitumen partially represented the structure of the organic matter in shale samples.

DISCUSSION

Kimmeridge clay formation is an important shale formation in UK and over much of northwest Europe, and has a history of multiple attempts at commercial exploitation because of the potential to produce millions of tons of shale oil (Speight, 2012). Analysis of shale oil generated from Kimmeridge formation has been carried out to provide information on oil shale genesis (Williams, 1987; Williams and Douglas, 1985, 1986). Kimmeridge clay is considered to be deposited during eustatic rise and transgression in an environment between open ocean and an enclosed marine basin (Gallois, 1976), which is consistent with the primary contribution of algal or bacterial organic matter source, and smaller yet various magnitude contribution of terrestrially derived organic material (Ramanampisoa and Disnar, 1994; Scotchman, 1991; Williams and Douglas, 1985).

Table 9. Contours selected from 2D ^{1}H-^{13}C HSQC spectrum from HRMAS NMR of Phosphoria and Kimmeridge shales and the possible chemical structures.

Phosphoria				Kimmeridge			
Contour #	^{1}H shift (ppm)	^{13}C shift (ppm)	Chemical structure	Contour #	^{1}H shift (ppm)	^{13}C shift (ppm)	Chemical structure
1	0.84	14	-$(CH_2)_n$-**CH_3**	1	0.87	14	-$(CH_2)_n$-**CH_3**
2	0.84	21	-CH(**CH_3**)-CH_2-	2	0.87	21	-CH(**CH_3**)-CH_2-
3	0.82	32	**$(CH_3)_2$**-cyclic alkane	3	0.95	21	-$(CH_2)_n$-CH**$(CH_3)_2$**
4	1.2	30	-**$(CH_2)_n$**-CH_2-CH_3	4	1.3	21	-$(CH_2)_n$-**CH_2**-CH_3
5	1.5	30	-**CH**-$(CH_3)_2$	5	1.3	29	-**$(CH_2)_n$**-CH_2-CH_3
6	1.6	40	-**CH**-	6	1.5	24	-**CH_2**-CH_2-COOR
7	1.7	36	-**CH**-	7	1.7	33	-CH_2-**CH**(CH_3)-CH_2-
8	2.0	31	-**CH_2**-Ar	8	1.9	21	-**CH**-CH_2-
9	2.2	33	-**CH_2**-COO	9	2	30	-**CH_2**-Ar
10	6.0	74	-C**H**-O	10	2.1	29	-**CH_2**-Ar
				11	2.2	33	-**CH_2**-COO
				12	2.5	29	-**CH_2**-CH=CH-
				13	2.5	21	-**CH_2**-CH=CH-
				14	6	74	-**CH**-O

The predominant methylene signal in the ^{13}C NMR multiCP spectrum of Kimmeridge shale sample (Figure 18 a) indicated the presence of poly-methylene chains in the molecular structure

of the organic matter in the sample, which was confirmed by the ^{1}H NMR spectrum of the corresponding bitumen sample (Figure 20 d), and also was supported by selective chemical degradation and GC data (Boucher et al., 1990). The different types of alkyl structures shown in the 2D ^{1}H-^{13}C HSQC spectrum of Kimmeridge bitumen sample (Figure 24 and Table 8) suggested extensive crosslinking, which also had been demonstrated before ((Boucher et al., 1990)). This might be the result of "vulcanization", when sulfur was incorporated into lipids to form cross-links between long carbon chains for the macromolecule to gain resistance to diagenetic degradations (Boussafir et al., 1995). This was also consistent with rich heterocyclic sulfur compounds generated during hydrous pyrolysis of Kimmeridge kerogen (Eglinton et al., 1988a) . A great portion of the aromatic signals in the NMR spectra (Figure 18) of our Kimmeridge sample could be from those sulfur-containing compounds, such as alkylthiophene, alkylbenzothiophene, and alkyldibenzothiophene.

Phosphoria formation is a major source rock for oil in Northern and central Rocky Mountain region (Claypool et al., 1978), and it is distinguished into four different facies based on their biomarker ratios (Dahl et al., 1993). The biomarkers detected in oil generated from Phosphoria source rocks included long chain alkanes as well as tricyclic alkanes (Silliman et al., 2002) and triaromatic steroids (Clayton and King, 1987), which was supported by the liquid-state and HRMAS 2D ^{1}H-^{13}C HSQC spectrum of our Phosphoria sample (Table 8 and 9). Sulfur containing heterocyclic aromatics were also present in oil from Phosphoria sample (Silliman et al., 2002), as it was in Kimmeridge sample.

For both Phosphoria and Kimmeridge samples, the multiCP/MAS spectra of raw shale, kerogen, and extracted rock were very much alike (Figure 17 a, b, and c and Figure 18 a, b, and c), indicating that the insoluble organic fraction dominated in the shale samples so that removal of the

soluble fraction did not significantly affect the carbon moiety distribution, similar to the study of Green River shale and kerogen study (Cao et al., 2013a). The alkyl carbon moiety (methyl groups and other alkyl in Table 6) in both kerogens were slightly lower than that in raw shales, which was consistent with the fact that both bitumen samples were rich in aliphatic carbons shown in Figure 20, resulting in the reduction of aliphatic carbons in kerogen samples relative to raw shales. These results showed that the acid treatments in kerogen isolation and chloroform treatment in bitumen extraction did not change the major organic component of Phosphoria and Kimmeridge shales except for the small proportion of soluble organic fraction.

The multiCP/MAS spectra of both shale samples were similar, but the functional group distribution (Table 6) and aromaticity (Table 7) of the two shales showed their detailed differences. Besides the subtle differences between some minor functional groups such as ketone/aldehyde, carbonyl, and O-alkyl, the main difference was the aromaticity. The aromaticity of Kimmeridge sample was lower than that of Phosphoria sample. Using aliphatic carbon moiety and alkyl-substituted aromatic moiety (Kelemen et al., 2007b), we could estimate that the average length of aliphatic chain in Kimmeridge shale was longer than that in Phosphoria shale.

In spite of their differences in geologic age and geographical location, Kimmeridge and Phosphoria shale samples share many similarities in solid-state ^{13}C NMR spectra, and the bitumen samples extracted from the two shales also shared a lot of same peaks in 2D ^{1}H-^{13}C HSQC spectra (Figure 23 and 13), indicating the same molecular structures (Table 8). Both samples are marine originated source rocks. The H/C ratio and S/C ratio of the two kerogens are very similar, with both bordering on the type IIS high sulfur marine kerogen type (Bolin et al., 2016). The two shales samples also generate similar distributions of hydrocarbon gases under hydrous pyrolysis and the bitumen samples have similar sulfur speciation in the XANES spectra (Bolin et al., 2016). The

similar hydrous pyrolysis products could explain the same assignments in the 2D ^{1}H-^{13}C HSQC spectra of two bitumen samples.

CHAPTER V

CONCLUSIONS

SUMMARY AND CONCLUSIONS OF THE RESEARCH

As routine ^{13}C solid-state NMR techniques in this dissertation, multiCP/MAS and multiCP/DD techniques can quickly generate quantitative spectra of the whole carbon and non-protonated carbon moieties from the organic matter in oil shale samples. After integration using the spectra, the percentages of different carbon moieties were calculated, resulted in quantitative assignments of various functional groups. Functional group assignments are the building blocks in elucidating and constructing molecular structures of the organic matter in oil shales. Since the quality of shale oil is directly related to the types of hydrocarbons, which depends on the structural characteristics of kerogen in the shale, advanced solid-state ^{13}C NMR is a good method for predicting the quality of crude oil generate by oil shale.

Aromaticity can be calculated using the multiCP/MAS and multiCP/DD spectra of shale samples, and it complements vitrinite reflectance and T_{max} from Rock-Eval pyrolysis on estimating thermal maturity of source rocks. Higher aromaticity generally corresponds with the source rock being more thermal mature. Higher aromaticity also means lower hydrogen index and lower aliphatic carbon content in the sample, which indicates low petroleum generating potential of the oil shale, supported by modified Fischer assay data.

By investigating quantitative functional group distributions and detailed structural characteristics of three shales with different and arguably extreme heteroatom contents using advanced ^{13}C solid-state NMR techniques, the following conclusions are drawn:

The high oxygen content in organic matter contained in the Ordovician Kukersite shale sample from Estonia corresponds with abundant aromatic C-O signals in the NMR results, and hence more non-protonated aromatic carbons. The non-protonated aromatic carbons are substituted with oxygen and alkyl chains. Meta dioxygen substitution is common. An improved structural model is constructed based on one from the literature and refined using our spectral data, and the simulated ^{13}C NMR spectra of the model matched the measured spectra of Kukersite shale reasonably well.

The high organic sulfur content in the organic matter present in Jordanian marinite shale from the Upper Cretaceous Ghareb Formation is mostly represented in the form of aromatic sulfur based on other studies, and is consistent with the high aromaticity of organic matter in the sample examined for this work.

Upper Permian torbanite shale of the Glen Davis Formation contains organic matter with a relatively low total heteroatom content and produces comparatively simpler spectra with only aromatic and aliphatic bands detected due to the presence of few if any oxygen-containing functional groups.

These results further previous work on Green River Formation and New Albany shale studies, among others, to examine how kerogen structure varies for different organic matter sources and depositional environments. By examining source rock with kerogens containing extreme heteroatom contents, we can assess the kinds of chemical structures that may be present in other more typical kerogens. With more reliable structural models of kerogen, it may be possible to refine models of thermal decomposition of kerogen to petroleum and potentially predict specific oil and gas properties a priori based solely on characterization of immature source rock samples (Durand, 1980b; Vandenbroucke and Largeau, 2007).

Two shale samples and their corresponding kerogens, extracted rocks, and bitumens were investigated using advanced solid-state NMR, liquid-state NMR, and HRMAS NMR techniques to characterize their possible molecular structual components. Despite the differences in geologic age and depositional location, Kimmeridge and Phosphoria formation have similar solid-state ^{13}C NMR spectra from shale, kerogen, and extracted rock samples, and they share almost the same signals in liquid-state 2D ^{1}H-^{13}C HSQC spectra from bitumen samples. We speculate the organic matter in Kimmeridge and Phosphoria samples have very similar molecular structure. The speculation can be supported by elemental analysis and XANES spectral data.

Advanced solid-state NMR techniques, along with liquid-state and HRMAS NMR techniques, have great ability in predicting oil yield of shale formation and quality of its shale oil by characterizing molecular structures of the organic matter in source rocks related to quantity and quality of potential hydrocarbon product.

DIRECTION FOR FUTURE RESEARCH

A good extension of this research is to develop a standard approach for predicting oil quantity and quality that would be produced by a shale quickly and non-destructively, using advanced solid-state NMR techniques. In order to reach this goal, a lot of well-studied shale formations should be measured with advanced NMR techniques to obtain quantitative data, and then the NMR data can be analyzed with other available data, such as elemental composition, mineralogy, chemical degradation, chromaography, mass spectrometry, infrared spectroscopy, Fischer assay, hydrous pyrolysis, and rock-eval pyrolysis. Statistical analyses can be applied when there are enough shale samples analyzed, and a good correlation between the NMR data and potential oil yied and quality data may be generated with a reasonable error.

Further research can also be carried out regarding the structural model of the kerogen in different shale formations. Quatitative solid-state NMR spectra are needed in order to construct a reliable model. Having more distictive functional groups in the structure improves the signals that can be presented in NMR spectra, and enhances the accuracy of the structural model. When simulated spetra match the experimental spectra on every single peak, the accuracy of the structural model is proven.

BIBLIOGRAPHY

Abbas, O., Rebufa, C., Dupuy, N., Permanyer, A., Kister, J., 2012. PLS regression on spectroscopic data for the prediction of crude oil quality: API gravity and aliphatic/aromatic ratio. Fuel 98, 5-14.

Adebiyi, F.M., Akhigbe, G.E., 2015. Characterization of paraffinic hydrocarbon fraction of Nigerian bitumen using multivariate analytical techniques. Journal of Unconventional Oil and Gas Resources 12, 34-44.

Ahmad, N., Williams, P.T., 1998. Influence of particle grain size on the yield and composition of products from the pyrolysis of oil shales. Journal of Analytical and Applied Pyrolysis 46, 31-49.

Alam, T.M., Jenkins, J.E., 2012. HR-MAS NMR spectroscopy in material science. Advanced aspects of spectroscopy. Intech Open, 279-306.

Anderson, J.M., Johnson, R.L., Schmidt-Rohr, K., Shanks, B.H., 2014. Solid state NMR study of chemical structure and hydrothermal deactivation of moderate-temperature carbon materials with acidic SO3H sites. Carbon 74, 333-345.

Aske, N., Kallevik, H., Sjöblom, J., 2001. Determination of saturate, aromatic, resin, and asphaltenic (SARA) components in crude oils by means of infrared and near-infrared spectroscopy. Energy & Fuels 15, 1304-1312.

Audino, M., Grice, K., Alexander, R., Boreham, C.J., Kagi, R.I., 2001. Unusual distribution of monomethylalkanes in Botryococcus braunii–rich samples: origin and significance. Geochimica et Cosmochimica Acta 65, 1995-2006.

Audino, M., Grice, K., Alexander, R., Kagi, R., 2004. Macrocyclic alkanes in crude oils and sediment extracts: enrichment using molecular sieves. Organic Geochemistry 35, 661-663.

Baranzelli, C., Vandecasteele, I., Ribeiro Barranco, R., Mari i Rivero, I., Pelletier, N., Batelaan, O., Lavalle, C., 2015. Scenarios for shale gas development and their related land use impacts in the Baltic Basin, Northern Poland. Energy Policy 84, 80-95.

Barron, P.F., 1982. ^{13}C cross-polarization n.m.r. examination of the Glen Davis oil shale deposit. Fuel 61, 1282-1284.

Bartholomew, T.V., Mauter, M.S., 2016. Multiobjective optimization model for minimizing cost and environmental impact in shale gas water and wastewater management. ACS Sustainable Chemistry & Engineering 4, 3728-3735.

Bartis, J.T., LaTourrette, T., Dixon, L., Peterson, D., Cecchine, G., 2005. Oil shale development in the United States: prospects and policy issues. Rand Corporation.

Behar, F., Beaumont, V., Penteado, H.D.B., 2001. Rock-Eval 6 technology: performances and developments. Oil & Gas Science and Technology 56, 111-134.

Birdwell, J.E., 2017. Oil Shale. Springer Encyclopedia of Geochemistry.

Birdwell, J.E., Lewan, M., Bake, K.D., Bolin, T.B., Craddock, P.R., Forsythe, J.C., Pomerantz, A.E., 2018. Evolution of sulfur speciation in bitumen through hydrous pyrolysis induced thermal maturation of Jordanian Ghareb Formation oil shale. Fuel 219, 214-222.

Birdwell, J.E., Washburn, K.E., 2015. Rapid Analysis of Kerogen Hydrogen-to-Carbon Ratios in Shale and Mudrocks by Laser-Induced Breakdown Spectroscopy. Energy & Fuels 29, 6999-7004.

Blokker, P., van Bergen, P., Pancost, R., Collinson, M.E., de Leeuw, J.W., Sinninghe Damste, J.S., 2001. The chemical structure of Gloeocapsomorpha prisca microfossils: implications for their origin. Geochimica et Cosmochimica Acta 65, 885-900.

Bolin, T.B., Birdwell, J.E., Lewan, M.D., Hill, R.J., Grayson, M.B., Mitra-Kirtley, S., Bake, K.D., Craddock, P.R., Abdallah, W., Pomerantz, A.E., 2016. Sulfur Species in Source Rock Bitumen before and after Hydrous Pyrolysis Determined by X-ray Absorption Near-Edge Structure. Energy & Fuels 30, 6264-6270.

Boreham, C.J., Summons, R.E., Roksandic, Z., Dowling, L.M., Hutton, A.C., 1994. Chemical, molecular and isotopic differentiation of organic facies in the Tertiary lacustrine Duaringa oil shale deposit, Queensland, Australia. Organic Geochemistry 21, 685-712.

Borrego, A., Blanco, C., Prado, J., Díaz, C., Guillén, M., 1996. ^{1}H NMR and FTIR spectroscopic studies of bitumen and shale oil from selected Spanish oil shales. Energy & fuels 10, 77-84.

Boucher, R.J., Standen, G., Patience, R.L., Eglinton, G., 1990. Molecular characterisation of kerogen from the Kimmeridge clay formation by mild selective chemical degradation and solid state ^{13}C-NMR. Organic Geochemistry 16, 951-958.

Boussafir, M., Gelin, F., Lallier-Vergès, E., Derenne, S., Bertrand, P., Largeau, C., 1995. Electron microscopy and pyrolysis of kerogens from the Kimmeridge Clay Formation, UK: Source organisms, preservation processes, and origin of microcycles. Geochimica et Cosmochimica Acta 59, 3731-3747.

Brittingham, M.C., Maloney, K.O., Farag, A.M., Harper, D.D., Bowen, Z.H., 2014. Ecological risks of shale oil and gas development to wildlife, aquatic resources and their habitats. Environmental science & technology 48, 11034-11047.

Bronnimann, C.E., Ridenour, C.F., Kinney, D.R., Maciel, G.E., 1992. 2D 1H-13C heteronuclear correlation spectra of representative organic solids. Journal of Magnetic Resonance (1969) 97, 522-534.

Bsieso, M., 2003. Jordan's experience in oil shale studies employing different technologies. Oil shale 20, 360-370.

Burdelnaya, N., Bushnev, D., Mokeev, M., 2013. Changes in the composition of bitumen extracts and chemical structure of kerogen during hydrous pyrolysis. Geochemistry International 51, 738-750.

Burnham, A., Han, J., Clark, C.E., Wang, M., Dunn, J.B., Palou-Rivera, I., 2012. Life-cycle greenhouse gas emissions of shale gas, natural gas, coal, and petroleum. Environmental science & technology 46, 619-627.

Cao, X., Birdwell, J.E., Chappell, M.A., Li, Y., Pignatello, J.J., Mao, J., 2013a. Characterization of oil shale, isolated kerogen, and postpyrolysis residues using advanced ^{13}C solid-state nuclear magnetic resonance spectroscopy. AAPG bulletin 97, 421-436.

Cao, X., Yang, J., Mao, J., 2013b. Characterization of kerogen using solid-state nuclear magnetic resonance spectroscopy: A review. International Journal of Coal Geology 108, 83-90.

Claypool, G.E., Love, A.H., Maughan, E.K., 1978. Organic geochemistry, incipient metamorphism, and oil generation in black shale members of Phosphoria Formation, western interior United States. AAPG Bulletin 62, 98-120.

Clayton, J.L., King, J.D., 1987. Effects of weathering on biological marker and aromatic hydrocarbon composition of organic matter in Phosphoria shale outcrop. Geochimica et Cosmochimica Acta 51, 2153-2157.

Congress, Year.

Coussens, C., Martinez, M., 2013. Health impact assessment of shale gas extraction: workshop summary.

Craig, H., 1953. The geochemistry of the stable carbon isotopes. Geochimica et Cosmochimica Acta 3, 53-92.

Crisp, P., Ellis, J., Hutton, A., Saxby, J., 1987. Australian oil shales: a compendium of geological and chemical data.

Dahl, J., Michael Moldowan, J., Sundararaman, P., 1993. Relationship of biomarker distribution to depositional environment: Phosphoria Formation, Montana, U.S.A. Organic Geochemistry 20, 1001-1017.

De Leeuw, J., Largeau, C., 1993. A review of macromolecular organic compounds that comprise living organisms and their role in kerogen, coal, and petroleum formation, Organic Geochemistry. Springer, pp. 23-72.

Dennis, L.W., Maciel, G.E., Hatcher, P.G., Simoneit, B.R., 1982. ^{13}C Nuclear magnetic resonance studies of kerogen from Cretaceous black shales thermally altered by basaltic intrusions and laboratory simulations. Geochimica et Cosmochimica Acta 46, 901-907.

Derenne, S., Largeau, C., Casadevall, E., Connan, J., 1988. Comparison of torbanites of various origins and evolutionary stages. Bacterial contribution to their formation. Causes of the lack of botryococcane in bitumens. Organic Geochemistry 12, 43-59.

Derenne, S., Largeau, C., Casadevall, E., Sinninghe Damsté, J.S., Tegelaar, E.W., de Leeuw, J.W., 1990. Characterization of Estonian Kukersite by spectroscopy and pyrolysis: Evidence for abundant alkyl phenolic moieties in an Ordovician, marine, type II/I kerogen. Organic Geochemistry 16, 873-888.

Durand, B., 1980a. Kerogen: Insoluble organic matter from sedimentary rocks. Editions technip.

Durand, B., 1980b. Sedimentary organic matter and kerogen. Definition and quantitative importance of kerogen. Kerogen: Insoluble organic matter from sedimentary rocks, 13-34.

Dyni, J.R., 2003. Geology and resources of some world oil-shale deposits. Oil shale 20, 193-253.

Eglinton, T.I., Douglas, A.G., Rowland, S.J., 1988a. Release of aliphatic, aromatic and sulphur compounds from Kimmeridge kerogen by hydrous pyrolysis: A quantitative study. Organic Geochemistry 13, 655-663.

Eglinton, T.I., Philp, R.P., Rowland, S.J., 1988b. Flash pyrolysis of artificially matured kerogens from the Kimmeridge Clay, U.K. Organic Geochemistry 12, 33-41.

Engel, M., Macko, S.A., 2013a. Organic geochemistry: principles and applications. Springer Science & Business Media.

Engel, M.H., Macko, S.A., 2013b. Organic geochemistry: principles and applications. Springer Science & Business Media.

Eshleman, K.N., Elmore, A., 2013. Recommended Best Management Practices for Marcellus Shale Gas Development in Maryland. Appalachian Laboratory University of Maryland Center for Environmental Science Frostburg, MD 21532.

Estrada, J.M., Bhamidimarri, R., 2016. A review of the issues and treatment options for wastewater from shale gas extraction by hydraulic fracturing. Fuel 182, 292-303.

Ethridge, S., Bredfeldt, T., Sheedy, K., Shirley, S., Lopez, G., Honeycutt, M., 2015. The Barnett Shale: From problem formulation to risk management. Journal of Unconventional Oil and Gas Resources 11, 95-110.

Fang, C., Zheng, D., Liu, D., 2008. Main Problems in Development and Utilization of Oil Shale and Status of the In-situ Conversion Process Technology in China.

Fang, H., Jianyu, C., 1992. The cause and mechanism of vitrinite reflectance anomalies. Journal of Petroleum Geology 15, 419-434.

Fathoni, A.Z., Batts, B., 1992. A literature review of fuel stability studies with a particular emphasis on shale oil. Energy & fuels 6, 681-693.

Figueroa Pilz, F., Dowey, P.J., Fauchille, A.L., Courtois, L., Bay, B., Ma, L., Taylor, K.G., Mecklenburgh, J., Lee, P.D., 2017. Synchrotron tomographic quantification of strain and fracture during simulated thermal maturation of an organic‐rich shale, UK Kimmeridge Clay. Journal of Geophysical Research: Solid Earth 122, 2553-2564.

Fletcher, T.H., Gillis, R., Adams, J., Hall, T., Mayne, C.L., Solum, M.S., Pugmire, R.J., 2014. Characterization of Macromolecular Structure Elements from a Green River Oil Shale, II. Characterization of Pyrolysis Products by 13C NMR, GC/MS, and FTIR. Energy & Fuels 28, 2959-2970.

Gallois, R., 1976. Coccolith blooms in the Kimmeridge Clay and origin of North Sea Oil. Nature 259, 473-475.

Gao, G., Zhang, W., Xiang, B., Liu, G., Ren, J., 2016. Geochemistry characteristics and hydrocarbon-generating potential of lacustrine source rock in Lucaogou Formation of the Jimusaer Sag, Junggar Basin. Journal of Petroleum Science and Engineering 145, 168-182.

Garrigues, P., Oudin, J.L., Parlanti, E., Monin, J.C., Robcis, S., Bellocq, J., 1990. Alkylated phenanthrene distribution in artificially matured kerogens from Kimmeridge clay and the Brent Formation (North Sea). Organic Geochemistry 16, 167-173.

Glikson, M., 1983. Microbiological precursors of coorongite and torbanite and the role of microbial degradation in the formation of kerogen. Organic Geochemistry 4, 161-172.

Glikson, M., Chappell, B.W., Freeman, R.S., Webber, E., 1985. Trace elements in oil shales, their source and organic association with particular reference to Australian deposits. Chemical Geology 53, 155-174.

Grice, K., Audino, M., Boreham, C.J., Alexander, R., Kagi, R.I., 2001. Distributions and stable carbon isotopic compositions of biomarkers in torbanites from different palaeogeographical locations. Organic Geochemistry 32, 1195-1210.

Guan, D., Xu, X., Li, Z., Zheng, L., Tan, C., Yao, Y., 2017. Current Status of Hydrocarbon Generation from Source Rocks Theory, Theory and Practice of Hydrocarbon Generation within Space-Limited Source Rocks. Springer, pp. 19-68.

Hakimi, M.H., Abdullah, W.H., Shalaby, M.R., 2010. Source rock characterization and oil generating potential of the Jurassic Madbi Formation, onshore East Shabowah oilfields, Republic of Yemen. Organic Geochemistry 41, 513-521.

Han, X., Kulaots, I., Jiang, X., Suuberg, E.M., 2014. Review of oil shale semicoke and its combustion utilization. Fuel 126, 143-161.

Hartstein, A.M., Ogunsola, O.I., Ogunsola, O., 2010. Oil shale: A solution to the liquid fuel dilemma. American Chemical Society.

Hein, J.R., 2003. Life cycle of the Phosphoria Formation: from deposition to the post-mining environment. Gulf Professional Publishing.

Hillier, J.L., Fletcher, T.H., Solum, M.S., Pugmire, R.J., 2013. Characterization of Macromolecular Structure of Pyrolysis Products from a Colorado Green River Oil Shale. Industrial & Engineering Chemistry Research 52, 15522-15532.

Hu, S., Xiao, C., Jiang, X., Liang, X., 2018. Potential impact of in-situ oil shale exploitation on aquifer system. Water 10, 649.

Huang, Z., Liang, T., Zhan, Z.-W., Zou, Y.-R., Li, M., Peng, P.a., 2018. Chemical structure evolution of kerogen during oil generation. Marine and Petroleum Geology 98, 422-436.

Hutton, A., Kantsler, A., Cook, A., McKirdy, D., 1980. Organic matter in oil shales. The APPEA Journal 20, 44-67.

Hutton, A.C., 1987. Petrographic classification of oil shales. International Journal of Coal Geology 8, 203-231.

Iqbal, S., Rodríguez-LLansola, F., Escuder, B., Miravet, J.F., Verbruggen, I., Willem, R., 2010. HRMAS 1H NMR as a tool for the study of supramolecular gels. Soft Matter 6, 1875-1878.

Jaber, J., Probert, S., Williams, P., 1999. Evaluation of oil yield from Jordanian oil shales. Energy 24, 761-781.

Johnson, H.R., Crawford, P.M., Bunger, J.W., 2004. Strategic significance of America's oil shale resource: Volume 2--oil shale resources technology and economics. United States Department of Energy, Office of Naval Petroleum and Oil Shale ….

Johnson, R.L., Schmidt-Rohr, K., 2014. Quantitative solid-state ^{13}C NMR with signal enhancement by multiple cross polarization. Journal of Magnetic Resonance 239, 44-49.

Kelemen, S., Afeworki, M., Gorbaty, M., Sansone, M., Kwiatek, P., Walters, C., Freund, H., Siskin, M., Bence, A., Curry, D., 2007a. Direct characterization of kerogen by X-ray and solid-state 13C nuclear magnetic resonance methods. Energy & Fuels 21, 1548-1561.

Kelemen, S.R., Afeworki, M., Gorbaty, M.L., Sansone, M., Kwiatek, P.J., Walters, C.C., Freund, H., Siskin, M., Bence, A.E., Curry, D.J., Solum, M., Pugmire, R.J., Vandenbroucke, M., Leblond, M., Behar, F., 2007b. Direct Characterization of Kerogen by X-ray and Solid-State ^{13}C Nuclear Magnetic Resonance Methods. Energy & Fuels 21, 1548-1561.

Kelemen, S.R., Walters, C.C., Kwiatek, P.J., Freund, H., Afeworki, M., Sansone, M., Lamberti, W.A., Pottorf, R.J., Machel, H.G., Peters, K.E., Bolin, T., 2010. Characterization of solid bitumens originating from thermal chemical alteration and thermochemical sulfate reduction. Geochimica et Cosmochimica Acta 74, 5305-5332.

Knauss, K.G., Copenhaver, S.A., L. Braun, R., Burnham, A.K., 1997. Hydrous pyrolysis of New Albany and Phosphoria Shales: production kinetics of carboxylic acids and light hydrocarbons and interactions between the inorganic and organic chemical systems. Organic Geochemistry 27, 477-496.

Kohnen, M.E.L., Sinninghe Damsté, J.S., Rijpstra, W.I.C., de Leeuw, J.W., 1990. Alkylthiophenes as Sensitive Indicators of Palaeoenvironmental Changes, Geochemistry of Sulfur in Fossil Fuels. American Chemical Society, pp. 444-485.

Koopmans, M.P., Carson, F.C., Sinninghe Damsté, J.S., Lewan, M.D., 1998a. Biomarker generation from Type II-S kerogens in claystone and limestone during hydrous and anhydrous pyrolysis1NIOZ Contribution No. 3217.1. Organic Geochemistry 29, 1395-1402.

Koopmans, M.P., Rijpstra, W.I.C., de Leeuw, J.W., Lewan, M.D., Damsté, J.S.S., 1998b. Artificial maturation of an immature sulfur- and organic matter-rich limestone from the Ghareb Formation, Jordan. Organic Geochemistry 28, 503-521.

Kuangzong, Q., Deyu, C., Zhanguang, L., 1991. A new method to estimate the oil and gas potentials of coals and kerogens by solid state ^{13}C NMR spectroscopy. Organic Geochemistry 17, 865-872.

Kuuskraa, V., Stevens, S.H., Moodhe, K.D., 2013. Technically recoverable shale oil and shale gas resources: an assessment of 137 shale formations in 41 countries outside the United States. US Energy Information Administration, US Department of Energy.

Lambert, J.B., Mazzola, E.P., Ridge, C.D., 2019. Nuclear magnetic resonance spectroscopy: an introduction to principles, applications, and experimental methods. Wiley.

Lee, S., 1990. Oil shale technology. CRC Press.

Lewan, M.D., Bjorøy, M., Dolcater, D.L., 1986. Effects of thermal maturation on steroid hydrocarbons as determined by hydrous pyrolysis of Phosphoria Retort Shale. Geochimica et Cosmochimica Acta 50, 1977-1987.

Lille, U., 2003. Current knowledge on the origin and structure of Estonian kukersite kerogen. Oil Shale 20, 253-263.

Lille, Ü., Heinmaa, I., Pehk, T., 2003. Molecular model of Estonian kukersite kerogen evaluated by ^{13}C MAS NMR spectra☆. Fuel 82, 799-804.

Longbottom, T.L., Hockaday, W.C., Boling, K.S., Li, G., Letourmy, Y., Dong, H., Dworkin, S.I., 2016. Organic structural properties of kerogen as predictors of source rock type and hydrocarbon potential. Fuel 184, 792-798.

Macauley, G., Ball, F., Powell, T., 1984. A review of the Carboniferous Albert Formation oil shales, New Brunswick. Bulletin of Canadian Petroleum Geology 32, 27-37.

Maciel, G., Dennis, L., 1981. Comparison of oil shales and kerogen concentrates by 13C nuclear magnetic resonance. Organic Geochemistry 3, 105-109.

Maciel, G.E., Bartuska, V.J., Miknis, F.P., 1978. Correlation between oil yields of oil shales and ^{13}C nuclear magnetic resonance spectra. Fuel 57, 505-506.

Maciel, G.E., Bartuska, V.J., Miknis, F.P., 1979. Improvement in correlation between oil yields of oil shales and ^{13}C n.m.r. spectra. Fuel 58, 155-156.

Mani, D., Kalpana, M.S., Patil, D.J., Dayal, A.M., 2017. Chapter 3 - Organic Matter in Gas Shales: Origin, Evolution, and Characterization, in: Dayal, A.M., Mani, D. (Eds.), Shale Gas. Elsevier, pp. 25-54.

Mann, A.l., Patience, R.l., Poplett, I.J.F., 1991. Determination of molecular structure of kerogens using ^{13}C NMR spectroscopy: I. The effects of variation in kerogen type. Geochimica et Cosmochimica Acta 55, 2259-2268.

Mao, J.-D., Johnson, R., Lehmann, J., Olk, D., Neves, E.G., Thompson, M., Schmidt-Rohr, K., 2012. Abundant and stable char residues in soils: implications for soil fertility and carbon sequestration. Environmental science & technology 46, 9571-9576.

Mao, J., Cao, X., 2011. Characterization of heterogeneities and domains in aquatic and sedimentary organic matter by ^{1}H spin diffusion: Potential for elucidating the formation mechanisms. Limnology and Oceanography: Methods 9, 533-542.

Mao, J., Cao, X., Olk, D.C., Chu, W., Schmidt-Rohr, K., 2017a. Advanced solid-state NMR spectroscopy of natural organic matter. Progress in Nuclear Magnetic Resonance Spectroscopy 100, 17-51.

Mao, J., Cao, X., Olk, D.C., Chu, W., Schmidt-Rohr, K., 2017b. Advanced solid-state NMR spectroscopy of natural organic matter. Progress in Nuclear Magnetic Resonance Spectroscopy 100, 17-51.

Mao, J., Chen, N., Cao, X., 2011. Characterization of humic substances by advanced solid state NMR spectroscopy: Demonstration of a systematic approach. Organic Geochemistry 42, 891-902.

Mao, J., Cory, R.M., McKnight, D.M., Schmidt-Rohr, K., 2007. Characterization of a nitrogen-rich fulvic acid and its precursor algae from solid state NMR. Organic Geochemistry 38, 1277-1292.

Mao, J., Fang, X., Lan, Y., Schimmelmann, A., Mastalerz, M., Xu, L., Schmidt-Rohr, K., 2010. Chemical and nanometer-scale structure of kerogen and its change during thermal maturation investigated by advanced solid-state ^{13}C NMR spectroscopy. Geochimica et Cosmochimica Acta 74, 2110-2127.

Mao, J., Hu, W., Schmidt-Rohr, K., Davies, G., Ghabbour, E., Xing, B., 2000. Quantitative characterization of humic substances by solid-state carbon-13 nuclear magnetic resonance. Soil Science Society of America Journal 64, 873-884.

Mao, J.D., Schmidt-Rohr, K., 2004a. Accurate Quantification of Aromaticity and Nonprotonated Aromatic Carbon Fraction in Natural Organic Matter by ^{13}C Solid-State Nuclear Magnetic Resonance. Environmental Science & Technology 38, 2680-2684.

Mao, J.D., Schmidt-Rohr, K., 2004b. Separation of aromatic-carbon ^{13}C NMR signals from di-oxygenated alkyl bands by a chemical-shift-anisotropy filter. Solid State Nuclear Magnetic Resonance 26, 36-45.

Mao, J.D., Xing, B., Schmidt-Rohr, K., 2001. New Structural Information on a Humic Acid from Two-Dimensional ^{1}H-^{13}C Correlation Solid-State Nuclear Magnetic Resonance. Environmental Science & Technology 35, 1928-1934.

Miknis, F.P., 1992. Combined n.m.r. and Fischer assay study of oil shale conversion. Fuel 71, 731-738.

Miknis, F.P., Conn, P.J., 1986. A common relation for correlating pyrolysis yields of coals and oil shales. Fuel 65, 248-250.

Miknis, F.P., Lindner, A.W., John Gannon, A., Davis, M.F., Maciel, G.E., 1984. Solid state ^{13}C NMR studies of selected oil shales from Queensland, Australia. Organic Geochemistry 7, 239-248.

Miknis, F.P., Netzel, D.A., Smith, J.W., Mast, M.A., Maciel, G.E., 1982a. ^{13}C NMR measurements of the genetic potentials of oil shales. Geochimica et Cosmochimica Acta 46, 977-984.

Miknis, F.P., Smith, J.W., Maughan, E.K., Maciel, G.E., 1982b. Nuclear magnetic resonance: a technique for direct nondestructive evaluation of source-rock potential. AAPG Bulletin 66, 1396-1401.

Morgan, V.G., Barbosa, L.L., Lacerda Jr, V., Vinicius Ribeiro de Castro, E.q., 2014. Evaluation of the physicochemical properties of the postsalt crude oil for low-field NMR. Industrial & Engineering Chemistry Research 53, 8881-8889.

Nasiri, M., Jafari, I., Parniankhoy, B., 2017. Oil and gas produced water management: a review of treatment technologies, challenges, and opportunities. Chemical engineering communications 204, 990-1005.

Nazzal, J.M., 2002. Influence of heating rate on the pyrolysis of Jordan oil shale. Journal of analytical and applied pyrolysis 62, 225-238.

Nazzal, J.M., 2008. The influence of grain size on the products yield and shale oil composition from the pyrolysis of Sultani oil shale. Energy conversion and management 49, 3278-3286.

Opella, S.J., Frey, M.H., 1979. Selection of nonprotonated carbon resonances in solid-state nuclear magnetic resonance. Journal of the American Chemical Society 101, 5854-5856.

Orendt, A.M., Pimienta, I.S.O., Badu, S.R., Solum, M.S., Pugmire, R.J., Facelli, J.C., Locke, D.R., Chapman, K.W., Chupas, P.J., Winans, R.E., 2013. Three-Dimensional Structure of the Siskin Green River Oil Shale Kerogen Model: A Comparison between Calculated and Observed Properties. Energy & Fuels 27, 702-710.

Padula, V.T., 1969. Oil shale of Permian Irati Formation, Brazil. AAPG Bulletin 53, 591-602.

Palmer, S.R., Gaines, A.F., Jarvie, A.W.P., 1987. Analysis of the structures of the organic materials in Kimmeridge and Oxford clays. Fuel 66, 499-504.

Pan, Y., Zhang, X., Liu, S., Yang, S., Ren, N., 2012. A review on technologies for oil shale surface retort. J. Chem. Soc. Pak 34, 1331-1338.

Park, M.-H., Choi, J., Kil, Y., Kwon, Y.-K., Kim, J.-H., 2013. Geochemical analyses on bituminous carbonate reservoir in Alberta, Canada: focusing on the GC/GC-MS results of bitumen. Geosciences Journal 17, 221-233.

Polito, L., Colombo, M., Monti, D., Melato, S., Caneva, E., Prosperi, D., 2008. Resolving the structure of ligands bound to the surface of superparamagnetic iron oxide nanoparticles by high-resolution

magic-angle spinning NMR spectroscopy. Journal of the American Chemical Society 130, 12712-12724.

Põllumaa, L., Maloveryan, A., Trapido, M., Sillak, H., Kahru, A., 2001. Study of the environmental hazard caused by the oil shale industry solid waste. Alternatives to Laboratory Animals 29, 259-267.

Price, L.C., Wenger, L.M., 1992. The influence of pressure on petroleum generation and maturation as suggested by aqueous pyrolysis. Organic Geochemistry 19, 141-159.

Qian, J., Wang, J., Li, S., 2003. Oil shale development in China. Oil shale 20, 356-359.

Ramanampisoa, L., Disnar, J.R., 1994. Primary control of paleoproduction on organic matter preservation and accumulation in the Kimmeridge rocks of Yorkshire (UK). Organic Geochemistry 21, 1153-1167.

Raukas, A., Punning, J.-M., 2009. Environmental problems in the Estonian oil shale industry. Energy & Environmental Science 2, 723-728.

Reinsalu, E., Valgma, I., 2003. Geotechnical processes in closed oil shale mines. Oil Shale 20, 398-403.

Rigby, D., Batts, B.D., 1986. The isotopic composition of nitrogen in Australian coals and oil shales. Chemical Geology: Isotope Geoscience section 58, 273-282.

Robinson, A.L., 2014. Air pollution emissions from shale gas development and production. Coussens C and Martinez RM (Rapporteurs): IOM (Institute of Medicine).

Roen, J.B., Kepferle, R.C., 1993. Petroleum geology of the Devonian and Mississippian black shale of eastern North America. Report.

Routson, R., Wildung, R., Bean, R., 1979. A review of the environmental impact of ground disposal of oil shale wastes. Journal of environmental quality 8, 14-19.

Rullkötter, J., Michaelis, W., 1990. The structure of kerogen and related materials. A review of recent progress and future trends. Organic Geochemistry 16, 829-852.

Russell, P.L., 1990. Oil shales of the world: their origin, occurrence & exploitation.

Salmon, E., Behar, F., Hatcher, P.G., 2011. Molecular characterization of Type I kerogen from the Green River Formation using advanced NMR techniques in combination with electrospray ionization/ultrahigh resolution mass spectrometry. Organic geochemistry 42, 301-315.

Scotchman, I.C., 1991. Kerogen facies and maturity of the Kimmeridge Clay Formation in southern and eastern England. Marine and Petroleum Geology 8, 278-295.

Silliman, J.E., Li, M., Yao, H., Hwang, R., 2002. Molecular distributions and geochemical implications of pyrrolic nitrogen compounds in the Permian Phosphoria Formation derived oils of Wyoming. Organic Geochemistry 33, 527-544.

Simpson, A., 2001. Multidimensional solution state NMR of humic substances: a practical guide and review. Soil science 166, 795-809.

Simpson, A.J., Kingery, W.L., Shaw, D.R., Spraul, M., Humpfer, E., Dvortsak, P., 2001. The application of 1H HR-MAS NMR spectroscopy for the study of structures and associations of organic components at the solid− aqueous interface of a whole soil. Environmental science & technology 35, 3321-3325.

Speight, J.G., 2012. Shale oil production processes. Gulf Professional Publishing.

Stasiuk, L., Snowdon, L., 1997. Fluorescence micro-spectrometry of synthetic and natural hydrocarbon fluid inclusions: crude oil chemistry, density and application to petroleum migration. Applied Geochemistry 12, 229-241.

Stratiev, D., Dinkov, R., Petkov, K., Stanulov, K., 2010. Evaluation of crude oil quality. Petroleum & Coal 52, 35-43.

Suryanarayana, C., Norton, M.G., 1998. X-Ray Diffraction: A Practical Approach. Springer Science & Business Media.

Taylor, R.W., Burnham, A.K., Mallon, R.G., Morris, C.J., 1982. SO_2 emissions from the oxidation of retorted oil shale. Fuel 61, 781-782.

Tissot, B., Vandenbroucke, M., 1983. Geochemistry and pyrolysis of oil shales. Prepr. Pap.-Am. Chem. Soc., Div. Fuel Chem.;(United States) 28.

Tissot, B.P., Welte, D.H., 1984. Petroleum formation and occurrence. Springer Science & Business Media.

Tong, J., Jiang, X., Han, X., Wang, X., 2016. Evaluation of the macromolecular structure of Huadian oil shale kerogen using molecular modeling. Fuel 181, 330-339.

Trewhella, M.J., Poplett, I.J.F., Grint, A., 1986. Structure of Green River oil shale kerogen: Determination using solid state ^{13}C n.m.r. spectroscopy. Fuel 65, 541-546.

Ungerer, P., Collell, J., Yiannourakou, M., 2015. Molecular Modeling of the Volumetric and Thermodynamic Properties of Kerogen: Influence of Organic Type and Maturity. Energy & Fuels 29, 91-105.

Väli, E., Valgma, I., Reinsalu, E., 2008. Usage of Estonian oil shale. Oil Shale 25, 101-114.

Vallner, L., Gavrilova, O., Vilu, R., 2015. Environmental risks and problems of the optimal management of an oil shale semi-coke and ash landfill in Kohtla-Järve, Estonia. Science of the Total Environment 524, 400-415.

van de Meent, D., Brown, S.C., Philp, R.P., Simoneit, B.R.T., 1980. Pyrolysis-high resolution gas chromatography and pyrolysis gas chromatography-mass spectrometry of kerogens and kerogen precursors. Geochimica et Cosmochimica Acta 44, 999-1013.

van Dongen, B.E., Schouten, S., Sinninghe Damsté, J.S., 2006. Preservation of carbohydrates through sulfurization in a Jurassic euxinic shelf sea: Examination of the Blackstone Band TOC cycle in the Kimmeridge Clay Formation, UK. Organic Geochemistry 37, 1052-1073.

Van Kaam-Peters, H.M.E., Köster, J., De Leeuw, J.W., Damsté, J.S.S., 1995. Occurrence of two novel benzothiophene hopanoid families in sediments. Organic Geochemistry 23, 607-616.

van Kaam-Peters, H.M.E., Schouten, S., de Leeuw, J.W., Sinninghe Damsté, J.S., 1997. A molecular and carbon isotope biogeochemical study of biomarkers and kerogen pyrolysates of the Kimmeridge Clay Facies: palaeoenvironmental implications. Organic Geochemistry 27, 399-422.

Vandenbroucke, M., 2003. Kerogen: from types to models of chemical structure. Oil & gas science and technology 58, 243-269.

Vandenbroucke, M., Largeau, C., 2007. Kerogen origin, evolution and structure. Organic Geochemistry 38, 719-833.

Walters, C., 2007. The Origin of Petroleum, pp. 79-101.

Wan Hasiah, A., 1999. Oil-generating potential of Tertiary coals and other organic-rich sediments of the Nyalau Formation, onshore Sarawak. Journal of Asian Earth Sciences 17, 255-267.

Wan, J., 2009. Environmental impacts of oil shale and pollution control technologies. Coal, Oil Shale, Natural Bitumin, Heavy Oil and Peat, 129-140.

Wang, D.M., Xu, Y.M., He, D.M., Guan, J., Zhang, O.M., 2009. Investigation of mineral composition of oil shale. Asia‐Pacific Journal of Chemical Engineering 4, 691-697.

Wang, Q., Liu, Q., Wang, Z.-C., Liu, H.-P., Bai, J.-R., Ye, J.-B., 2017. Characterization of organic nitrogen and sulfur in the oil shale kerogens. Fuel Processing Technology 160, 170-177.

Wang, Q., Pan, S., Bai, J., Chi, M., Cui, D., Wang, Z., Liu, Q., Xu, F., 2018. Experimental and dynamics simulation studies of the molecular modeling and reactivity of the Yaojie oil shale kerogen. Fuel 230, 319-330.

Wei, Z., Gao, X., Zhang, D., Da, J., 2005. Assessment of Thermal Evolution of Kerogen Geopolymers with Their Structural Parameters Measured by Solid-State ^{13}C NMR Spectroscopy. Energy & Fuels 19, 240-250.

Werner-Zwanziger, U., Lis, G., Mastalerz, M., Schimmelmann, A., 2005. Thermal maturity of type II kerogen from the New Albany Shale assessed by ^{13}C CP/MAS NMR. Solid State Nuclear Magnetic Resonance 27, 140-148.

Whelan, J.K., Thompson-Rizer, C.L., 1993. Chemical methods for assessing kerogen and protokerogen types and maturity, Organic Geochemistry. Springer, pp. 289-353.

Williams, P.F.V., 1987. Organic geochemistry of the British Kimmeridge Clay: 3. The occurrence and distribution of acyclic isoprenoid C19 alkenes in Kimmeridge Clay shale oils. Fuel 66, 86-91.

Williams, P.F.V., Douglas, A.G., 1985. Organic geochemistry of the British Kimmeridge Clay: 1. Composition of shale oils produced from Kimmeridge sediments. Fuel 64, 1062-1069.

Williams, P.F.V., Douglas, A.G., 1986. Organic geochemistry of the British Kimmeridge clay: 2. Acyclic isoprenoid alkanes in Kimmeridge shale oils. Fuel 65, 1728-1734.

Williams, P.T., Ahmad, N., 1999. Influence of process conditions on the pyrolysis of Pakistani oil shales. Fuel 78, 653-662.

Wilson, M.A., Vassallo, A.M., Russell, N.J., 1983. Exploitation of relaxation in cross-polarization nuclear magnetic resonance spectroscopy of fossil fuels. Organic Geochemistry 5, 35-42.

Witte, E.G., Schenk, H.J., Müller, P.J., Schwochau, K., 1988. Structural modifications of kerogen during natural evolution as derived from ^{13}C CP/MAS NMR, IR spectroscopy and Rock-Eval pyrolysis of Toarcian shales. Organic Geochemistry 13, 1039-1044.

Wu, X.L., Burns, S.T., Zilm, K.W., 1994. Spectral Editing in CPMAS NMR. Generating Subspectra Based on Proton Multiplicities. Journal of Magnetic Resonance, Series A 111, 29-36.

Xiu, Z., Nie, W., Yan, J., Chen, D., Cai, P., Liu, Q., Du, T., Yang, B., 2020. Numerical simulation study on dust pollution characteristics and optimal dust control air flow rates during coal mine production. Journal of Cleaner Production 248, 119197.

Yang, S., Horsfield, B., 2020. Critical review of the uncertainty of Tmax in revealing the thermal maturity of organic matter in sedimentary rocks. International Journal of Coal Geology 225, 103500.

Yen, T.F., Chilingarian, G.V., 1976. Oil shale. Elsevier.

Zhan, Q., Zenobi, R., Buseck, P.R., Teerman, S., 1997. Analysis of Polycyclic Aromatic Hydrocarbons in Kerogens Using Two-Step Laser Mass Spectrometry. Energy & Fuels 11, 144-149.

Zhang, Z., Du, X., Carlson, K.H., Robbins, C.A., Tong, T., 2019. Effective treatment of shale oil and gas produced water by membrane distillation coupled with precipitative softening and walnut shell filtration. Desalination 454, 82-90.

Zhao, X., Liu, Z., Liu, Q., 2017. The bond cleavage and radical coupling during pyrolysis of Huadian oil shale. Fuel 199, 169-175.

Zoback, M., Kitasei, S., Copithorne, B., 2010. Addressing the environmental risks from shale gas development. Worldwatch Institute Washington, DC.

Žujović, Z., Srejić, R., Vučelić, D., Vitorović, D., Jovančićević, B., 1995. Structural analysis of Aleksinac oil shale kerogen by high-resolution solid-state ^{13}C n.m.r. spectroscopy. Fuel 74, 1903-1909.

VITA

Wenying Chu
Department of Chemistry and Biochemistry
Old Dominion University
Norfolk, VA 23529

Education

Ph.D. in Chemistry, Old Dominion University, Norfolk, VA, USA
BS in Agricultural Resources and Environment, Huazhong Agricultural University, Wuhan, Hubei, China

Publications

Chu, W., X. Cao, K. Schmidt-Rohr, J. E. Birdwell and J. Mao (2019). "Investigation into the Effect of Heteroatom Content on Kerogen Structure Using Advanced ^{13}C Solid-State Nuclear Magnetic Resonance Spectroscopy." Energy & Fuels **33**(2): 645-653.

Duarte, R. M. B. O., P. Duan, J. Mao, W. Chu, A. C. Duarte and K. Schmidt-Rohr (2020). "Exploring water-soluble organic aerosols structures in urban atmosphere using advanced solid-state 13C NMR spectroscopy." Atmospheric Environment **230**: 117503.

Liu, C.-H., W. Chu, H. Li, S. A. Boyd, B. J. Teppen, J. Mao, J. Lehmann and W. Zhang (2019). "Quantification and characterization of dissolved organic carbon from biochars." Geoderma **335**: 161-169.

Xu, J., B. Zhao, W. Chu, J. Mao and J. Zhang (2017). "Chemical nature of humic substances in two typical Chinese soils (upland vs paddy soil): A comparative advanced solid state NMR study." Science of The Total Environment **576**: 444-452.

Xu, J., B. Zhao, W. Chu, J. Mao, D. Olk, J. Zhang and W. Wei (2017). "Evidence from nuclear magnetic resonance spectroscopy of the processes of soil organic carbon accumulation under long-term fertilizer management." European Journal of Soil Science **68**(5): 703-715.

Mao, J., X. Cao, D. C. Olk, W. Chu and K. Schmidt-Rohr (2017). "Advanced solid-state NMR spectroscopy of natural organic matter." Progress in nuclear magnetic resonance spectroscopy **100**: 17-51.

Fu, H., H. Liu, J. Mao, W. Chu, Q. Li, P. J. J. Alvarez, X. Qu and D. Zhu (2016). "Photochemistry of Dissolved Black Carbon Released from Biochar: Reactive Oxygen Species Generation and Phototransformation." Environmental Science & Technology **50**(3): 1218-1226.

Li, X., J. Dong, W. Chu and Z. Duan (2015). "Adsorption efficiency of a continuous trapping system and its use for the collection of root exudates from cucumber." Journal of Plant Nutrition and Soil Science **178**(6): 963-975.

Li, X., W. Chu, J. Dong and Z. Duan (2014). "An Improved High-performance Liquid Chromatographic Method for the Determination of Soluble Sugars in Root Exudates of Greenhouse Cucumber Grown under CO2 Enrichment." Journal of the American Society for Horticultural Science **139**(4): 356-363.